Research Report

SC-RR-72 0547

PRESSURES IN WATER ON AND NEAR AMCHITKA ISLAND, MILROW AND CANNIKIN

M. L. Merritt
Test Effects Department

Printed February 1973

SANDIA LABORATORIES

OPERATED FOR THE UNITED STATES ATOMIC ENERGY COMMISSION BY SANDIA CORPORATION | ALBUQUERQUE, NEW MEXICO, LIVERMORE, CALIFORNIA

Issued by Sandia Laboratories, a prime contractor to the United States Atomic Energy Commission

---

Printed in the United States of America
Available from
National Technical Information Service
U.S. Department of Commerce
5285 Port Royal Road
Springfield, Virginia 22151
Price: Printed Copy $3.00; Microfiche $0.95

SC-RR-72 0547

PRESSURES IN WATER ON AND NEAR AMCHITKA ISLAND, MILROW AND CANNIKIN

M. L. Merritt
Test Effects Department
Sandia Laboratories, Albuquerque, New Mexico
87115

February 1973

ABSTRACT

Measurements of sea floor ground motion and water pressures resulting from explosions in the underlying rock have been taken: in the Milrow nuclear shot, in the moderately deep water of the surrounding sea; in the Cannikin nuclear shot, in on-shore ponds and streams. Repeated reflections from the water surface and the sea floor were found to modify the pressure wave shapes from those encountered in rock. In Milrow's deep water measurements, this principally resulted in reduced peak pressures; in Cannikin's shallow water measurements, pressure waveforms closely resembled acceleration waveforms. A simple but adequate theory describing these phenomena has been developed. Spall and/or cavitation in water generally results in spray and geysering in on-shore ponds and streams, and white water and spouts off-shore. Bulk or distributed cavitation was apparently present on Cannikin to a much greater extent than on Milrow.

Key words: Underwater, ground motion, spall, cavitation

ACKNOWLEDGMENTS

The Milrow underwater measurement program was a joint effort with the General Motors A. C. Electronics Defense Research Laboratory, now the Delco Electronics Laboratory. Both the Milrow and the Cannikin programs were conducted under the sponsorship and financial support of the AEC's Nevada Operations Office. I wish to thank the various Delco and Sandia people who carried out these programs in the field, especially Jim McNeil and Louis Toth of Delco, and John Dickinson, Ken Kimball, Jim Johnson, and Harry Holmes of Sandia.

TABLE OF CONTENTS

LIST OF TABLES

LIST OF ILLUSTRATIONS

LIST OF ILLUSTRATIONS (Cont)

LIST OF ILLUSTRATIONS (Cont)

PRESSURES IN WATER ON AND NEAR AMCHITKA ISLAND, MILROW AND CANNIKIN

Chapter 1

INTRODUCTION

Milrow and Cannikin were the second and third nuclear shots fired underground at Amchitka Island, Alaska. An earlier underground explosion, Long Shot, was detonated on October 29, 1965, by the Department of Defense as part of the Vela Uniform program of seismic studies. Later, the Atomic Energy Commission needed a site suitable for detonations with yields considerably greater than a megaton of TNT. The Pahute Mesa area of the Nevada Test Site appeared unsuitable for detonations over about a megaton in yield because of possible damage to nearby population centers. Long Shot, with a yield of about 80 kilotons, established suitability of Amchitka for detonations of the order of 100 kilotons. Milrow, with a yield of about 1 megaton buried at a depth of 4000 feet, was fired on October 2, 1969, as a calibration shot for the effects to be expected from a larger shot. Finally, Cannikin, the proof test of the Spartan warhead intended for the Safeguard AIBM system, was fired on November 6, 1971, with a yield somewhat less than 5 megatons and buried at a depth of 5875 feet.

Areas of primary concern associated with the use of Amchitka as a test site were effects on wildlife and seismic response of an area with high natural seismicity. As part of this program observations of ground motion were made on Amchitka and adjacent islands as well as of the resultant pressures in the sea surrounding Amchitka and in some of the many ponds and streams on that island.

Experience on ground-shock-induced water pressures is scarce. The problem is intrinsically different from that posed by shocks generated by explosions in water, as described by Cole (1948) and many investigators since, in that shocks generated by explosions in rock are of longer duration and slower rise times than those in water. Another difference is that underwater pressures resulting from surface and air bursts are mediated by the resulting airblast. Pertinent experience thus consisted only of measurements made in the Long Shot explosion in 1965. On Long Shot, Day and Murrell (1967) of the Waterways Experiment Station installed pressure gages and vertically oriented velocity gages in 60-foot-deep salt water at three positions off shore and in one freshwater pond on Amchitka. Data were reported from only two of the

deep-water gages; the recorded signal from the other gages indicated equipment malfunctions. The available deep-water results were, however, valuable in designing an experiment for Milrow which in turn served as additional guidance in preparing for Cannikin.

Chapter 2

THE EXPERIMENTS

2.1 The Milrow Experiment Plan

The underwater program on Milrow documented the motion of the sea floor and the resultant overpressure in the water above from the nearest point deep enough to be unaffected by surf action. The program was designed to correlate with biological experiments and to gain more comprehensive understanding of the ground-water interaction phenomena. No effort was made to measure pressure in the shallow water of on-shore ponds and streams.

Simultaneously with this project, underground and surface measurements of ground motion were made on Amchitka by Sandia and by the U. S. Coast and Geodetic Survey (now NOAA's Earth Sciences Laboratory (NOAA/ESL)), and surface phenomena were photographed from two nearby aircraft by EG&G, Inc.

The experiment layout consisted of five underwater canisters each with three gages for measuring acceleration and velocity on the sea floor, two gages (duplicates for backup purposes) for measuring water pressure at sea floor level, and two or more gages for measuring pressure at intermediate depths.

The closest canister was in the Pacific Ocean, and the more distant arrays were across the island in the Bering Sea. These locations were to extend the land surface motion measurements being made by Sandia while still remaining in the same geologic block. This layout is listed in Table 2.1 and is given in map form in Figure 2.1.

Each canister weighed about 2 tons and displaced 13 cubic feet and thus had a specific gravity of about 5. They were held to the bottom only by their own weight.

The canisters contained initial signal conditioning equipment, orientation and leveling equipment, and power and temperature monitors (ACDRL, 1969). The sea floor gages were supported by the canisters, and the intermediate gages were suspended by cable between a slightly submerged buoy and the canister.

Marine cables, armored against wave and surf action, connected the canisters to trailer-mounted recording equipment; however, the cable with the longest span required an intermediate radio telemetry link over land.

Locations of the canisters were determined by survey triangulation of the chartered cable-laying ship at time of installation and, hence, are not presumed to be more accurate than ±50 feet. Water depths were measured at the same time and, since tidal fluctuations at Amchitka are small (<5 ft), no further corrections were made.

Accelerometers used were Kistler Model 303's mounted in triaxial mount within the canister. The active elements of these gages are mass-spring systems slightly more than critically damped at the expected temperature of 40°F. Velocity gages were provided by Sandia. Horizontally oriented gages were pendulums grossly overdamped, with variable reluctance pickups. In the vertically oriented gages, the pendulums were supported by a spring, forming in essence a damped mass-spring system. Since their calibration depends on damping, the temperature (a factor in damping) was also monitored in the canister. The pressure gages were Pace Model CP51 mounted in the cover of the canister with their diaphragms coupled to sea water through a fluid column and subsidiary diaphragm.

Signal return on the underwater cable was by standard IRIG fm telemetry. This, not gage or recording response, established the effective bandwidth of data as reported in this report. The effective bandwidths for each kind of channel--all canisters being alike in this respect--are given in Table 2.2. Four channels were further filtered for commutation with various monitors of canister operation.

2.2 Intermediary History

The Milrow experiment was very successful in percentage of data returned; however, it soon became evident that insufficient attention had been given to the consequences of reverberation of the pressure wave in the ocean water. The water was not sufficiently deep to prevent surface reflected rarefactions (negative pressure waves) from interfering with the initial peak. As a result, an approximately linear decrease of peak pressure appeared with depth of gage. In addition, gage measurements and photographs taken by EG&G showed that water spall and resulting cavitation* were dominant phenomena. Nevertheless, the preshot theory appeared to

*Cavitation usually means bubble formation when the tensile strength of water is exceeded. In this report the word is used to mean failure of water in tension in the negative phase of a pressure wave. It is thus akin to spall in solids, except that distributed failure, or failure throughout a whole volume rather than at a plane surface, is possible.

account for the observed underwater pressure waveshapes (Merritt, 1969b, 1970, 1971). (See also Section 3.3 below.)

Effects dependent on finite depth of water should be exaggerated in the very shallow water of on-shore ponds and streams. Indeed, the EG&G photography indicated that shallow water as far as several miles from SZ was thrown upwards in sheets of white spray. (This had also been seen in Long Shot, but was not deemed significant!) In contrast to the marine scene where no otter or fish kill was detected, an extensive kill of stickleback in two of the closer ponds on Long Shot (Kirkwood, 1970; Valdez and Helm, 1971) served to indicate that measurements in shallow water would be needed on Cannikin.

2.3 The Cannikin Experiment Plan

In Cannikin the principal consideration in siting the gages was to measure pressures and accelerations at the same places where biological observations were to be made. The locations are listed in Tables 4.1 and 4.2 and given in map form in Figure 2.2. Since places were widely scattered, making active gages impractical, passive gages were relied upon for the bulk of the measurements.*

The active pressure gages were Validyne P-66 units of 50-psi range. The active element in these instruments is a diaphragm with a variable-reluctance pickup. Signals were transmitted by hardwire telemetry to a recording station also used for ground motion measurements by Perret (1972). Heavy weights, mounted on metal stakes driven in the bottom of the three ponds, supported the gages in a side-on position with each axis horizontal and diaphragm vertical to eliminate dynamic pressure effects.

The passive pressure gages were Validyne PR-61 units of various ranges. Their active element is a diaphragm driving a V-shaped stylus that cuts into indium. The width of the resulting indentation is related to the peak pressure incident on the diaphragm.

Passive accelerometers were of two types. The Teledyne-Geotech PRS-100 gage is a three-axis accelerometer. In it a small permanent magnet attached to a damped spring-mass system wipes a prerecorded signal from a small piece of magnetic tape.

---

*Active gages are gages and recording systems that yield the whole time history of the phenomenon being measured. These call for hardwire or radio telemetry of signals to a central recording station. Passive gages are self-recording instruments that indicate only the peak value of the phenomenon being measured.

After use, the tape is dipped into a suspension of iron powder, dried and fixed by a light spray of lacquer, and then the length of area free of iron deposit is measured with a micrometer. The Dynasciences Model A-12 is a single-axis gage and is bidirectional. Upon acceleration a mass, restrained by a leaf spring, crushes a soft pellet, the resultant width of which is related to the driving acceleration. Their behavior during calibration led us to install more than one wherever they were used.

The Teledyne passive accelerometers were generally mounted on top of a 2-inch pipe driven into the ground (Figure 2.3); in retrospect we realize that this may render questionable the measurement of the two horizontal components of acceleration, although the vertical component presumably remains valid. At three positions the Teledyne gages were bolted onto existing concrete pads (Figure 2.4). The Dynasciences passive accelerometers were mounted at ground level inside pipes driven into the ground.

An additional type of passive pressure gage had been procured to record higher pressure ranges at the marine fish-holding pens, but heavy seas on the day before Cannikin prevented such pens from being installed, and these gages were not used. It had been decided a year earlier not to use Milrow-type canisters on Cannikin because of the very large expense involved and because the Milrow results were well explained. Thus no deep-water measurements at all were made on Cannikin.

As on Milrow, underground and surface measurements of ground motion were made on the island by Sandia and by NOAA/ESL, and surface phenomena were photographed from a nearby aircraft by EG&G and from stations on the ground by Pan American World Airways.

Chapter 3

RESULTS - MILROW

3.1 The Milrow Data

Milrow was detonated at 1206 BDT (2206 GMT) October 2, 1969, in a hole 4000 feet deep on Amchitka. Its yield was about 1 mt. Surface zero (SZ) was at an elevation of 129 feet.

All except three of the 53 underwater channels gave apparently valid data; pertinent data from these records are compiled in Table 3.1, and the waveforms themselves are plotted in Figures 3.1 through 3.13. As to the three failures, W16 UT and W23 PB1,* were known to be faulty before the shot; the third gage, W20 PH2, failed to operate properly.

Very noticeable on the acceleration records of Figures 3.1 through 3.3 is a violently oscillating signal that starts in or after the negative phase. Its frequency is about 250 Hz, well within the bandpass of the three acceleration channels (see Table 2.2). The PH2 channels, with a bandwidth of 330 Hz, have a smaller noise pattern like that of the acceleration channels; and the PB2 channels, with a bandwidth of 220 Hz, have just a hint of such noise. Channels such as W8 AR, and especially W13 AR, show a trace of such a signal before shock arrival. On the W16 channels this noise shows several false starts before a slow buildup. Such a noise signal may have been present on other channels, but if so it was filtered out. This oscillating signal is present before shock arrival at a lower level, appears on PH2 which was not on the canister and on PB2 which was at a different place on the canister than the acceleration gages, all of which suggests that this signal is not a direct effect of the shock on the gages, but an unknown effect of shock on the electronics in the canister.

The next to the last column in Table 3.1 lists the preshock-arrival ambient pressure at the pressure gages as determined from the gage depth of the fourth column by the formula $P_o(\text{psi}) = 14.7 + 0.445d(\text{ft})$ (or $P_o(\text{atm}) = 1 + 0.1d(\text{m})$). The measured pressures are overpressures and underpressures, measured relative to this ambient pressure. In principle, no underpressure should be large enough to reduce the total

*This notation is explained in the footnote to Table 2.1.

absolute pressure to below zero. With one exception this is true. The exception is the record from gage W8 PB1. Its peak underpressure is -83 psi vis-a-vis a preshock ambient of about 50 psi. Looking at its waveshape in Figure 3.7 and comparing it with record W8 PB2, this appears to be a temporary overshoot that immediately relaxes to the expected -50 psi.

Another apparent discrepancy between records W8 PB1 and W8 PB2, and indeed between every PB and PH pair, is that the PB1 (and PH1) signal is later in arrival, time of peak, and all other respects than the PB2 (and PH2) record measured at almost the same place in the water. This delay is an artifact caused by the 35 Hz (and 14 Hz) filter which the PB1 (and PH1) signal went through before being commutated, as mentioned in Section 2.1. UV records also experienced such a filter delay.

Amplitude discrepancies in various PH and PB pairs suggest signal to gage range problems; however, the signal to gage range ratio of the pair with the greatest discrepancy, W23 PH, is no worse than that of a number of other pairs with much smaller discrepancies, so this cannot be a complete explanation.

A final observation on the data is that the closest three stations (W8, W13, and W16) have AV and UV waveshapes superficially symptomatic of spall. In detail, the W8 UV record does show a prolonged period of -1 g acceleration, but the W13 AV and UV records show only -0.8 g, and the W16 AV and UV records show an initial -1 g that gives way to -0.8 g. The value -0.8 g suggests a canister thrown free from the bottom rather than spall in the underlying rock. Each canister had a net density of five times that of water; its buoyancy was thus 1/5 its weight; and its free fall in water, excluding drag effects, would be at -0.8 g.

3.2 Theory of Reverberations

The analysis of underwater pressures generated by motion of the ocean floor necessarily starts with the theory of that interaction. This theory was developed by Merritt (1969a), and arrived at independently by Koh and Rosenkranz (1970); but since those reports were of limited circulation, the theory is repeated here.

Consider a wave coming straight up out of the ground into a layer of water. Its pressure and particle velocity will be related as

$$P_R = \rho_R c_R U_R = Z_R U_R \ , \qquad (3.1)$$

where P_R is overpressure, ρ_R is rock density, c_R is longitudinal sound velocity, U_R is particle velocity, and Z_R is so-called seismic impedance. At interaction with water of impedance Z_W, transmission and reflection factors are:

$$T_p = \frac{P_W}{P_R} = \frac{2Z_W}{Z_R + Z_W}$$

$$T_u = \frac{U_W}{U_R} = \frac{2Z_R}{Z_R + Z_W}$$

$$R_p = \frac{Z_W - Z_R}{Z_W + Z_R}$$

$$R_u = \frac{Z_R - Z_W}{Z_R + Z_W} .$$

Assuming c_R = 3.33 m/msec, c_W = 1.4 m/msec, ρ_R = 2.38 gm/cm^3, and ρ_W = 1 gm/cm^3, then Z_R/Z_W = 17/3, and

$$T_p = 0.3 \qquad T_u = 1.7$$

$$R_p = -0.7 \qquad R_u = 0.7 \tag{3.2}$$

At other angles these factors change, with small additional perturbations caused by the generation of shear reflections. However, in all cases, the wave in water is refracted towards the vertical, and can never be more than 25 degrees from it. It will be convenient hereafter to let R = 0.7 and take care of signs by physical reasoning.

Let the input wave in rock have the form

$$\frac{P_R}{P_m} = g\left(t + \frac{y}{c_R}\right), \tag{3.3}$$

where P_m is the peak pressure, and distance, y, is measured down from the rock-water interface. The pressure transmitted into the water then is

$$\frac{P_W}{P_m} = (1 - R)\, g\left(t + \frac{y}{c_W}\right) = f\left(t + \frac{y}{c_W}\right) \tag{3.4}$$

and the signal reflected back into the rock is

$$Rg\left(t - \frac{y}{c_R}\right).$$

The transmitted wave is reflected from the water surface, adding a pressure in the water

$$-f\left(t - \frac{y}{c_W} - \frac{2d}{c_W}\right)$$

where d is the depth of the water. After interaction with the rock-water interface, a wave is transmitted down into the rock

$$-(1 + R)\, f\left(t - \frac{y}{c_R} - \frac{2d}{c_W}\right) = -\left(1 - R^2\right) g\left(t - \frac{y}{c_R} - \frac{2d}{c_W}\right)$$

and one is reflected back up in the water

$$-Rf\left(t + \frac{y}{c_W} - \frac{2d}{c_W}\right).$$

Carrying this induction forward, we conclude that

$$\frac{P_R(t)}{P_m} = g\left(t + \frac{y}{c_R}\right) - Rg\left(t - \frac{y}{c_R}\right) - \left(1 - R^2\right)\sum_{o}^{\infty}\left(-R\right)^n g\left(t - \frac{y}{c_R} - \frac{(2n + 1)d}{c_W}\right) \tag{3.5}$$

and

$$\frac{P_W(t)}{P_m} = \sum_{o}^{\infty}\left(-R\right)^n\left[f\left(t + \frac{y}{c_W} - \frac{2nd}{c_W}\right) - f\left(t - \frac{y}{c_W} - \frac{(2n + 2)d}{c_W}\right)\right]. \tag{3.6}$$

Equations for velocity are similar differing only in the sign of some terms.

The assumptions that have been made are (1) linearity, especially no attenuation, (2) plane waves normally incident, (3) perfect interfaces, (4) no further structure or gradient of properties in the rock, (5) shear-free media (only important for nonnormal incidence), and, most important of all, (6) continuity, which is to say no spall in the rock, no separation between rock and water, and no cavitation in the water. The last assumption is further discussed in Section 3.4.

3.3 Application of the Reverberation Theory

In practice velocity and pressure at the sea floor are measured, and f(t) must be inferred from these. A little manipulation of the appropriate series shows that, at y = 0,

$$f(t) = \left(\frac{1 + R}{2}\right) Z_W U_W(t) + \left(\frac{1 - R}{2}\right) P_W(t) \quad . \tag{3.7}$$

For shear-bearing rock, the reflection factor of signals passing from water into rock is nearly independent of angle out to a refracted angle of 70 degrees in rock (Merritt, 1969, p 41). Thus in this application, assumptions two and five in Eq. (3.7) are not significant.

The operations implied have been carried out for all five Milrow stations. The velocity needed is the vertical component UV; it is multiplied by the impedance Z = 62.8 psi/fps (14 atm/mps) to produce a velocity in units of psi. (The Z will be dropped henceforth.) As stated in Section 2.1, UV and PB1 were delayed in their filters. The amount of this delay was evaluated graphically, at 20 and 40 msec, respectively, and this adjustment was made. At all stations except W23 there were two successful measurements of PB, and so in practice f(t) was determined by

$$f(t) = 0.85\ UV(t - 20) + 0.075\ PB1\ (t - 40) + 0.075\ PB2\ (t). \tag{3.8}$$

Figure 3.14 shows W8 PB1, W8 PB2, W8 UV plotted together and the resultant f(t). Figure 3.15 shows W8 PB1 and W8 PB2 compared with a PB back calculated from the f(t). Figure 3.16 shows W8 PH1 and W8 PH2 compared with a calculated PH. The other four stations are reported similarly in Figures 3.17 through 3.30.

The reconstructed input signals f(t) are given in Figures 3.14, 3.17, 3.20, 3.23, and 3.27. The slow rises of about 80 msec are real, since they are well within the response capability of all instruments and recording channels. (Explosions in

air and water, as is well known, yield shock waves with almost instantaneous rises (Glasstone, 1962; Cole, 1948); but explosions in rocks or soils generate shock waves whose fronts quickly deteriorate into slow rise times such as these.) Generally the function f(t) has a waveshape much like UV, as might be expected from Eq. (3.8).

To compare with measurements on land let us estimate what the interface velocity UV would have been without the overlying water. For nonnormal incidence, assuming no shear waves reflected back into the rock, the transmission factors corresponding to Eq. (3.1) are

$$T_u = \frac{2Z_R \cos \theta_R}{Z_W \cos \theta_R + Z_R \cos \theta_W}$$

$$T_p = \frac{2Z_W \cos \theta_R}{Z_W \cos \theta_R + Z_R \cos \theta_W} = \frac{f}{g} \quad . \tag{3.9}$$

Without overlying water, the surface velocity would be

$$U(\text{no water}) = \frac{2g \cos \theta_R}{Z_R} \quad . \tag{3.10}$$

Remembering that

$$\frac{Z_R}{Z_W} = \frac{1 + R}{1 - R}$$

we get

$$U(\text{no water}) = \frac{2f \cos \theta}{Z_R} \left[\frac{(1 - R) \cos \theta_R + (1 + R) \cos \theta_W}{2(1 - R) \cos \theta_R} \right] \tag{3.11}$$

whence

$$\frac{Z_W U(\text{no water})}{f} = \left(\frac{1 - R}{1 + R} \right) \cos \theta_R + \cos \theta_W \tag{3.12}$$

which reduces to $2/(1 + R) = 1.176$ for normal incidence. As Perret and Breding point out (1972, p 44), pressure waves in the real world do not travel in straight lines

because velocities generally increase with depth. The angles of incidence θ_R at the five underwater stations cannot be precisely determined; one can only say that they are less than what straight line ray paths would imply. With the existing geometry, these angles vary from less than 66 degrees at W8 to less than 81 degrees at W23, and in Eq. (3.12), the right side is larger than 0.996 to 0.938 or to the accuracy of the estimate, the right side can be set equal to unity. Therefore,

$$U(\text{no water}) \approx \frac{f}{Z_W} \quad . \tag{3.13}$$

In Figures 3.15, 3.18, 3.21, 3.24, and 3.28, the bottom pressure PB is calculated and compared with the measured pressure. (There is a slight circularity in logic in doing this, since f(t) was determined in small part from PB.) In all cases the first overpressure pulses agree very well. In Figure 3.15 (W8 PB), the negative or underpressure phases differ markedly. At the left margin of the figure, the preshock ambient is indicated. In this instance the calculation broke down after cavitation set in. The overshoot on record W8 PB1 followed the calculation, and the measured pressure does lie in the middle of the calculated oscillation, but this may be sheer coincidence. In Figures 3.18 and 3.24 (W13 PB and W20 PB), calculated and measured PB's agree well through the whole record. In Figure 3.21 (W16 PB), calculated oscillations are more extreme than measured. In Figure 3.28 (W23 PB) amplitude agreement is good, but phase differences accumulate. In all the three more distant stations a slow oscillation sets in during the negative phase whose period is about $4d/c_W$: the double round trip time arises from the fact that reflection at the upper water surface is out of phase (compressions return as rarefactions and vice versa), whereas reflection at the sea floor is in phase.

The remaining figures in this group compare calculated pressures at mid-depth with measured pressures. Again in all instances, the first overpressure pulses agree. Figure 3.16 (W8 PH), like 3.15 (W8 PB), shows an apparent cavitation-limited signal, although there is a discrepancy between the 26 psi of where the underpressure should cut off and the 20 psi of where it does. In Figure 3.22 (W16 PH) the calculated underpressure considerably exceeds the measured underpressure, so that the former (but not the latter) exceeds the ambient pressure limit. In Figures 3.25 and 3.26 (W20 PI and W2 PH) calculated and measured pressures agree well through the whole record. In Figure 3.29 (W23 PI) as in Figure 3.28 (W23 PB), amplitude agreement is good, but phase differences accumulate. In Figure 3.30 the two records are plotted (W23 PH1 and W23 PH2) which were in unsatisfactory agreement as stated in Section 3.1. The calculated curve agrees well with W23 PH1, barring the phase shift common to all W23 stations. I, therefore, conclude that W23 PH2 is the faulty one of the pair.

All in all, the reverberation theory accounts for the measured pressures very well, with one major fault: the theory takes no account of total pressure and breaks down when the total pressure goes to zero, that is, when the underpressure achieves the magnitude of the preshock ambient pressure. In any given instance, the calculation is valid until that happens, but thereafter must be discarded.

3.4 Spall and Cavitation

Since spall and cavitation appear to be important modifiers of ground motion and resulting water pressures, some further attention is due them. In its usual use, spall refers to an internal failure of a solid in tension due to reflection of a compression wave along a free surface. In most detonations where there is no surface water, spall is evident at SZ and out to a horizontal distance equal to several burst depths--in Milrow out to at least 17,000 feet from SZ (Perret and Breding, 1972). Typical AV and UV waveshapes in the spall region are shown in Figure 3.31 (Cannikin records SF5S-AV and UV). After shock arrival there is an extended period of free fall, followed by an abrupt arrest as the spalled material hits bottom. The acceleration waveform is two shock pulses separated by a -1 g plateau, with the second or slapdown pulse often larger and rising more quickly than the first. In velocity, an N-shaped wave results. With multiple spalls there may be several slapdown pulses. When there is surface water the phenomenon is usually more complicated: the reflected signal is weaker so that one might expect a less extensive spall in the rock, but the water may fly upwards, either as a single mass or breaking up in the process.

To see what may happen, let us examine a specific, perhaps oversimplified situation in detail, following the various phenomena as they happen in the space time diagram of Figure 3.32. Assume that an incident wave I comes straight upwards, with a triangular waveshape:

$$\begin{aligned} P_R = P_m g(t) &= P_m\left(1 - t/t_o\right) \qquad 0 < t < t_o \\ &= 0 \qquad\qquad\qquad\quad \text{all other } t \ . \end{aligned} \tag{3.14}$$

Let t_o = 300 msec and P_m = 150 atmospheres. Assume 25 m of water over the rock, and properties of water and rock as before. If all surfaces stay together, pressures in water and in rock would be given by Eqs. (3.5) and (3.6); however, they do not. A transmitted shock T of magnitude (1 - R) P_m = 45 atm continues into the water, reaching the surface at 17.86 msec, and is then reflected in tension, line RT in

Figure 3.32. Setting z = y + 25 = depth below the water surface, the time on line RT is $t = (z + d)/c_W$ and the pressure on it is:

$$P_W = (1 - R)P_m\left[g\left(\frac{2z}{c_W}\right) - g(1)\right] = -(1 - R)P_m \frac{2z}{c_W t_o} \quad . \tag{3.15}$$

The criterion for spall in the water is

$$|P_W| = 1 + 0.1d \tag{3.16}$$

so that spall failure occurs at depth

$$z_S = \frac{1}{\left[\frac{2(1 - R)P_m}{c_W t_o} - 0.1\right]} \quad . \tag{3.17}$$

For the conditions stated, this evaluates to a depth of 8.75 m, point S in Figure 3.32. Without going through the details, it can be shown that for this linear waveform the water above this depth has a uniform velocity upwards of:

$$Z_W U_W = 2(1 - R)P_m\left(1 - \frac{z_S}{c_W t_o}\right) \tag{3.18}$$

or a velocity of 6.3 m/sec. For other waveforms this uniformity is of course only approximate.

Water below this depth, region 4 in Figure 3.32, is all in continuous spall, because as each new part of the upgoing wave reaches the current top of the water, it finds there a free surface without even an overlying atmospheric pressure, and this new surface flies upward. Water in region 4, therefore, is in a state of nearly zero total pressure (vapor pressure remains), and of velocity:

$$Z_W U_W(z) = 2(1 - R)P_m\left(1 - \frac{2z}{c_W t_o}\right) + 1 + 0.1z \quad , \tag{3.19}$$

the term (1 + 0.1z) coming from relief of the original hydrostatic pressure. Below $z = z_S$, velocity changes continuously, but because velocity decreases with depth, there must be true cavitation or bubble formation in this whole region.

In the rock one must distinguish three regions: 1, 5, and 6 in Figure 3.32. In region 1 there is only the incident wave:

$$P_R = Z_R U_R = P_m g\left(t + \frac{y}{c_R}\right) . \tag{3.20}$$

In region 5, there is in addition a reflection

$$P_R = P_m\left[g\left(t + \frac{y}{c_R}\right) - Rg\left(t - \frac{y}{c_R}\right)\right] . \tag{3.21}$$

In region 6, there is a larger reflection and also a rarefaction from the removal of the weight of water:

$$P_R = P_m\left[g\left(t + \frac{y}{c_R}\right) - g\left(t - \frac{y}{c_R}\right)\right] - (1 + 0.1d) . \tag{3.22}$$

Thus at any depth y, there is a rarefaction jump at line R of magnitude $-RP_m$; and another jump at line TRT of magnitude $-(1 - R)P_m - (1 + 0.1d)$.

As to spall in rock, there is clearly a reduced potential for it on line R, for there the requirement is

$$\left|P_R\right| = P_m\left[\frac{2y}{c_R t_o} - (1 - R)\right] = 1 + 0.1d + 0.238y + T$$

where T is the effective tensile strength of the rock. Thus spall depth on line R is

$$y_S = \frac{1 + 0.1d + T + (1 - R)P_m}{\left(2P_m/c_R t_o\right) - 0.238} . \tag{3.23}$$

If there had been no water (d = 0, R = 1), the spall depth would be 16(1 + T) meters. With water one gets 780 + 16T meters, so deep that the implicit assumption of plane wave input must break down. Effectively there is no spall on the line R if water is present.

On the line TRT, the requirement for spall is

$$\left|P_R\right| = \frac{2yP_m}{c_R t_o} + (1 + 0.1d) = 1 + 0.1d + 0.238y + T$$

yielding a spall depth

$$y_S = \frac{T}{\left(2P_m/c_R t_o\right) - 0.238} \quad . \tag{3.24}$$

This final expression is remarkably like that applying when there is no water, having only a T where the latter has (1 + T). In bulk, rock has little or no tensile strength because of natural fractures. Thus we should expect less spall and that spall should occur shallower in rock under water than in rock without water above it.

(The example just carried through was such that the first spall failure in water was less than the water depth ($z_S < d$). When this is not the case, region 4 in Figure 3.32 disappears; but there is still usually a spall at the water-rock interface induced by the large impedance mismatch there, the water separating from the rock and flying upward in free fall. However, this leaves nearly zero total pressure at the interface, so that the conditions in region 6 are as they have been described, and Eq. (3.24) remains valid.)

These observations agree with the measured sea floor motion discussed at the end of Section 3.1. Only station W8 had a clearly defined period of -1 g acceleration; W13 and W16 showed -0.8 g, the latter with an initial momentary -1 g. W20 and W23 had smaller negative accelerations yet. If there had been spall underneath in the rock, both the rock and the water would be settling back in free fall at -1 g, and the buoyancy of the water would not be effective. Thus the experimental data on Milrow indicated that spall under the sea only surely to the 8400-foot horizontal range, and certainly not as far as 13,000 feet. In contrast, spall on land extended out at least to 17,000 feet (Perret and Breding, 1972).

For practical considerations of underwater spall and cavitation, complications such as oblique incidence and shear waves in the rock must be added. General features can be expected to be the same, however, yielding these predictions for Milrow and Cannikin:

a. Spall in rock under the sea will not extend out to the same horizontal range as on land.

b. The water will fly up, a surface layer tending to stay together, but if the water is deep enough, below the surface layer, there will be massive cavitation.

3.5 Arrival Times

In Figure 3.33 arrival times are compared to those of Perret and Breding (1972) and to the latters' fit to their data. Although the underwater arrival times depart slightly from the overland data, these are all obviously one ensemble of data. Interstation velocities are reasonable, 12 to 15,000 ft/sec.

3.6 Amplitudes of Ground Motion

In Figure 3.34 vertical peaks of acceleration as reported by Perret and Breding (1972) and by ERC (1970) are plotted against slant range. From Perret's data both first and slapdown pulses are plotted. ERC also had two data points at about 10^6 feet, at Adak and Shemya, off the end of the plot. The solid line is the best linear fit through the data:

$$AV = 429(SR)^{-2.0} \tag{3.25}$$

where SR is measured in kilofeet. The underwater accelerations agree, but not excellently.

In Figure 3.35 vertical components of velocity are plotted against slant range from the same source. The line of best fit is

$$UV = 180(SR)^{-1.6} \quad . \tag{3.26}$$

The underwater data plotted are, according to Eq. (3.13), velocities equal to the calculated f(t) divided by the seismic impedance Z_W.

It thus appears that these underwater data are valid ground motion data.

3.7 Peak Overpressures

A major consequence of the reverberation theory and its result, Eq. (3.6), is that for shallow gage depths, the input pressure signal propagating upward past the gage does not have time to reach its peak before a rarefaction reflected from the water surface returns and keeps the measured pressure from rising further. This effect occurs when the gage depth is

$$z < \frac{c_W t_r}{2} \quad , \tag{3.27}$$

regardless of water depth. The effect is very evident in Figures 3.14, 3.17, 3.20, and 3.23, but does not appear in Figure 3.27 because at that station and depth the inequality no longer holds. Since the rise time t_r is about 80 msec, the critical depth is about 180 feet or 30 fathoms.

Wave fronts are approximately linear, so that the net effect on peak pressure is an approximately linear decrease of peak pressure for gage depths less than 180 feet. For gage depths greater than this, the reflected rarefaction arrives after the peak and does not affect it. Then the peak is related to the vertical component of the velocity of the sea floor by the seismic impedance of water, Z_W = 63 psi/fps.

Thus peak positive overpressure is a function both of range from the source and depth of point of interest. Figure 3.36 shows this synthesis. The top line, derived from the measured peak vertical velocities of Figure 3.35 is the peak overpressure that would have been measured at any depth of 180 feet or deeper. The other lines represent overpressures at other depths; the 60-foot line, for example, is a factor of 3 below the top line. The measured peak overpressures are also plotted. In each instance where two gages were at the same location but gave different readings, the readings are combined. The number beside each set of readings indicates the depth at which the readings were taken. Despite differences in detail, as in the individual waveshapes, the agreement is generally good.

Overpressure at the water surface should be zero. To confirm this, sealed empty beer cans served as pressure gages and were tied to floating sea otter pens, one near station W8, and two further away on the Pacific side of Amchitka. The cans did not collapse or buckle inwards which indicated that overpressures were less than 7 to 10 psi, the previously determined threshold required to buckle the cans.

3.8 Pressure Contours

Another means of summarizing the shock pressures in the ocean surrounding Amchitka is to draw on a map contours of peak pressures resulting from Milrow. These contours appear in Figure 3.37. The contours of the peak positive overpressure at the ocean floor follow the rules:

$$PB = 11300(SR)^{-1.6} \qquad d > 180 \text{ ft}$$

$$= 11300(SR)^{-1.6}\left(\frac{d}{180}\right) \qquad d < 180 \text{ ft} \quad . \tag{3.28}$$

Above the ocean floor, pressures were less, and are obtained by substituting z for d in Eq. (3.28).

There appear to have been three areas on the ocean floor where overpressures were greater than 100 psi; one was verified by station W8.

In addition, Figure 3.37 includes contours of a large area on each side of Amchitka, in which underpressures were so large that there was complete relief of pressure at the sea floor causing the water to spall. These areas are more extensive than the overpressure contours.

The four more distant canisters skirted the edge of the water spall contour on the Bering side of Amchitka. This confirms the observation of Section 3.4 that the bottom gages at W13, W16, and W20 recorded, at most, only borderline instances of cavitation, and W23 recorded no cavitation.

These pressure contours are sensitive to the cut off depth of 180 feet. That depth is equivalent to a rise time of 80 msec and was obtained from the velocity waveforms of Figure 3.4 and the equivalent measurements on land (Perret and Breding, 1972, Figures 3.6 et al). Those wave fronts are actually not straight, but S-shaped; the steepest part of the wave front is equivalent to a rise time of about 70 msec, and the whole rise from toe to peak about 100 msec; 80 msec is an in-between figure justified post hoc by Figure 3.36. A larger rise time would decrease the size of the contours in Figure 3.37, and vice versa.

The water spall contour is sensitive to the rate of decrease of pressure behind the pressure peak. For the purpose of drawing Figure 3.37, this portion of the wave-shape was approximated as a straight line that would reach zero in a time twice the rise time, approximately what the f(t)'s of Figures 3.14 et al would suggest. A slower decrease would decrease the size of the cavitation limit contour in Figure 3.37, and vice versa.

3.9 Summary -- Milrow

In summary these observations may be made about the underwater ground motions and pressures measured in this project on Milrow:

a. The ground motion data are consistent with ground motions measured on land reported by Perret and Breding (1972) and ERC (1970).

b. Underwater pressures in these waters of moderate depth show strong effects of reverberation in the water. A principal result is reduced peak pressures compared to those obtained by multiplying the peak vertical velocity of the sea floor by the seismic impedance of the water. Time scales of these peaks are also shortened, and a slow oscillation often appears in the later part of the record.

c. The theory describing this reverberation concludes in Eqs. (3.5) and (3.6). This theory breaks down when the underpressure in the negative phase achieves the magnitude of the preshot ambient pressure, i.e., when spall or cavitation ensures. Thereafter, its results must be discarded.

d. Spall in rock differs as a result of water overlying that rock; it does not extend to the same horizontal range as on land. The water itself tends to fly up and, depending on its depth, there may be a volume of bulk or distributed cavitation above the sea floor.

e. No measurements were made in Milrow in on-shore ponds and streams.

Chapter 4

RESULTS - CANNIKIN

4.1 The Cannikin Data

Cannikin was detonated at 1100 BST (2200 GMT) on November 6, 1971, in a hole 5875 feet deep on Amchitka. Its yield was somewhat less than 5 mt. Surface zero was at an elevation of 208 feet. The five active pressure gages gave apparently valid data until 1.8 seconds, when the generator power failed and both Perret (1972) and I lost all further information. (A momentary interruption of power just before final failure produced a spurious signal at 1.68 seconds on all records.) All passive gages were recovered in the first few days following the detonation, except for one acceleration gage that was lost under cliff falls and one pressure gage that could not be found in a drained lake.

The pressure waveshapes differ in several particulars from those measured on Milrow: (1) the amplitudes are smaller, which was expected from the much shallower water; (2) early parts of the records resemble acceleration waveforms with an initial pulse, a long plateau, and then a second pulse(s) quite unlike slapdown pulses.

4.2 Shallow Water Theory

Section 3.2 described the pressure in a layer of water over rock as a series of reverberations; Section 3.3 showed that this theory accounts well for measured pressures in moderately deep water. For shallow water, a much simpler theory may suffice. If one assumes the water is so shallow that it moves en masse, then by elementary physics the overpressure at the bottom of that water should be related to its acceleration as

$$P = \rho d a \tag{4.1}$$

where ρ is the density of water, d is water depth, and a acceleration. In the notation of the previous chapter this form becomes:

$$P = \frac{Zda}{c} = \frac{d}{c}\frac{d}{dt}(UZ) = \frac{d}{c} P_m f'(t) \tag{4.2}$$

which is closely related to Eq. (3.5).

In Figure 4.6 three examples are given which compare what Eqs. (3.5) and (4.2) would predict for the same circumstances. In each example, the input waveshape f(t) is given at the left, and the computed results are given to the right; the results by the more exact Eq. (3.5) are solid lines, and by the approximation Eq. (4.2) are dashed lines. In these examples, $\tau = 2d/c = 10$ msec, equivalent to water 7 meters deep. Two examples are given with sharp wave fronts and one with a slowly changing wave front. These examples indicate that for sharp wave fronts (acceleration rise time less than reverberation time in water), the real pressure given by Eq. (3.5) overshoots and oscillates about the pressure given by Eq. (4.2); whereas for slowly rising waves, the two yield about the same results.

The overshoots shown in Figure 4.6 are about a factor of 2 larger, very similar to the overshoot of underdamped mass-spring systems or electrical circuits. In steady-state or slowly changing response, (Figure 4.6c or the latter part of Figure 4.6a), however, the Eq. (3.5) pressure ends up slightly higher than the Eq. (4.2) approximation. Although not generally true, in those two instances it can be shown that the error is approximately a factor of $2/(1 + R) = 1.176$.

The waveshapes in Figures 4.1 through 4.5 are in qualitative agreement with these principles. The first pulse corresponds to a slowly varying acceleration pulse; the second to a sharp slapdown pulse.

(Discussed and rejected elsewhere (Merritt, 1972) is another possible explanation of the second pulses: that the water movement exposed the gages to the dynamic effects of muck and other bottom materials. The basic reasons to support the present theory are: simplicity of explanation, cause for fish kill, and agreement with accelerations.)

The second pulses are shown in expanded time scale in Figures 4.7 through 4.10. The second signal in lake BP (Figure 4.7) is a single narrow spike. (The signal immediately after the spike at 1.68 seconds is the spurious signal referred to above and seen on all records.) Second signals in records DK-2, DP-1, and DP-2 (Figures 4.8 through 4.10) are strongly oscillatory with periods of 4 to 6 msec. The second signal at DK-1 came too late to be seen before power failure. The single spike of Figure 4.7 does not fit the pattern suggested by the calculations behind Figure 4.6. One can only guess that since this lake had a hard and well-defined bottom (as opposed to soft, mucky bottoms), in this case the water did indeed leave the gage cleanly behind, surrounded only by air. The second pulses of Figures 4.8 and 4.9 do fit the overshoot pattern, and for that reason the factor of 2 is used henceforth as an adjustment

factor in inferring accelerations. (The flat top on the first positive excursion of Figure 4.8 is a slightly clipped signal.) The more complicated second pulse of Figure 4.10 (DP-2) suggests multiple slapdown signals. DP-1, 60 meters to the north of DP-2 in the same lake, shows a single pulse; but Perret's nearest gages (S6, 280 meters closer to SZ than DP-2, and SF5N, 440 meters closer) show double slapdown pulses. With this complication, the full factor of 2 is not applicable, and one would estimate instead an overshoot centered about 6.5 psi. That is the basis used hereinafter to infer accelerations.

4.3 Time Scales

Figure 4.11 compares in detail the time scale of the pressure waveforms measured in this project with the acceleration waveforms measured by Perret (pers. comm.). The lowest line shows first arrivals. The middle line shows the end of the first acceleration pulse with the difference between middle and lower line being effectively the velocity rise time. The top line is the time of arrival of the slapdown pulse.

All comparisons are quite good. The greatest variation occurs in the time of the slapdown pulse. A possible indication of azimuthal asymmetry is given by the fact that the Perret datum out of line at (SR = 2.17, t = 1.80) was his station SB-4 at the edge of the Bering Sea and not colinear with the other stations. The two pressure second pulses out of line are at lake BP (SR = 1.93, t = 1.68) and at lake DK-2 (SR = 2.20, t = 1.78), also not colinear with Perret's stations (see map, Figure 2.1). On the other hand lake DP was colinear with Perret's stations, being about 300 meters beyond S-6, and DP-1 and DP-2 time scales are in agreement with Perret's.

Additional evidence on the time scale is derived from documentary photography of lake DK and a nearby unnamed lake. This photography shows an initial white flash, a darkening, and then a long interval in which the surface of the water rises faster than the ground and takes on a white foamy appearance. At slapdown, the surface of the water increases its agitation, rising faster than before and with a more irregular and spiked appearance. These phenomena are roughly coincident with certain features of the measured pressures. The initial whitening appears to be a shock arrival. The darkening lasts through the period of positive pressure and upward acceleration, and is interpreted to result from smoothing of ripples as water accelerates the air above it. The long white period is construed to be a period of free fall during which surface tension and the deceleration of water by air above it cause the surface to lose its integrity and break up. Then, finally, the new agitation is at slapdown. Shortly after this the camera mounts broke, and no further photographic data are available.

4.4 Accelerations

In Figures 4.12, 4.13, and 4.14, vertical and radial peak accelerations derived from several sources are plotted against slant range. When available, both first and slapdown peaks are plotted. (The ERC data ensemble also had six AV data and three AR data beyond the range of this figure. These data have been omitted to avoid unduly compressing the close-in part of the curve; however, they were used in the fits.)

In Figure 4.12 the curve shown is the best linear fit to other data (Perret, 1972; West and Christie, 1971, ERC; Jackson, L^3, pers. comm.). Compared to this curve, or to the data points themselves, peak vertical accelerations measured by passive gages are almost all high; however, by nature, passive gages respond to the highest signal they see. It must then be presumed that the acceleration gages indicate slapdown signals, and the indicated values are more nearly in line with them.

Figure 4.13 contains two curves, a linear and a quadratic fit to the Perret, ERC, and L^3 data on radial acceleration. Compared either to these curves or to the other data points, peak radial accelerations from passive gages are grossly out of line. One might postulate that the gage mounts were at fault, since most of the gages were placed at the upper end of a pipe driven into the ground (Figure 2.3); however, the three gages that were bolted to concrete footings (see "⊗" in Figure 4.13) are just as far out of line.

All radial acceleration data were taken with Geotech gages (AG). Vertical acceleration data were also taken with Dynasciences gages (AD). If in Figure 4.12 the AD data were to be emphasized, it would be seen that their results are, to the eye, slightly more in line with the other data than are the AG gage data. In Table 4.1 both positive and negative peaks recorded by AG gages are noted. Many of the negative vertical peaks are unreasonably large: in principle negative peaks can be -1 g or even overshoot that, but not as far as the values given in Table 4.1. Negative vertical peaks for AD gages are not entered on Table 4.1; indications of downward acceleration were too low to measure.

This information casts doubt on the measurements made by AG gages.

4.5 Pressure Amplitudes

Since the pressure gages were in essence another kind of acceleration gage, accelerations have been inferred from the measured pressures by Eq. (4.2). The results are entered in Table 4.2, and are plotted in Figure 4.14 together with more

directly measured accelerations. On the five active pressure gage records, first and slapdown peaks are separately plotted as corrected (Section 4.2). It is evident that the five first peaks inferred from pressure gages line up extremely well with other first peaks, and thus appear to be quite valid. The scatter on the four second peaks from active pressure gages is like that of the eight second peaks obtained by Perret and L^3, and the two sets of second peak data intermingle. These data also appear to be valid.

In discussing peak accelerations derived from passive pressure gages, also plotted in Figure 4.14, the question arises as to whether there is a relation between pressures and/or accelerations and their location on Amchitka relative to the geological structure of the island, especially in view of the much-publicized concentration of cliff damage and uplift between two faults on the Bering coast. Figure 4.15 is a map of the central portion of Amchitka, showing also the main road, some of the lakes, and the principal faults mapped in this portion of the island (from USGS, 1972). The various points of measurement are indicated on Figure 4.15 by the same code as is used in Tables 4.1 and 4.2, and the actual accelerations and pressures converted to acceleration are indicated by the numbers next to these points.

The coastal damage area was from Banjo Point west. From there to where the Teal Creek Fault reaches the coast, rock and cliff falls and uplift of the intertidal bench are very evident. To the west of Teal Creek Fault, a weaker rock substrate resulted in a dominance of turf slides, except for massive rock fall at Petrel Point. Cliff damage on the Pacific Coast was minor.

A kilometer to the east of SZ is a cluster of lakes most of which were drained by tilting or cracks. These lakes are almost on the so-called Unnamed Fault, which is also the southeastern boundary of the strong effects area. Four of the lakes in this cluster were instrumented with passive pressure gages. Table 4.2 shows that three of these four were drained and one partly drained when the gages were recovered. Recovery was made after collapse of the cavity and additional surface disruption. Photographs taken before and after collapse indicate that lake DF was drained as a result of the primary shock, but lakes BO, DG, and DH still contained some water before collapse (Stephan, BMI, pers. comm.). In inferring accelerations from the indicated pressures, I chose to use the initial water depth, reasoning that the shock phenomena must be complete before the lakes could drain.

In Figure 4.12, after adjusting the slapdown pulse at DP-1 according to the reasoning of Section 4.2, five points remain which seem anomalously high and three anomalously low (Table 4.3).

Two of the eight anomalous pressures were in the cluster of drained lakes, DH and BO, lake DH being almost directly on the Unnamed Fault. According to EG&G aerial motion picture photography, all lakes within several kilometers of SZ (at least as far as DP) sprayed into the air at shot time. The field of view is not large enough to observe more distant lakes. Geysers or spouts in lakes were less common than at Long Shot or Milrow; none of the instrumented lakes contained a geyser except lake DH. Most geysering on land occurred on or near the Unnamed Fault. Geysers were also seen in the Bering Sea off the end of Teal Creek Fault.

Four of the anomalies were in streams. Indeed each of the three instrumented streams had at least one anomaly. In each case the gages were located in midflow. On recovery (after collapse) one of the gages in stream AH was buried by material that had washed downstream. According to the EG&G aerial photography, White Alice Creek and stream AH shot up into the air as a line of spray. These streams typically have heavy overgrowth on either side which renders them particularly susceptible to being squeezed from either side, hence the line of spray seen in photography. DE stream is short and drains BP lake; it is in the foreground of the photography where details are plain and did not appear to spray. BR stream is in the far distance of the photography, and one cannot tell whether it sprayed.

The low reading in AH stream is from the gage found buried. One suspects that the high readings from AH and BR streams are a consequence of the squeeze which caused the spraying. The fact that all three streams instrumented showed anomalous readings is itself indicative of an unexpected difficulty in monitoring pressure in streams.

The other coincidence that emerges from this investigation is that the two highest readings, those from AH stream and from DH lake, were from stations very close to each other, each almost on a mapped fault that underwent a great deal of disruption.

Four out of five anomalously high acceleration readings (five out of six if one includes an uncorrected DP-1) are accelerations inferred from pressures. This suggests that the overshoot discussed in Section 4.2 was a factor in these measurements--and thus probably also in others.

Perret located SF5S and SF5N gages straddling Teal Creek Fault and SF12S and SF12N gages over the so-called S12 fault. In each instance, the closer gage shows a weaker slapdown pulse than the far gage. This observation suggested examining the measured and inferred accelerations by structural block as in Figure 4.16. In this figure the ordinate is the ratio of the measured or inferred slapdown acceleration

to the average acceleration at that distance (the fit in Figure 4.12), and the abscissa is the distance normal to the strike of the cross-island faults shown in Figure 4.15. Perret's and the L^3 measurements, as standards for comparison, are connected with solid lines. The addition of data derived from passive acceleration gages and inferred from pressure gages, provides scatter that simply obscures the pattern. There remains, however, a tendency in adjacent blocks to have higher slap-down pulses at their near edges than at their far edges, both in an absolute sense and relative to the overall decrease with distance.

4.6 Pressures in the Sea

Plans to install pressure gages in the deep water off shore of Amchitka failed because a severe storm the day before the shot prevented deployment of the fish-holding pens on which the gages were to have been mounted. It is nevertheless of interest to reconstruct what the pressure magnitudes and waveshapes were in the sea, especially in view of the large and well-publicized sea otter mortality (Kirkwood and Fuller, 1972; for examples of news coverage see N. Y. Times: November 21, page 75; December 12, page 49; December 21, editorial page 26). Indications of any very fast changes in pressure on Cannikin are particularly important, for it has been repeatedly shown that drastic changes are much more damaging to biological systems than slow changes (e.g., White, et al, 1971).

A contour map of Cannikin (similar to Figure 3.37 for Milrow) with overpressures and water spall limit appears in Figure 4.17. The contours of peak positive overpressure at the ocean floor follow the rules:

$$\begin{aligned} PB &= 27800\ (SR)^{-1.6} && d > 250 \text{ ft} \\ &= 27800\ (SR)^{-1.6} \left(\frac{d}{250}\right) && d < 250 \text{ ft} \end{aligned} \qquad (4.3)$$

Above the ocean floor, pressures were less, and are obtained by substituting Z for d in Eq. (4.3). The 250 feet cut off on peak clipping is equivalent to a linear rise time of 110 msec, this time being derived from Perret's measurements as discussed in Section 3.8. In both instances, the back side of the velocity waveshape was assumed to be linear and go to zero in twice the rise time.

According to this reckoning, the water spall area on Cannikin is less extensive relative to the 100 psi contour than it was on Milrow. This is a direct consequence

of the longer rise time. On the other hand, another effect apparently took place on Cannikin that was almost absent on Milrow. According to Eq. (3.17), there can be a depth below which continuous distributed bulk cavitation takes place. That equation only has meaning if the depth it predicts is less than the depth of the water. Applying this principle as in Figure 4.18, we see that on Milrow the Eq. (3.17) depth is almost never less than the water depth, and that only along a narrow submarine canyon so that the area of the bottom over which this occurred is small, approximately coincident with the smallest 100-psi contour shown in Figure 3.37. On Cannikin, on the other hand, there is a considerable volume of water in which bulk cavitation took place. This bottom area is shown in the map of Figure 4.17.

Spall and resulting cavitation have two consequences that may be damaging biologically: the decompression itself or the pressure transients at the end of cavitation as bubbles collapse. Kenyon reports (1969) that sea otter gather their food from the ocean floor out to depths of 20 fathoms (36 m). According to Figures 4.17 and 4.18 there is a large volume of bulk cavitation within the 20 fathom contour. This may explain the large numbers of sea otter missing and presumed killed after Cannikin. Autopsies of animals recovered showed severe lung and spinal hemorrhages such as are typically found in explosive decompression (White, pers. comm.).

Measurements on Milrow on the PB2 and PH2 gages indicated that the ending of water spall and cavitation did not produce rapid pressure changes in water. According to Table 2.2 these instruments and their associated recording equipment had bandwidths of 220 and 330 Hz and were capable of detecting signals with rise times of 3 to 4.5 msec or longer; but no such signals appear in the records.

Following reasoning of Section 3.4, rock spall will not occur along the same range in rock under water as in dry rock. On land, according to Perret's waveforms (priv. comm.), spall extended out at least to a horizontal range of 18,000 feet (5.5 km), and according to the reasoning of some that the 1 g line is the limit, out to 8 to 10 km or 26 to 30,000 feet (see Figure 3.34). The latter figure is only half way between the 200 psi and the 100 psi contour in Figure 4.17, on the Bering Sea side of Amchitka. If spall under water at Cannikin went half as far as spall on land as at Milrow, then it reached the outer edge of the 300 psi contour in Figure 4.17. Thus only the close-inshore waters were affected by rock spall. Evidence from Milrow is that the ending of rock spall, water spall, and cavitation did not produce rapid pressure changes in water, the evidence being the lack of such signals on the Milrow W8 PB2 and W8 PH2 gages. I infer that these phenomena did not occur on Cannikin either.

4.7 Summary - Cannikin

In summary these observations may be made about the accelerations and pressures measured in this project on Cannikin:

1. These data are consistent with accelerations reported by Perret (1972), West and Christie (1971), and L^3 (pers. comm.).

2. A relationship is confirmed between acceleration and pressures measured in shallow ponds (Eq. (4.2)).

3. Pressures in shallow ponds resemble acceleration waveforms in having two pulses separated by a period of relief of weight of overlying water (free fall). The second pulse is typically strong and rapidly oscillating.

4. Pressure measurements in streams were by and large anomalous. Anomalously high peaks appear to be associated with squeeze forces as evidenced by line sprays from streams and geysering in lakes. Anomalous lows also were present.

5. Effects due to geologic structure are most evident in slapdown (spall-closure) pulses, in that a tendency for spall is stronger on the near side of a structural block than on the far side.

6. Pressures in the sea were not directly measured, but were inferred from surface motions measured on land using the theory confirmed on Milrow. A new occurrence on Cannikin was a large volume of bulk cavitation in water. This may explain the gross mortality of sea otter which was observed. As others have seen before, first acceleration peaks have less scatter than second or slap-down pulses.

7. Passive pressure gages apparently measured correctly, but the complex wave-shapes presented some ambiguity in interpretation. The passive pressure gages were less than satisfactory as acceleration gages; on the other hand, active pressure gages make good acceleration gages in ponds not subject to squeeze forces.

8. The passive accelerometers used are suspect. Pipe mounts used on AG gages were unsatisfactory.

References

AC Electronics - Defense Research Laboratories, 1969, Description of the Ganja Bottom Motion System, ACDRL Report S69-03, February 1969.

Cole, R. H., 1948, Underwater Explosions, Princeton U. Press (since reprinted by Dover, 1965).

Day, J. D., and D. W. Murrell, 1967, Vela Uniform Project Long Shot, Project 1.01, Ground and Water Shock Measurement, Report VUF-2701, Waterways Experiment Station, Corps of Engineers.

Environmental Research Corporation (ERC), 1970, Observed Seismic Data, Milrow Event, ERC report NVO-1163-199, March 1970.

Glasstone, S., 1962, The Effects of Nuclear Weapons, U. S. Government Printing Office.

Kenyon, K. W., 1969, The Sea Otter in the Eastern Pacific Ocean, U. S. Dept. of Interior No. Am. Fauna Series No. 68, U. S. Government Printing Office.

Kirkwood, J. B., 1970, Amchitka Bioenvironmental Program. Bioenvironmental Safety Studies, Amchitka Island, Alaska. Milrow D+2 Months Report, Battelle Report BMI-171-126, March 20, 1970.

Kirkwood, J. B., and R. G. Fuller, 1972, Amchitka Bioenvironmental Program. Bioenvironmental Safety Studies, Amchitka Island, Alaska. Cannikin D+2 Months Report, Report BMI-171-147, Battelle Memorial Institute.

Koh, R. C. Y., and D. Rosenkranz, 1970, Ocean Surface Effects Generated by a Nearby Underground Explosion at the Amchitka Test, Report NVO-289-6-1, Tetra Tech, Inc.

Merritt, M. L., 1969a, Ground Motion Predictions for Amchitka, Report SC-RR-69-376, Sandia Laboratories.

Merritt, M. L., 1969b, Underwater Motion and Overpressures, Milrow Event, Report SC-TM-69-773, Sandia Laboratories.

Merritt, M. L., 1970, Physical and Biological Effects, Milrow Event, Report NVO-79, Atomic Energy Commission.

Merritt, M. L., 1971, "Ground Shock and Water Pressures from Milrow," Bioscience Vol. 21, No. 12, 696-700.

Merritt, M. L., 1972, "Reaction of Shallow Onshore Waters to Ground Shock," Bull. Seism. Soc. Am., to be published (also SC-DC-71-4486).

Perret, W. R., 1972, "Cannikin Close-in Ground Motion and the Motion Induced by Milrow," Bull. Seism. Soc. Am., to be published (SC-DC-71-4471).

Perret, W. R., and D. R. Breding, 1972, Ground Motion in the Vicinity of an Underground Nuclear Explosion in the Aleutian Islands: Milrow Event, Sandia Laboratories Report SC-RR-71-0668, May 1972.

U. S. Geological Survey, 1972, Geologic and Hydrologic Effects of the Cannikin Underground Nuclear Explosion, Amchitka Island, Aleutian Islands, Alaska, Report USGS-474-148, June 1972.

References (cont)

Valdez, R. A., and W. T. Helm, 1971, "Ecology of Threespine Stickleback Gasterosteus aculeatus L. on Amchitka Island, Alaska," Bioscience Vol. 21, No. 12, 641-645.

West, L. R., and R. K. Christie, 1971, Observed Ground Motion Data, Cannikin Event, ERC Report NVO-1163-230, December 1971.

White, C. S., R. K. Jones, E. G. Damon, E. R. Fletcher, and D. R. Richmond, 1971, The Biodynamics of Airblast, Report DNA-2738T, Lovelace Foundation, Albuquerque.

TABLE 2.1

Locations of Instruments on Milrow

Station	Horizontal Range (ft)	Slant Range (ft)	Water Depth (ft)	PB Depth (ft)	PI Depth (ft)	PH Depth (ft)	Other Measurements
W8	8,440	9,250	80	75.5	-	25.5	AVRT, UVRT
W13	13,550	14,080	40	35.5	-	19.5	AVRT, URVT
W16	16,035	16,480	65	60.5	-	27.5	AVRT, UVRT
W20	19,710	20,060	117	112.5	85.5	36.5	AVRT, UVRT
W23	22,820	23,110	209	204.5	134.5	35	AVRT, UVRT

NOTE: PB, PI, and PH indicate near-bottom overpressure, overpressure at intermediate depth, and overpressure at least depth, respectively. AV, AR, AT, UV, UR, UT indicate vertical, horizontal radial and tangential components of acceleration, and the same components of velocity, respectively. The notations W8, W13, W16, W20, and W23 are meant to suggest measurements in water (W) at horizontal ranges of the indicated number of kilofeet.

TABLE 2.2

Channel Assignments and Bandwidths
Milrow Underwater Instrumentation

IRIG Channel Number	Gage	Carrier Frequency (Hz)	Bandwidth (Hz)	Commutator Filter (Hz)
7	PI	2,300	35	
8	PH1	3,000	45	14
9	PB1	3,900	60	35
10	UV	5,400	80	35
11	UR	7,350	110	14
12	UT	10,500	160	
13	PB2	14,500	220	
14	PH2	22,000	330	
15	AV	30,000	450	
16	AR	40,000	600	
17	AT	52,500	790	
E	Commutator	70,000	2100	

TABLE 3.1

Milrow Underwater Data

Gage	Horiz. Range (ft)	Water Depth (ft)	Gage Depth (ft)	Arrival Time (sec)	Acceleration (g) 1	Acceleration (g) 2	Velocity (ft/sec) 1	Velocity (ft/sec) 2	Displacement (in.)	Pressure +	Pressure −	Preshot Ambient Pressure
W8 AV	8,440	80		0.729	3.21	-	(5.0)	(-3.7)				
AR					0.31	-	-	-				
AT					-0.15	+0.25	(-0.1)	(+0.1) (+0.3)				
UV							5.09	-3.87	(7.0)			
UR							0.45	+0.8	(4.9)			
UT							-0.1	+0.06 +0.2	-			
PB1			75							129	83	48
PB2			75							148	51	48
PH1			25							50	27	26
PH2			25							53	23	26
W13 AV	13,550	40		1.11	1.62		(3.0)	(-1.85)				
AR					(0.3)		(0.75)	(1.1)				
AT					0.3		(0.42)	(-0.6)				
UV							3.82	-2.41	(5.4)			
UR							0.78	+1.0	-			
UT							0.48	-0.6	(1.5)			
PB1			35							35	20	30.5
PB2			35							35	22	30.5
PH1			19							22	13	23
PH2			19							21	14	23
W16 AV	16,035	65		1.302	1.76		(2.82)	(-1.4)				
AR					0.17	-0.03	(0.24)	(1.5)				
AT					-		(-0.8)	(1.2)				
UV							3.07	-1.41	(3.4)			
UR							0.3	+1.57	(5.2)			
UT										No record		
PB1			60							53	29	42
PB2			60							44	36	42
PH1			27							25	18	27
PH2			27							29	19	27
W20 AV	19,710	117		1.618	1.08		(2.03)	(-0.9)				
AR					0.23	-0.19	(0.35)	(0.7)				
AT					0.03	-0.1	(0.05)	-				
UV							2.22	-1.55	(2.9)			
UR							0.45	0.80	(3.2)			
UT							0.03	-0.1 0.35	(0.64)			
PB1			112							73	70	65
PB2			112							79	65	65
PI			87							68	57	54
PH1			36							25	27	31
PH2			36							No record		
W23 AV	22,820	209		1.793	0.61		(1.18)	(-0.88)				
AR					0.19		(0.4)	(0.95)				
AT					0.023	-0.115	(0.03)	(-0.2)				
UV							1.20	-1.23	(2.13)			
UR							0.45	0.96	(2.6)			
UT							0.025	-0.25	(-0.4)			
PB1			204							Record invalid		
PB2			204							69	93	106
PI			134							50	73	75
PH1			35							17	22	30.5
PH2			35							11	18	30.5

Note: A number in parentheses, such as (5.0) indicates a value determined by integration.

TABLE 4.1

Cannikin Peak-Reading Accelerometers

Location	Coordinates (m) N	Coordinates (m) E	HR (km)	SR (km)	θ (deg)	AV (g) +	AV (g) -	AR (g) +	AR (g) -	AT (g) +	AT (g) -	Gage Type
BP Lake	4,760	6,720	0.70	1.92	36	22.5	~ 0					AD30
S3	4,340	5,370	0.97	2.03	278	29	~ 0					AD50
CTB20	2,960	6,490	1.24	2.18	171	14.8	-13.7	16.0	-14.3	no cal		AG10
DK Lake	5,390	5,880	1.28	2.20	337	>30	~ 0					AD30
DE Stream	5,240	7,410	1.51	2.34	47	16	~ 0					AD20
AH Stream	3,410	7,670	1.55	2.37	159	19	~ 0					AD30
C4	5,010	7,660	1.57	2.38	60	15.5	- 8.9	11.9	-13.9	14.8	-18.6	AG10
STP	5,215	4,840	1.80	2.54	304	14.9	-11.8	7.2	- 2.7	2.1	- 2.6	AG10
S6	5,240	4,835	1.82	2.55	305	not valid						AD15,20,30
C5	4,435	8,680	2.37	2.97	85	17.5	- 9.7	no cal		11.8	- 9.6	AG10
C2	6,480	5,280	2.52	3.09	336	12.8	- 2.1	15.7	-11.2	8.8	9.35	AG10
BR Stream	2,100	4,274	2.92	3.43	227	14.5	~ 0					AD15
S12	6,170	3,580	3.38	3.83	306	12.0	- 6.8	13.2	-17.6	18.7	- 6.9	AG10
C7	2,330	3,160	3.67	4.08	239	7.7	- 2.0	3.0	- 6.1	6.9	- 5.6	AG5
Microwave	3,055	10,020	3.87	4.26	103	17.0	- 5.2	13.5	-10.0	7.2	- 8.0	AG10
Em-Lake	6,470	3,170	3.89	4.28	306	10.7	- 3.1	11.0	-10.2	11.9	-15.7	AG10
Em-Lake	6,480	3,100	3.95	4.34	306	15.7	- 4.0	11.5	-14.9	5.5	- 1.2	AG10
C3	5,800	4,640				lost						AG10
C1	8,330	3,060	5.28	5.57	322	2.4	- 1.1	2.0	- 3.6	3.4	- 2.4	AG2
S18	7,675	2,240	5.37	5.66	311	8.5	- 2.2	5.6	- 7.5	3.9	- 7.1	AG5
C6	3,920	12,160	5.84	6.11	92	7.4	- 2.0	7.9	- 5.6	7.2	- 6.9	AG5
S33	11,415	-1,200	10.43	10.59	314	1.2	- 0.8	no reading		0.2	0.3	AG2

Notation:

HR - horizontal range
SR - slant range
θ - azimuth
AV - vertical peak acceleration
AR - radial peak acceleration
AT - tangential peak acceleration

TABLE 4.2

Cannikin Pressure Gage Results

Location	Coordinates (m) N	E	HR (km)	SR (km)	θ (deg)	Depth (cm)	t_a (sec)	P_1 (psi)	P_2 (psi)	A_1 (g)	A_2 (g)	Gage Type	P_3 (psi)	A_3 (g)
BP Lake	4760	6760	0.72	1.93	37	50 to 38	0.499	8.5	16.9	11.6	23	PL50		
						50 to 38			14.4		19.6	PV50		
	4820	6800	0.79	1.96	37	50 to 38			11.2		15.4	PV30		
BO Lake	4100	7140	0.82	1.97	98	45 to 0			7.25		11	PV20		
DH Lake	3660	7080	0.92	2.01	125	35 to 23			29.6		57	PV50		
DF Lake	3950	7300	1.01	2.06	106	50 to 0			16.6		22.6	PV50		
DG Lake	3780	7430	1.18	2.14	110	45 to 15			14.		21	PV30		
DK2 Lake	5390	5867	1.29	2.20	339	75	0.578	8.4	41.	7.6	37	PL50	22	20
						75			25.5		23	PV30		
DK1 Lake	5460	5710	1.41	2.28	334	45	0.606	13.2	-	20	-	PL50		
DO Lake	2760	6560	1.45	2.30	168	50			26.		35.4	PV30		
DE Stream	5240	7410	1.51	2.34	45	25			6.9		19	PV30		
						25			1.75		4.8	PV30		
AH Stream	3410	7670	1.55	2.37	299	30			25.25		57	PV30		
						30 buried			3.25		7.3	PV30		
DP1 Lake	5340	4570	2.10	2.76	303	45	0.708	4.75	30.8	7.2	47	PL50	15.5	23.4
						45			23.25		35	PV30		
DP2 Lake	5400	4550	2.15	2.80	304	75	0.727	5.82	8.5	5.3	7.7	PL50	6.5	5.9
BR Stream	2100	4270	2.92	3.43	224	45			15.9		24	PV30		
						45			>10.		>15	PV10		
S12 Lake	6270	3660	3.38	3.83	309	30			4.08		9.3	PV10		
Emerald Lake	6510	3185	3.91	4.30	307	90			9.7		7.3	PV10		
S18 Lake	7075	2390	4.88	5.20	306	25			8.75		24	PV10		

NOTATION:

HR = horizontal range
SR = slant range
θ = azimuth
t_a = first arrival time
P_1 = amplitude of first pressure pulse
P_2 = amplitude of slapdown pulse or peak measured by passive gage
P_3 = pressure with overshoot removed
A_1 = acceleration inferred from first pulse
A_2 = acceleration inferred from second pulse or peak
A_3 = acceleration inferred from P_3
PV = validyne passive pressure gage of range in psi indicated
PL = pace active pressure gage of range in psi indicated

Coordinates are relative to N 5,700,000
E 640,000
UTM grid

TABLE 4.3

Cannikin Acceleration Anomalies

	SR (km)	P (psi)	(g)
	High		
AH stream	2.37	25	57
DH lake	2.01	30	57
BR stream	3.43	16	24
Microwave station	4.26		30
S18 lake	5.20	9	24
	Low		
BO lake	1.97	7	11
DE stream	2.34	1.7	5
AH stream	2.37	3	7

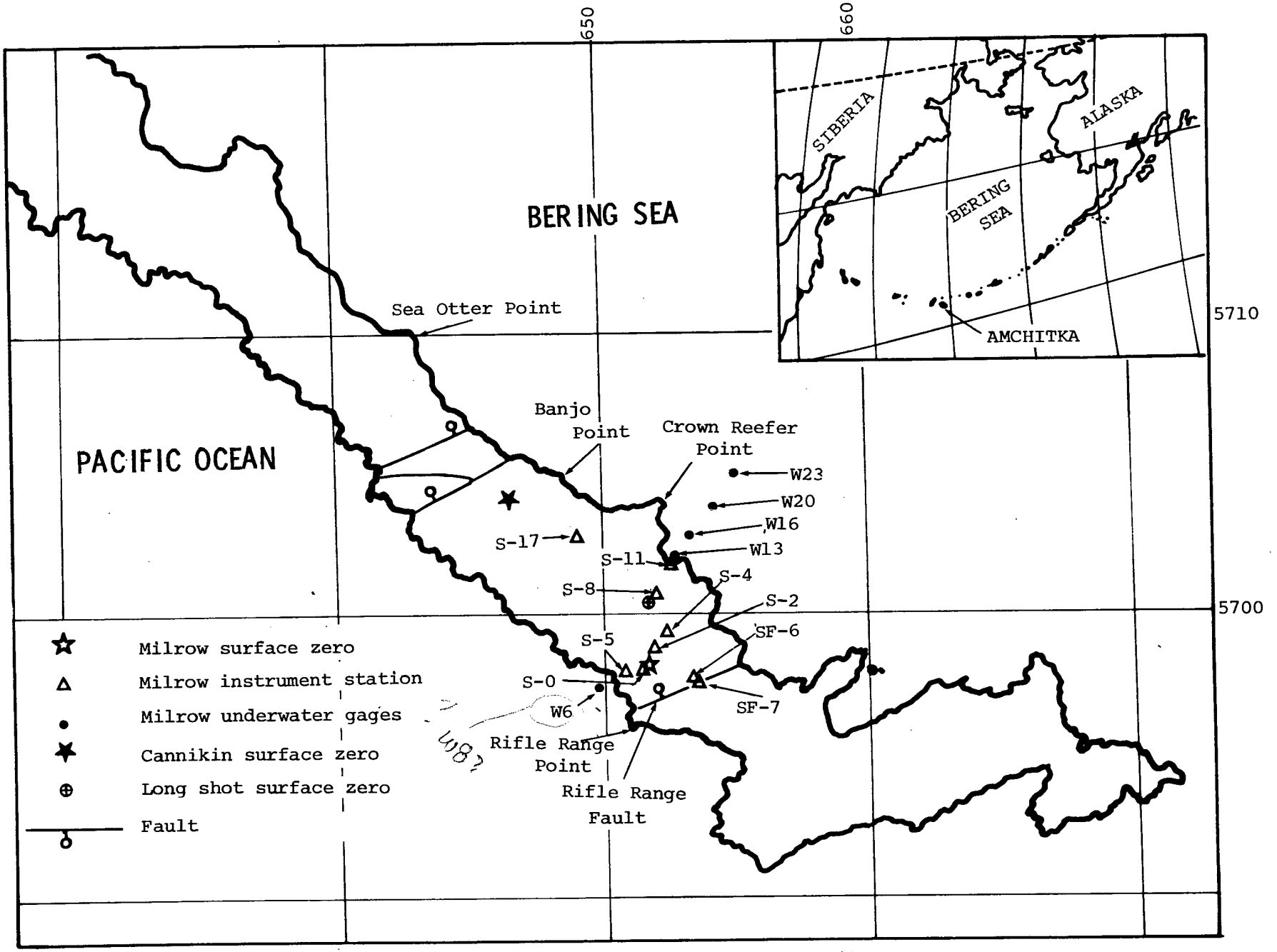

Figure 2.1 Instrumentation layout -- Milrow

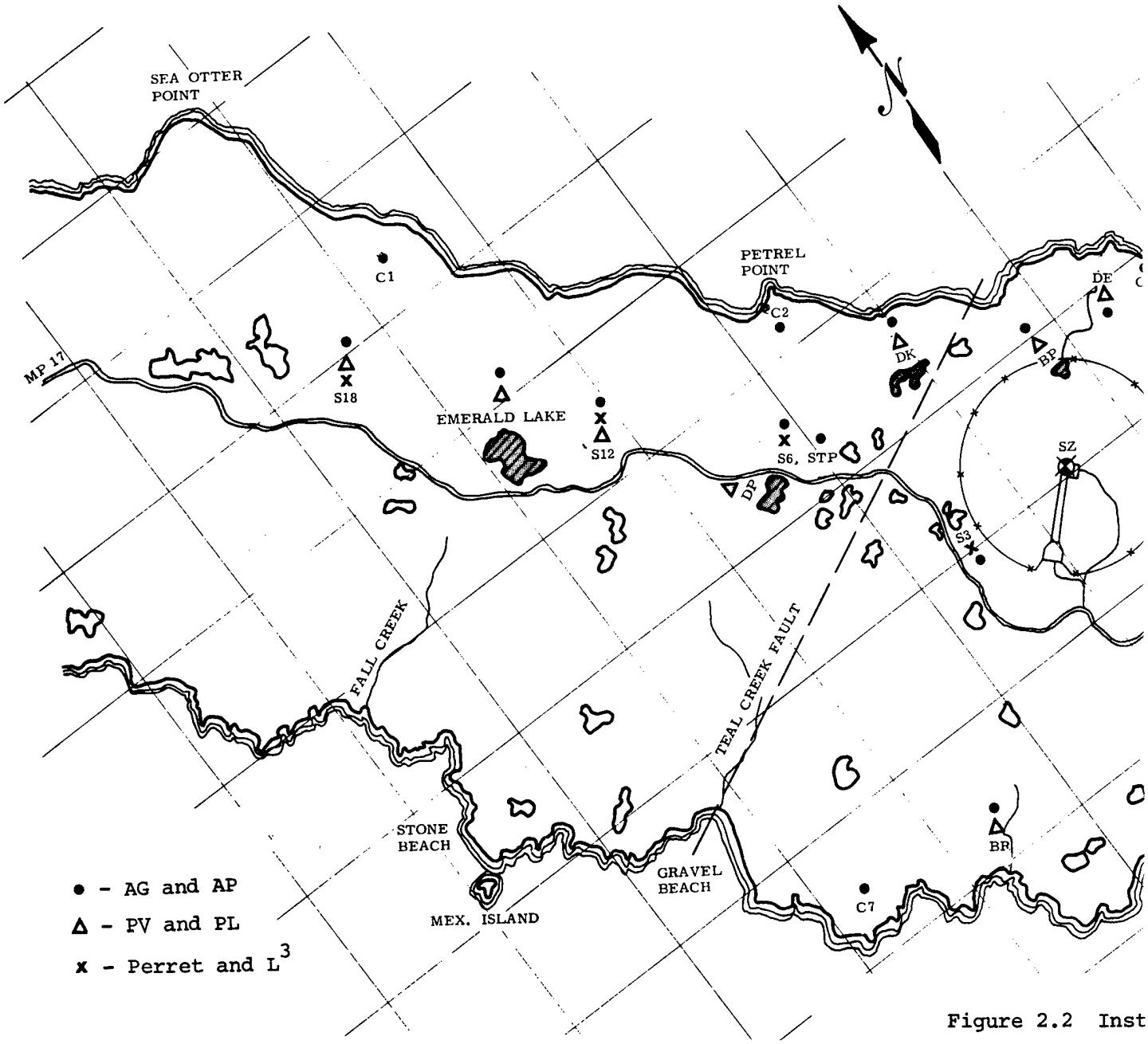

Figure 2.2 Inst

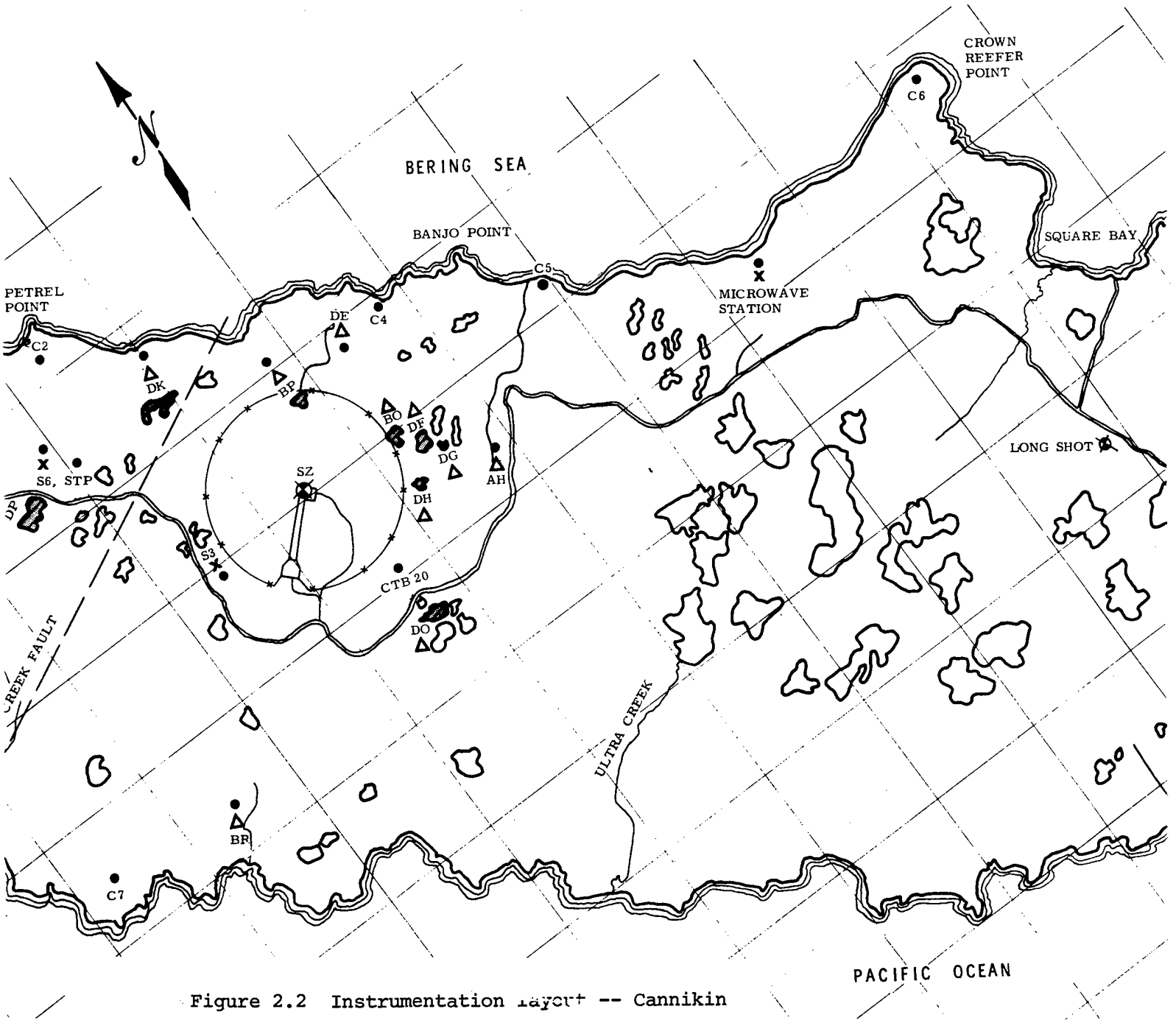

Figure 2.2 Instrumentation layout -- Cannikin

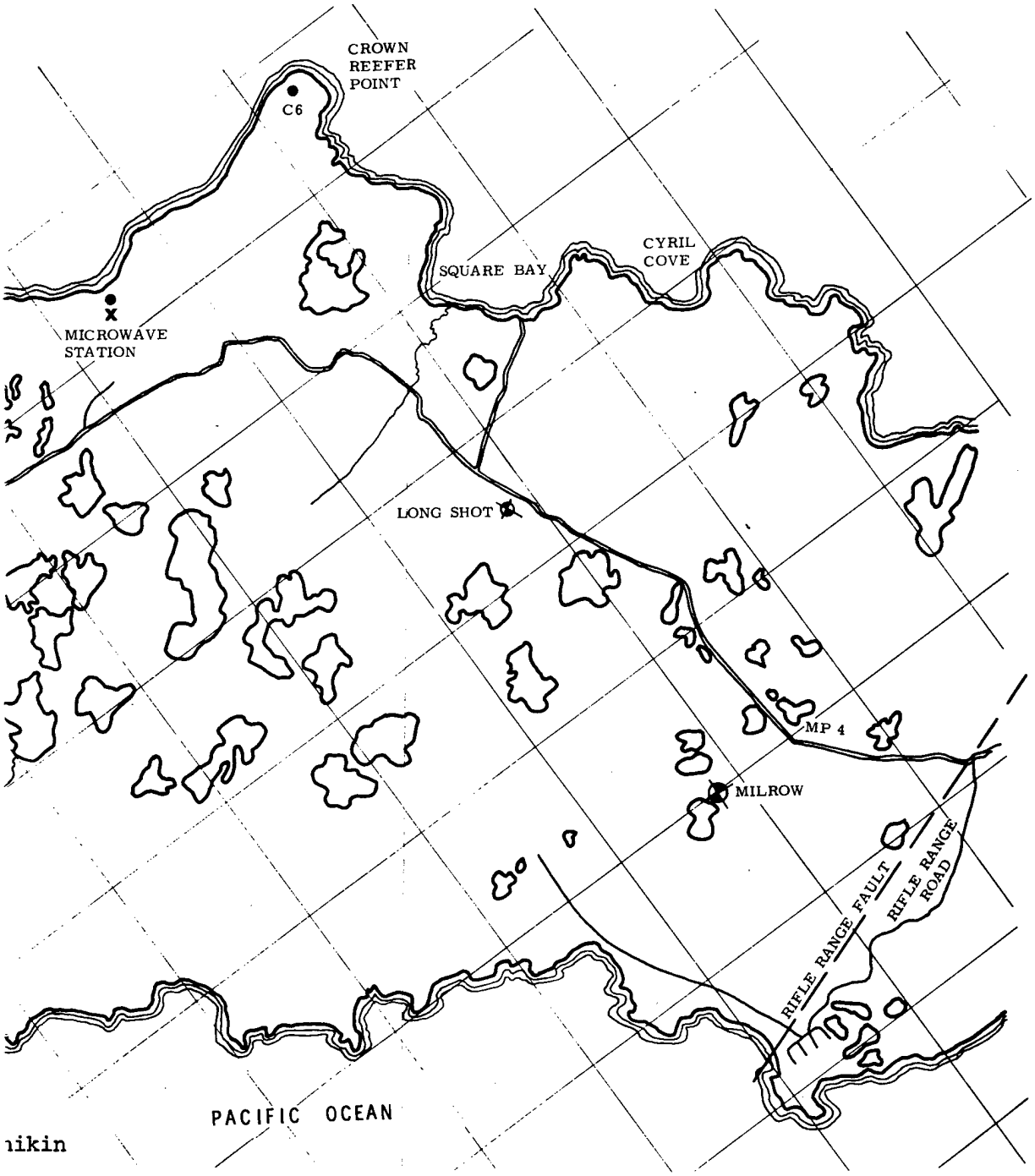
CROWN
REEFER
POINT
C6
SQUARE BAY
CYRIL
COVE
MICROWAVE
STATION
LONG SHOT
MP 4
MILROW
RIFLE RANGE FAULT
RIFLE RANGE
ROAD
PACIFIC OCEAN
ıikin

49-50

Figure 2.3

Teledyne passive accelerometer mounted on a pipe

Figure 2.4

Teledyne passive accelerometer bolted onto existing concrete pads

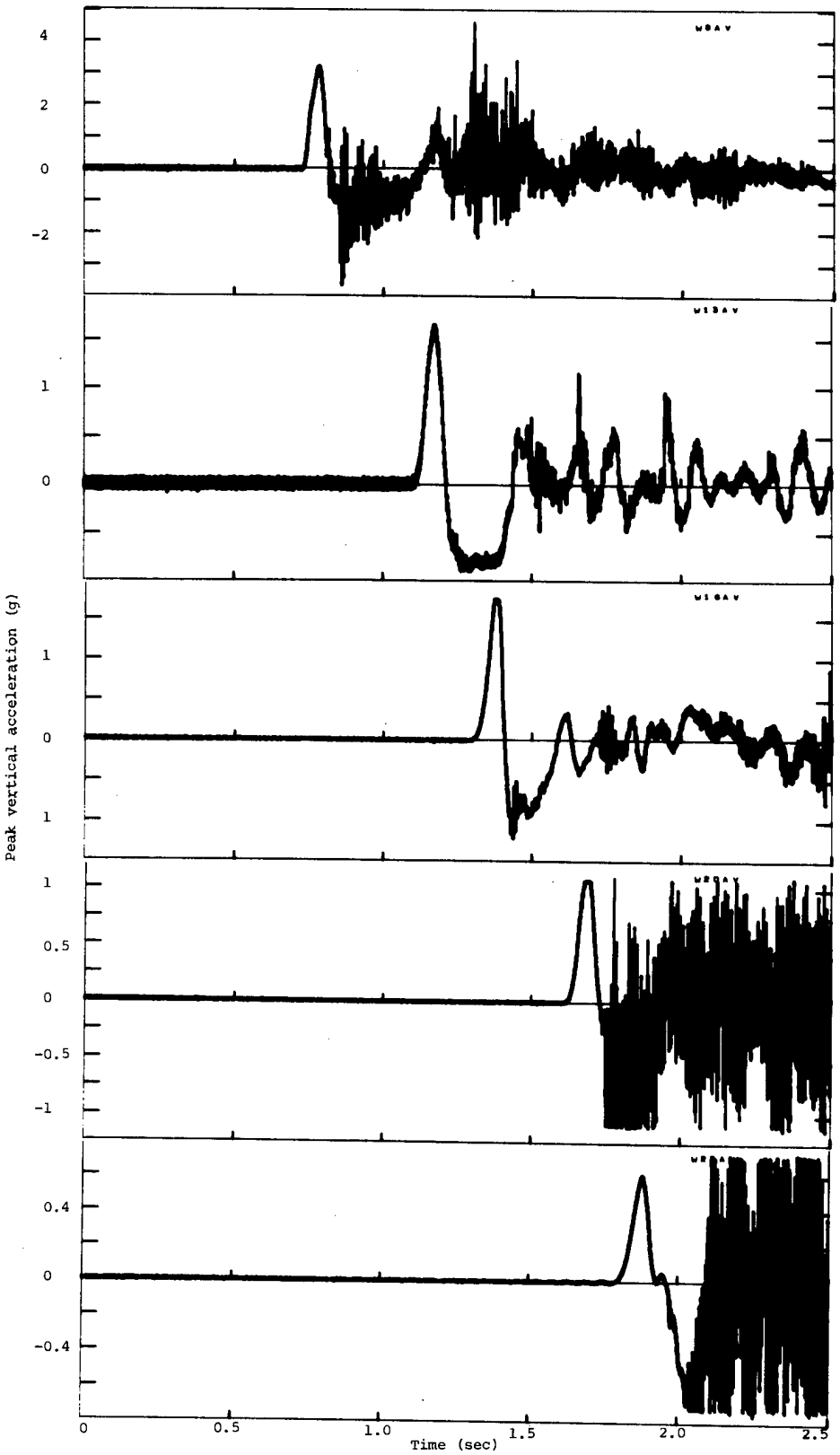

Figure 3.1 Vertical acceleration -- Milrow

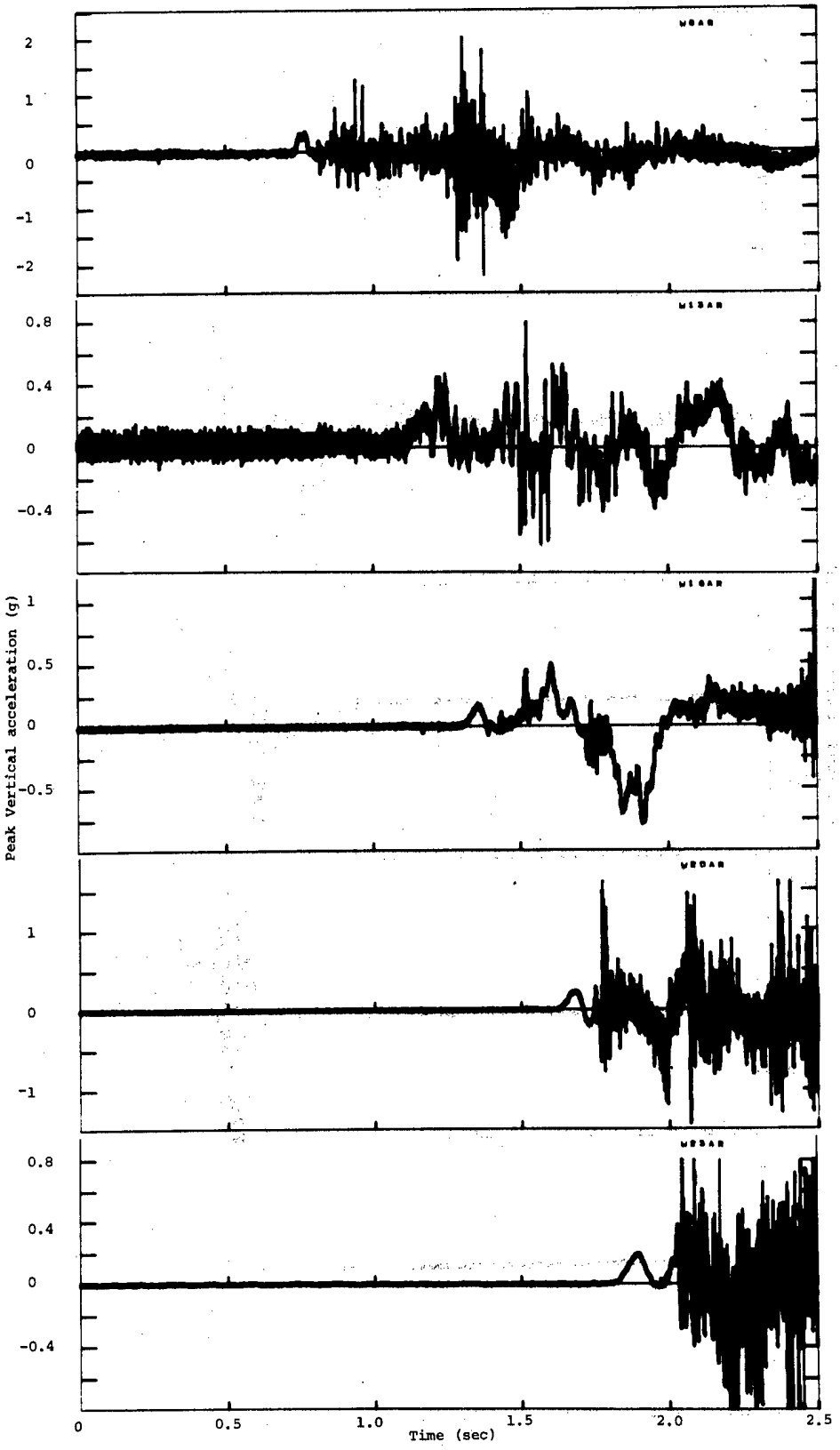

Figure 3.2 Radial accelerations

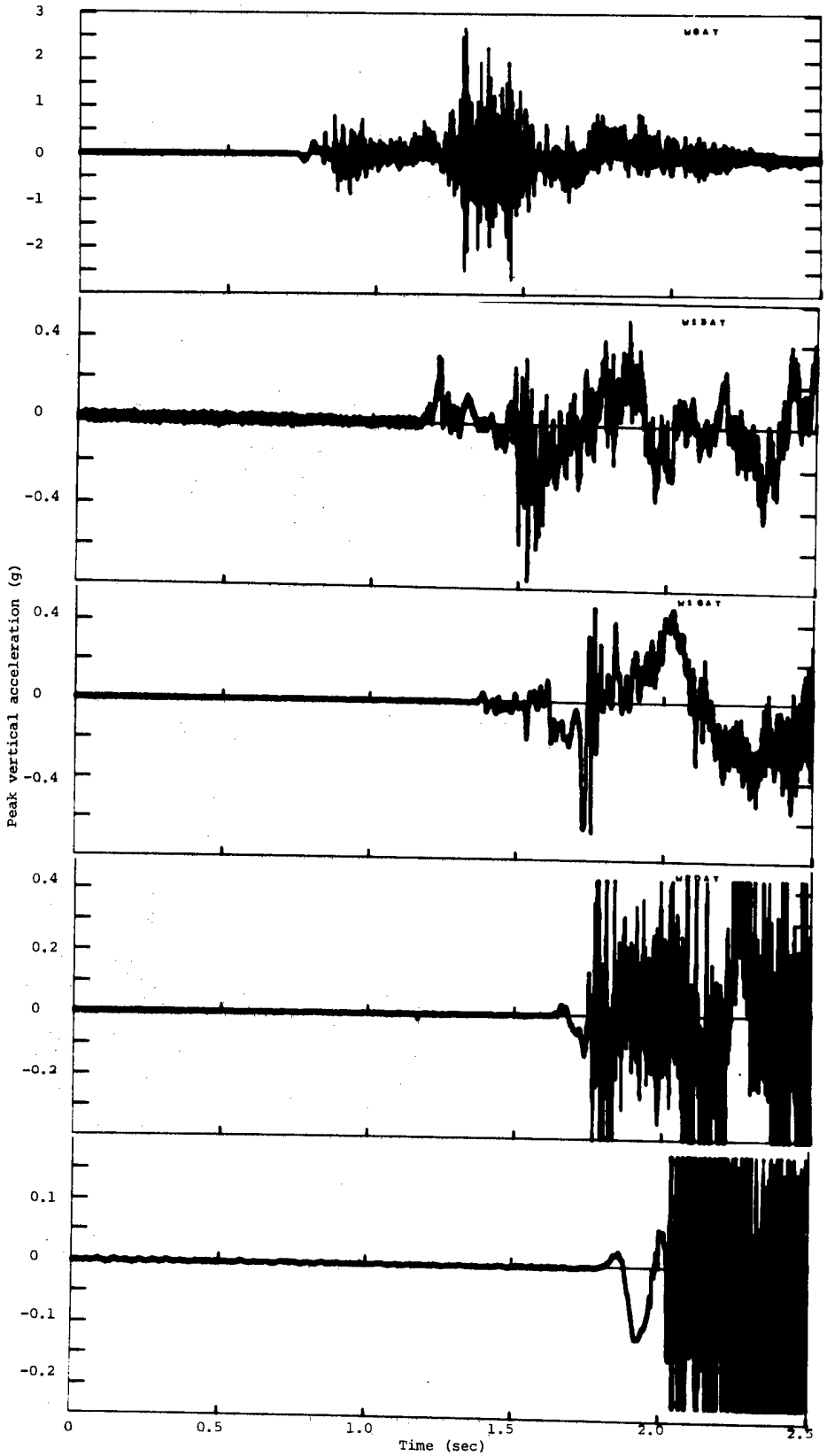

Figure 3.3 Tangential accelerations

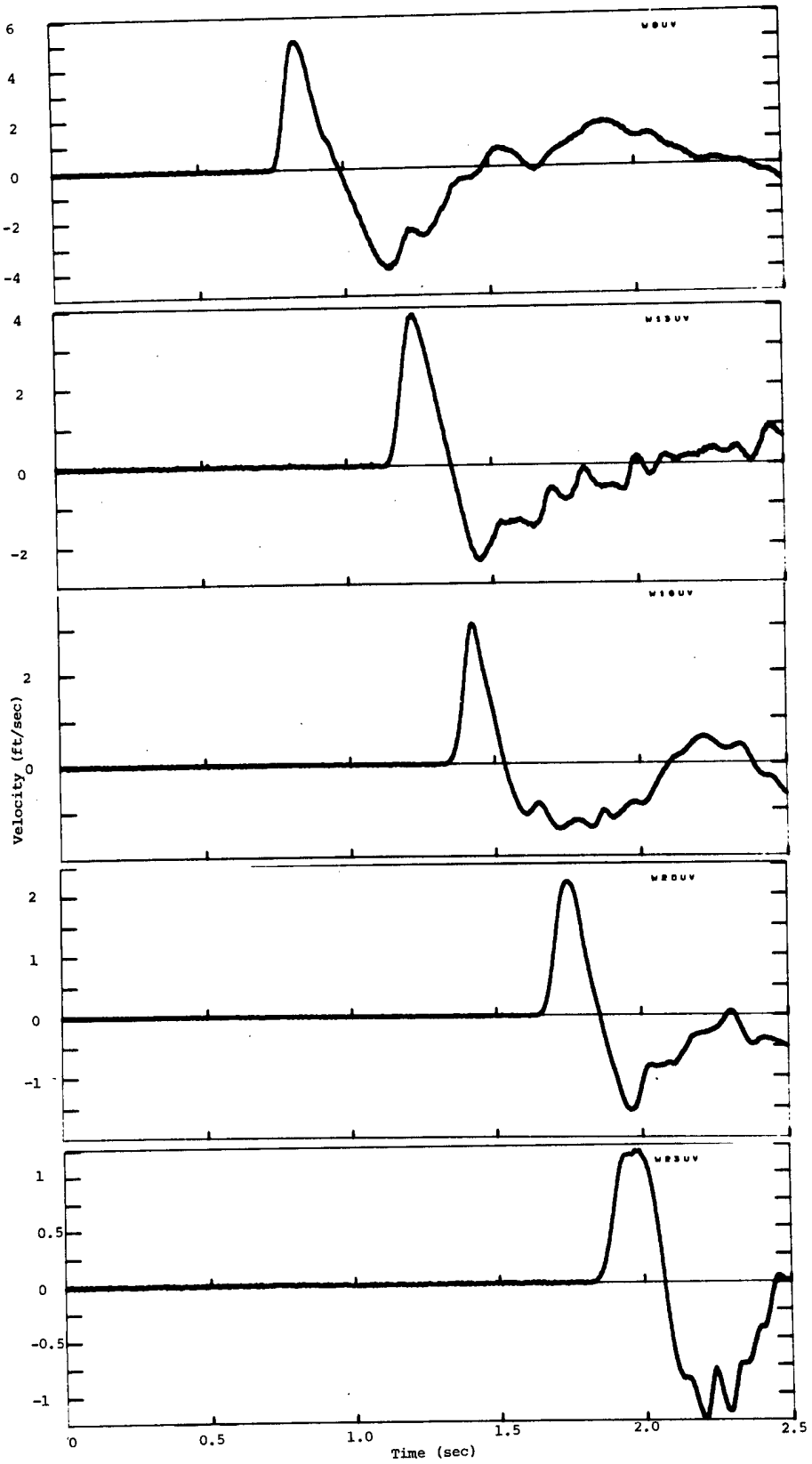

Figure 3.4 Vertical velocities

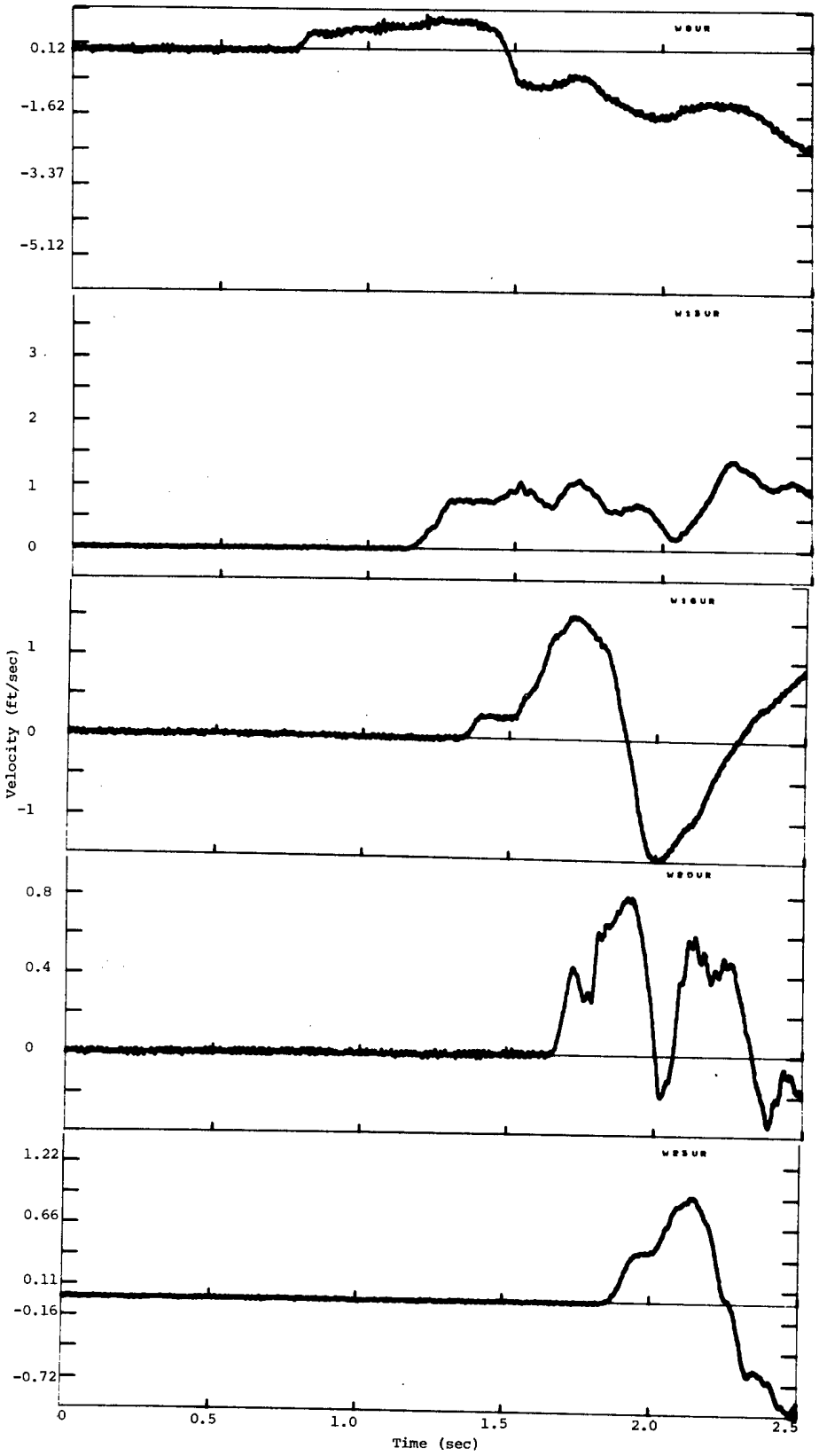

Figure 3.5 Radial velocities

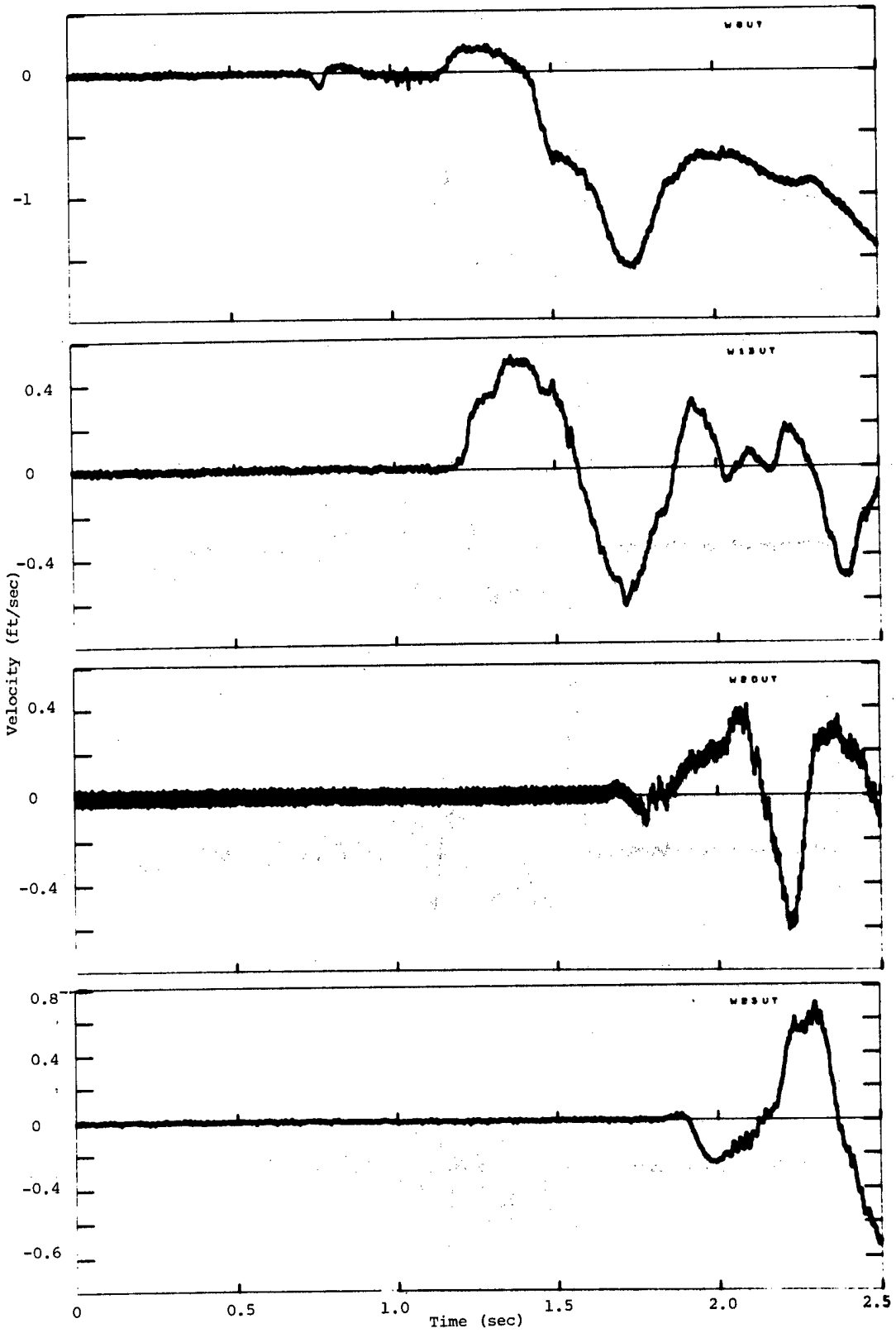

Figure 3.6 Tangential velocities

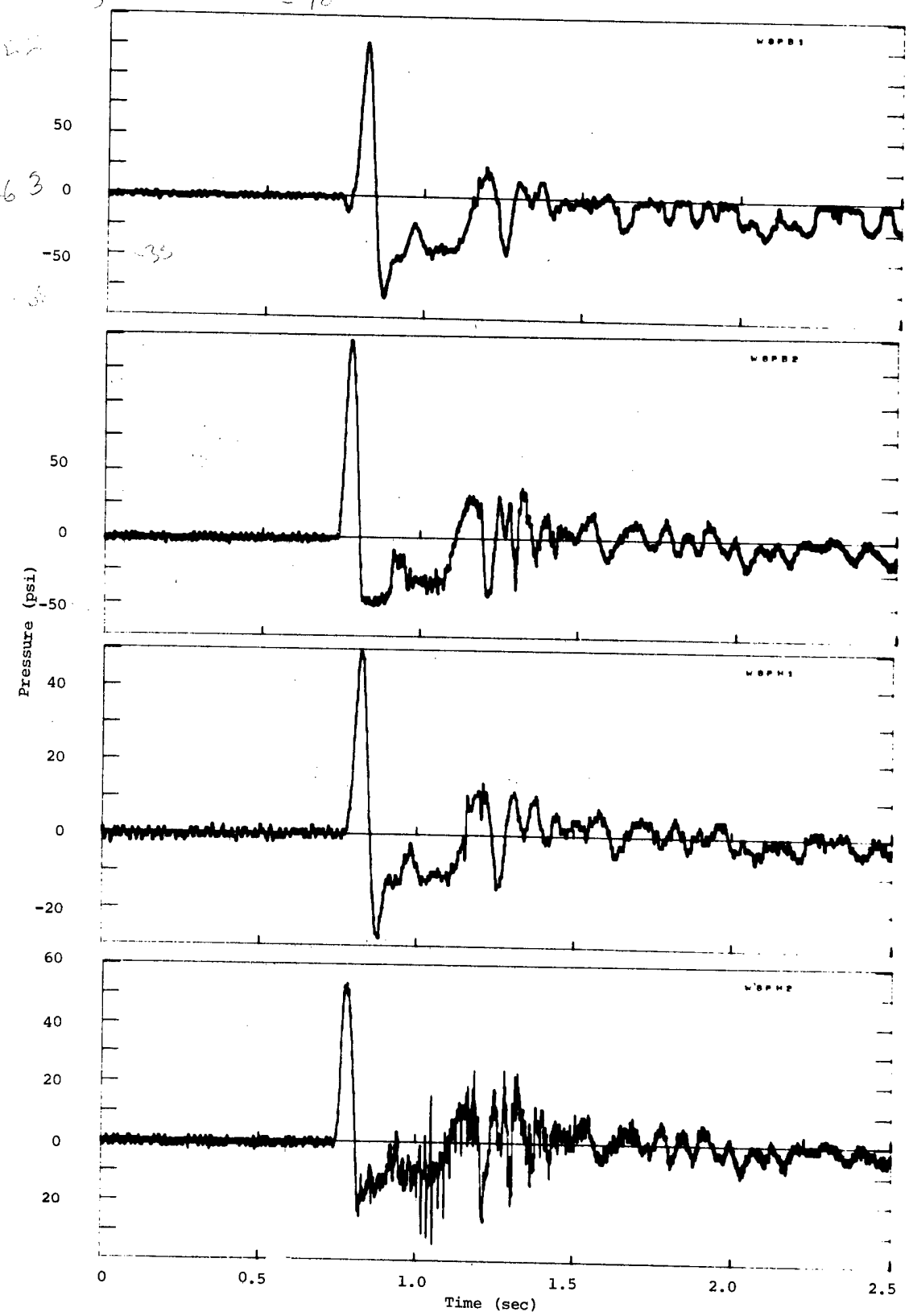

Figure 3.7 Pressures at station W8

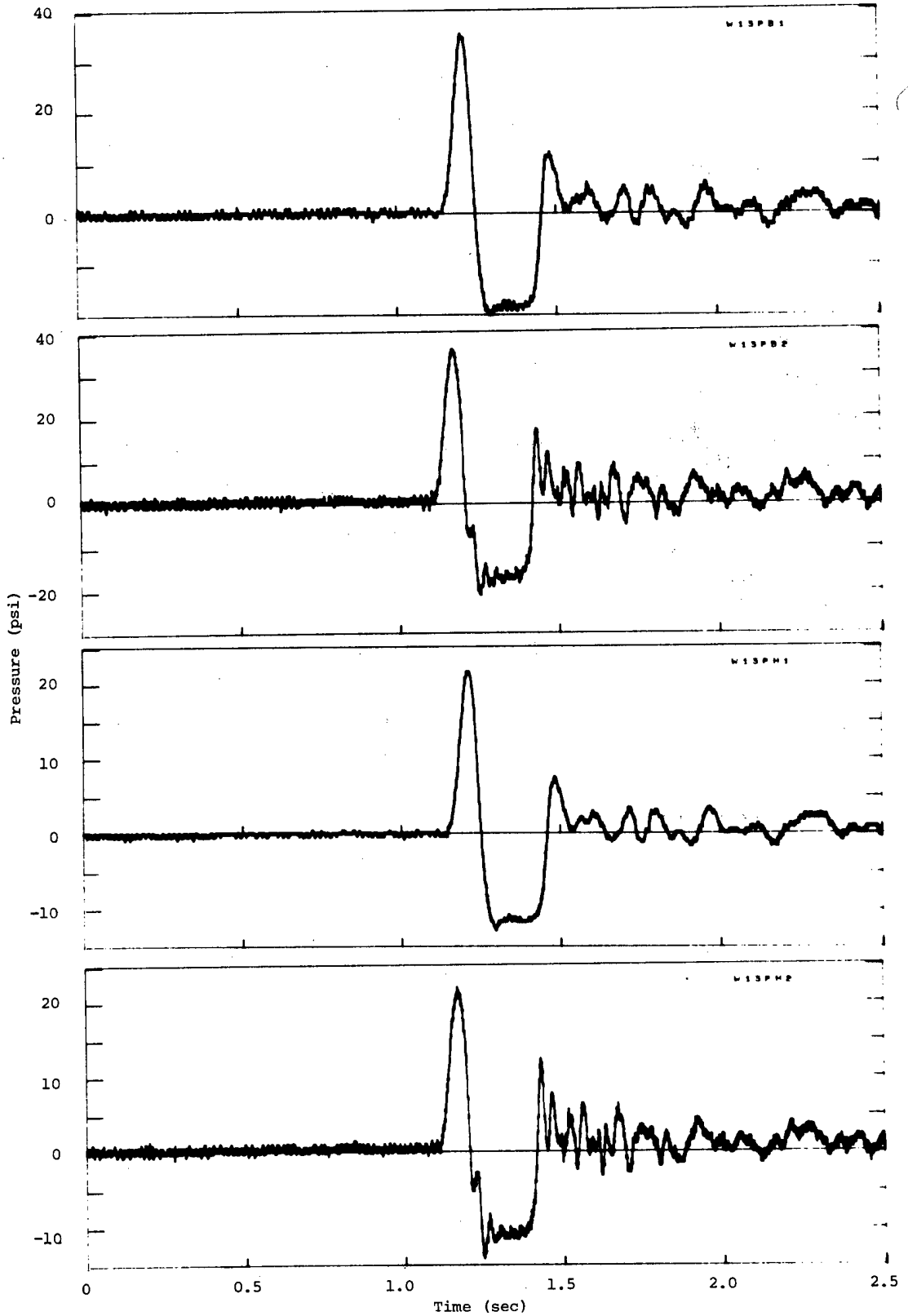

Figure 3.8 Pressures at station W13

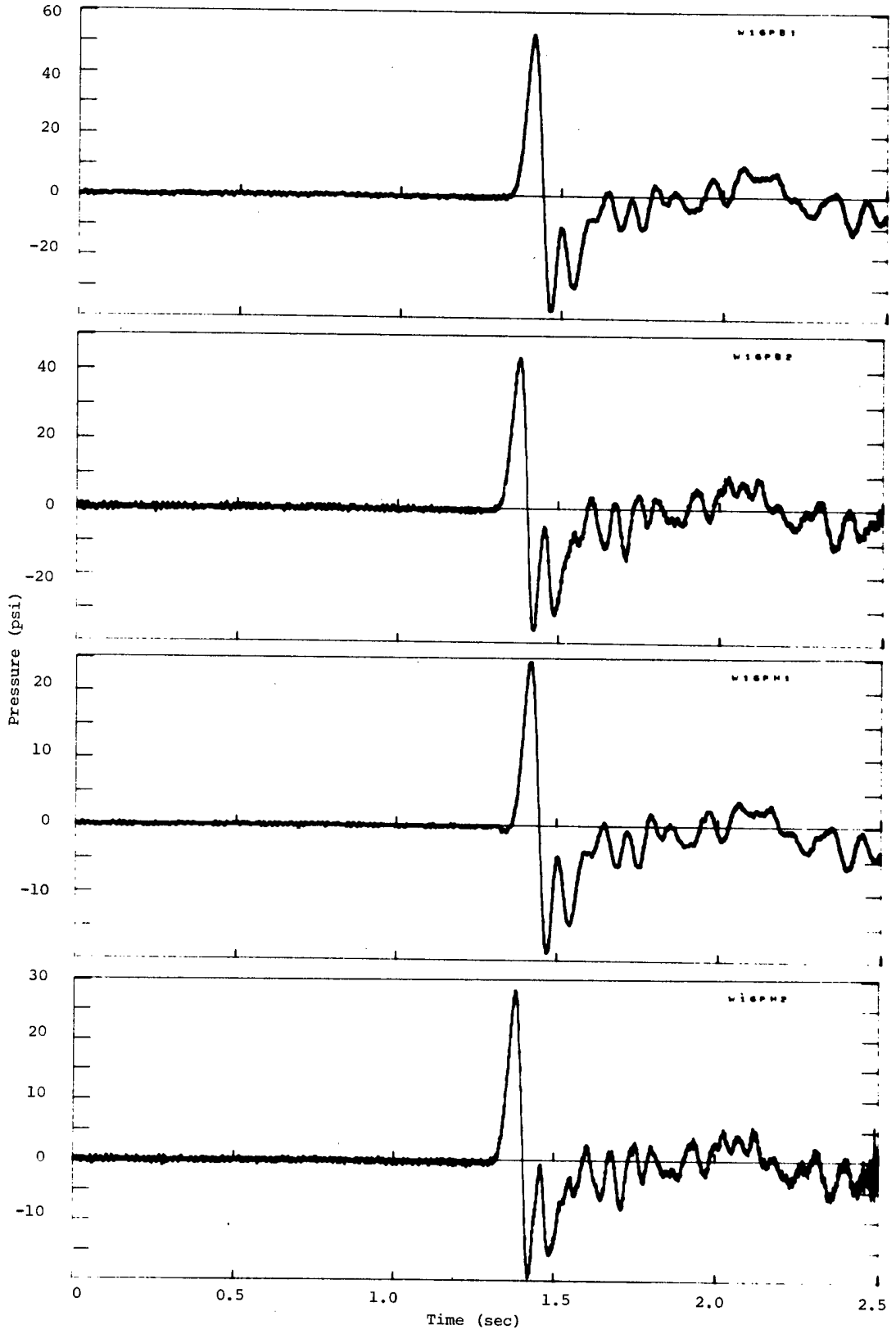

Figure 3.9 Pressures at station W16

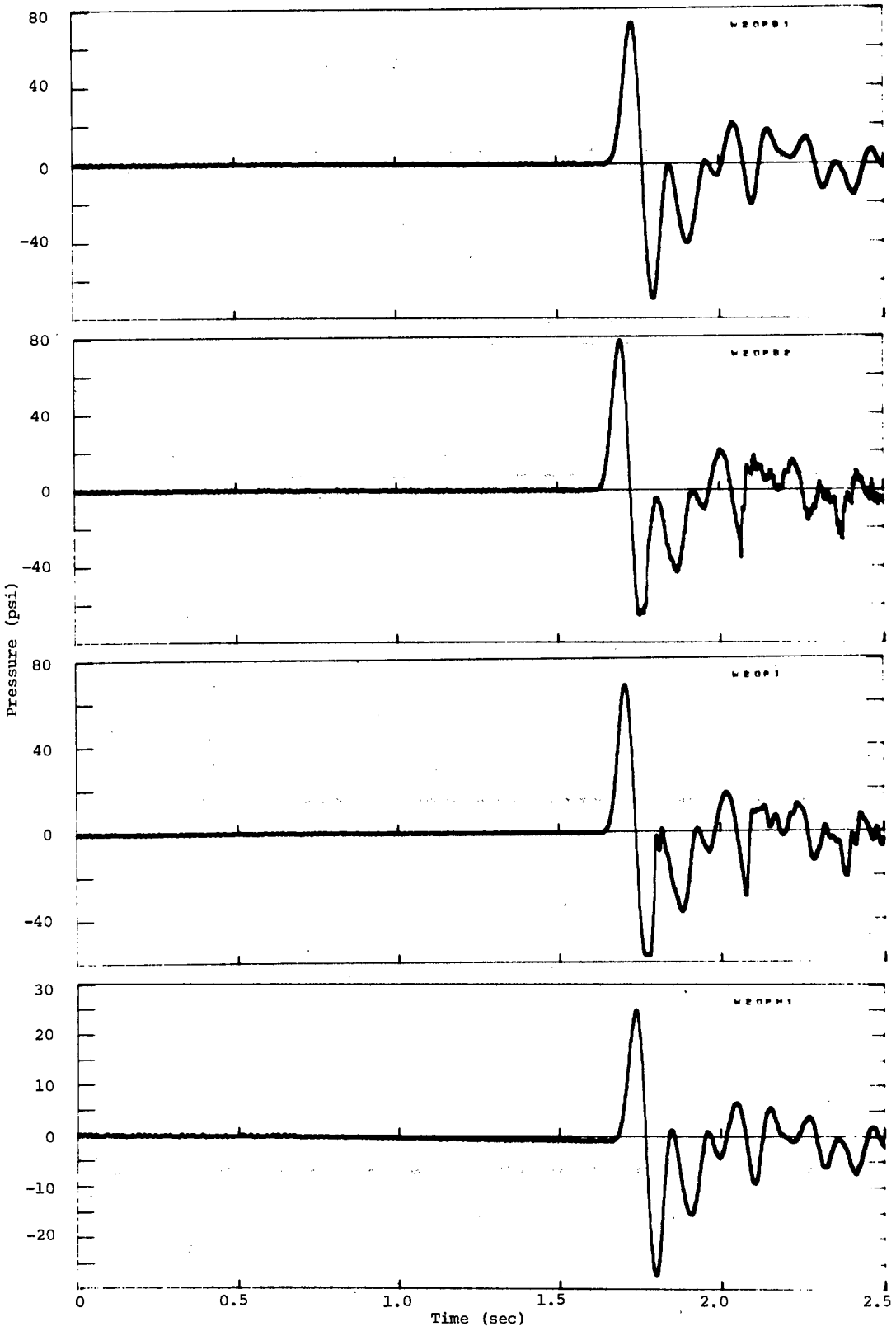

Figure 3.10 Pressures at station W20

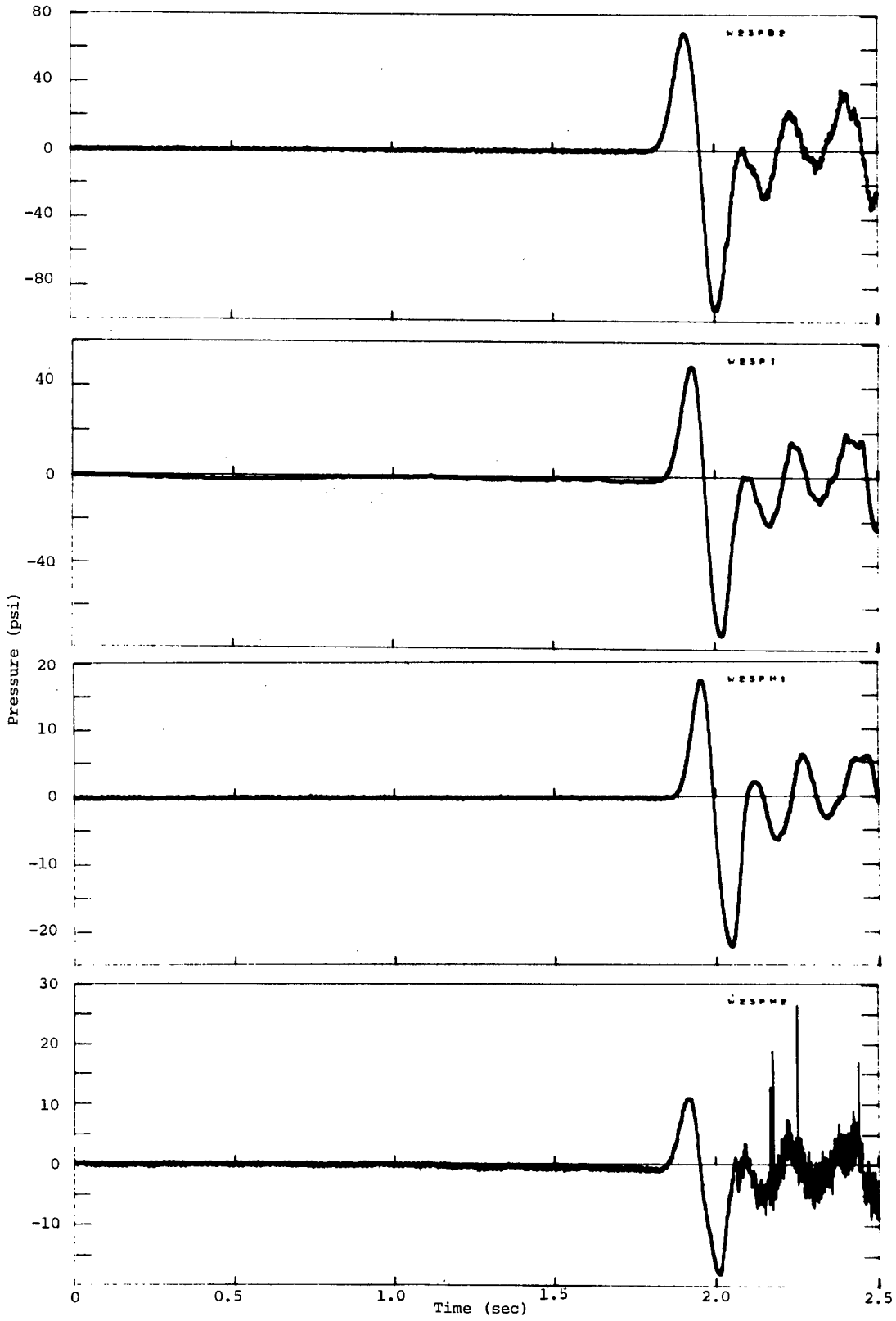

Figure 3.11 Pressures at station W23

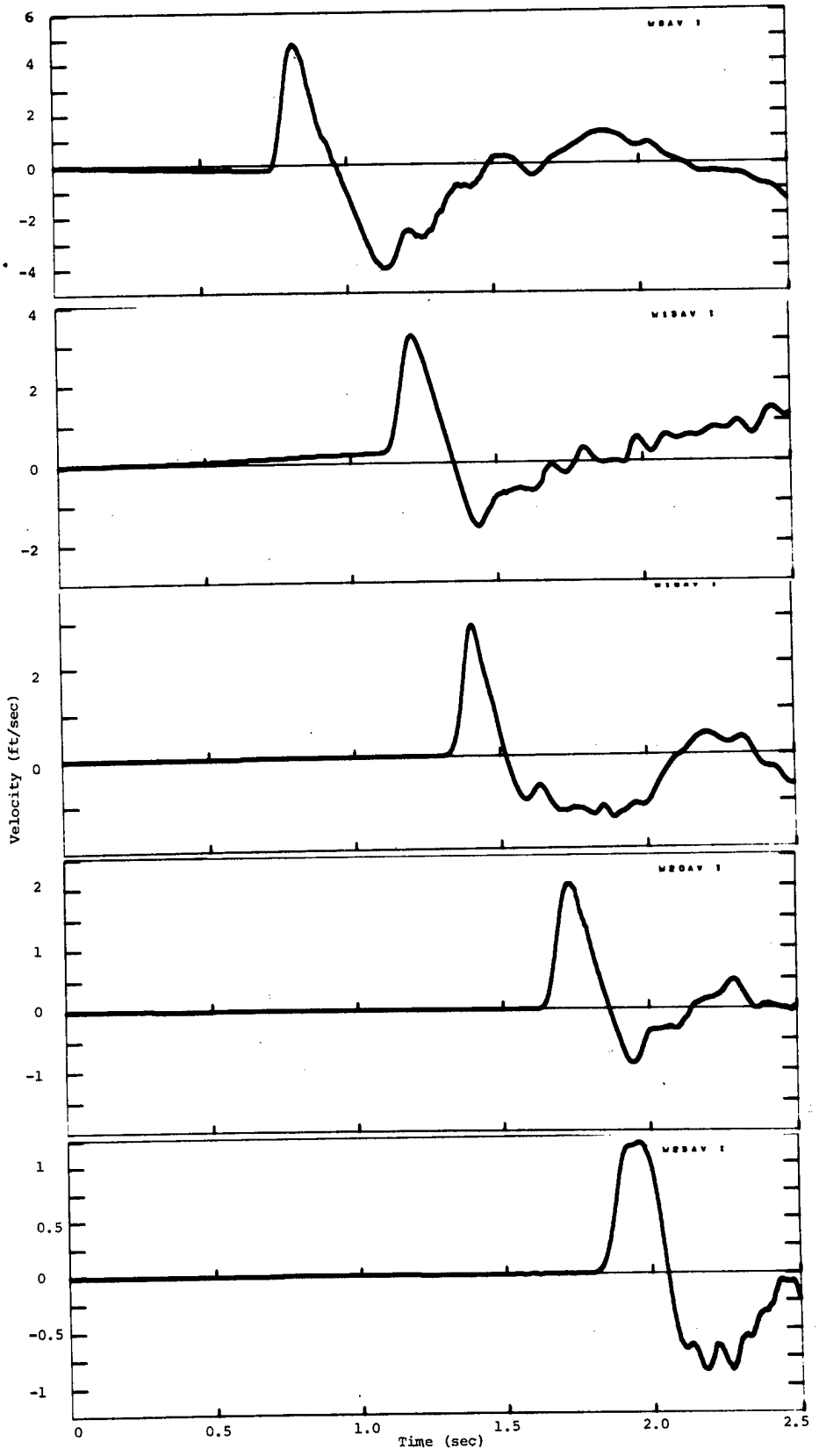

Figure 3.12 Integrated vertical accelerations

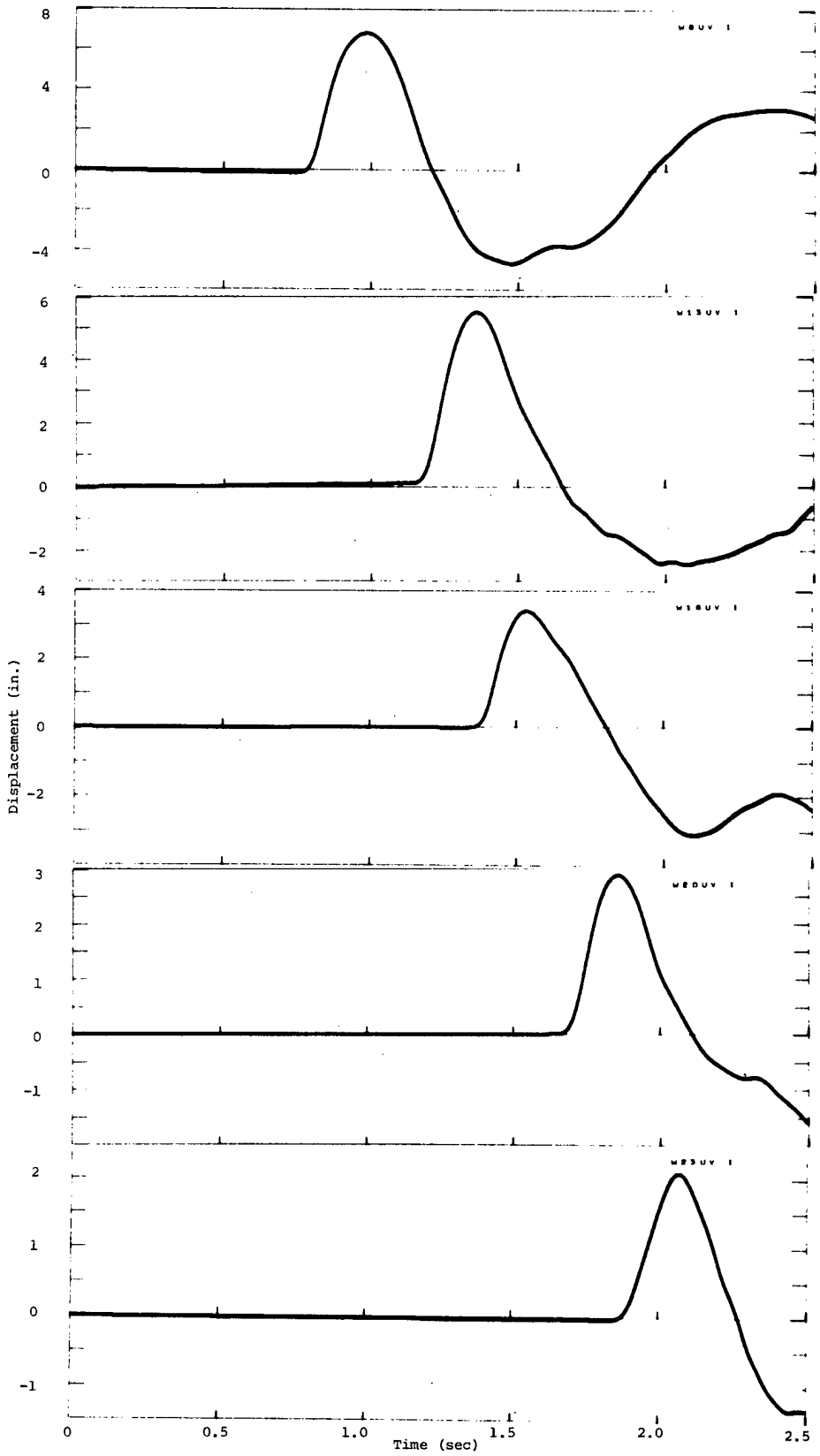

Figure 3.13 Integrated vertical velocities

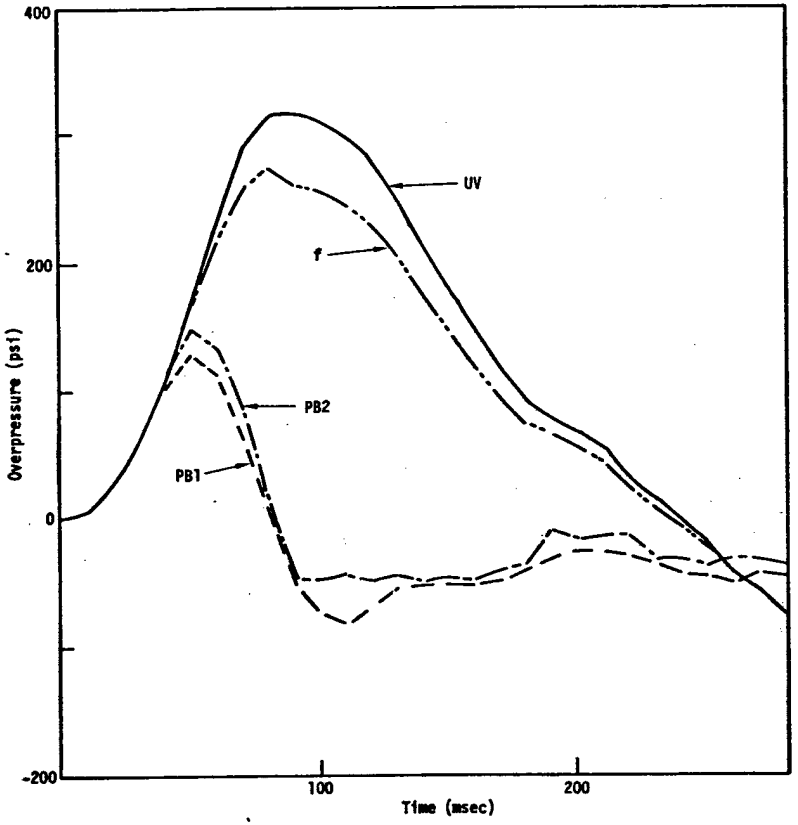

Figure 3.14 Comparison of waveforms, station W8: PB1, PB2, UV, f

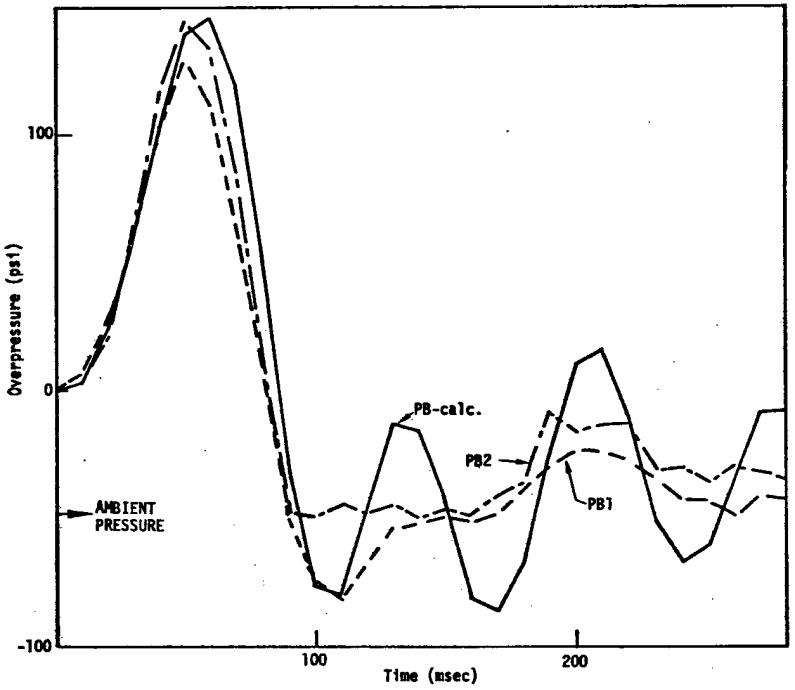

Figure 3.15 Comparison of measured and calculated waveforms, station W8 bottom pressures

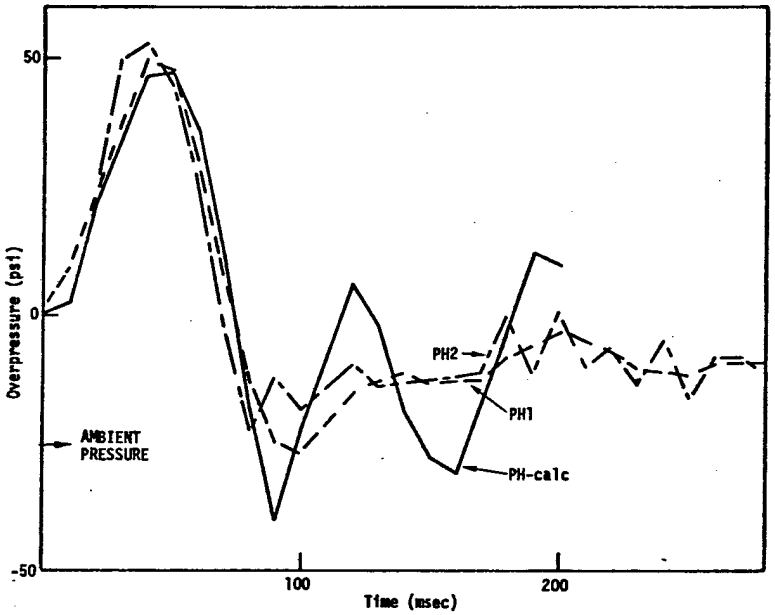

Figure 3.16 Comparison of measured and calculated pressures, station W8 half-way-up pressures

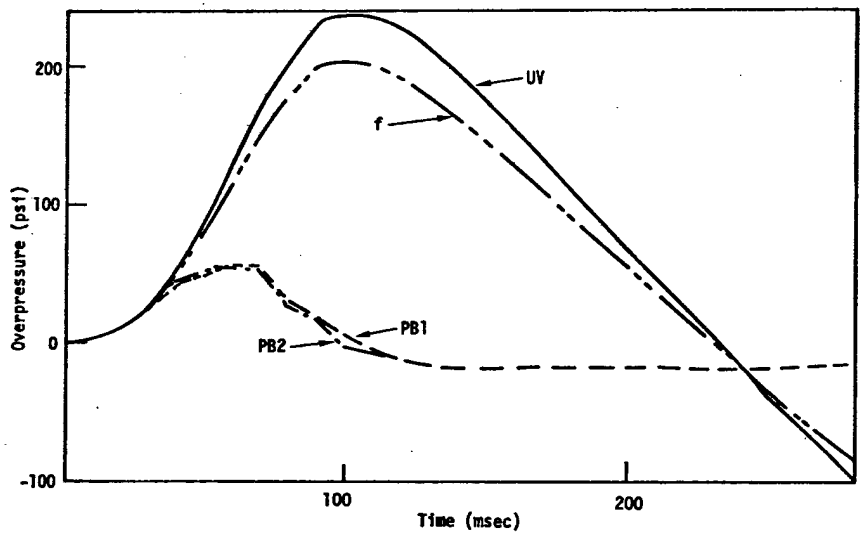

Figure 3.17 Comparison of waveforms, station W13: PB1, PB2, UV, f

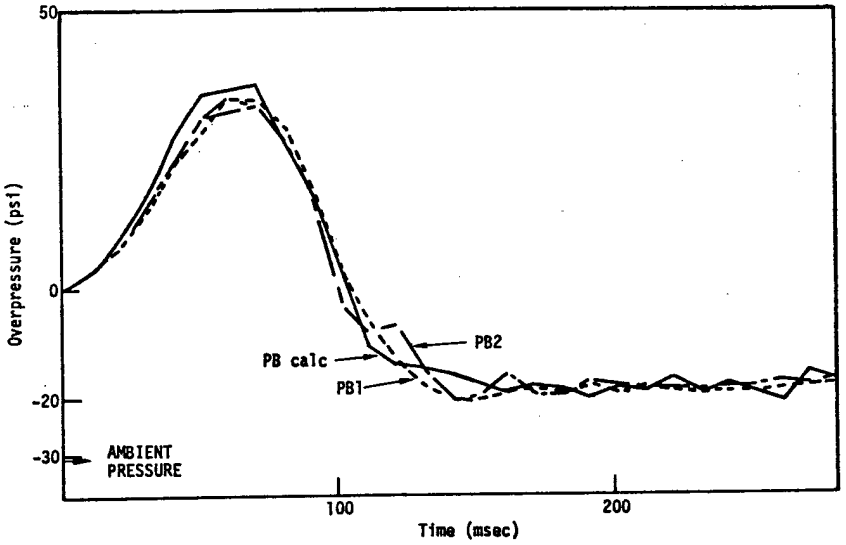

Figure 3.18 Comparison of measured and calculated waveforms, station W13 bottom pressures

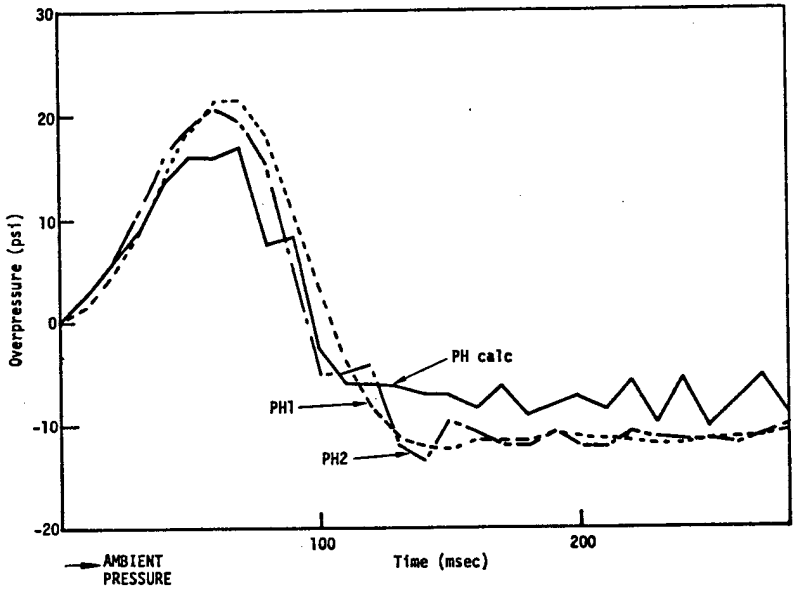

Figure 3.19 Comparison of measured and calculated waveforms, station W13 half-way-up pressures

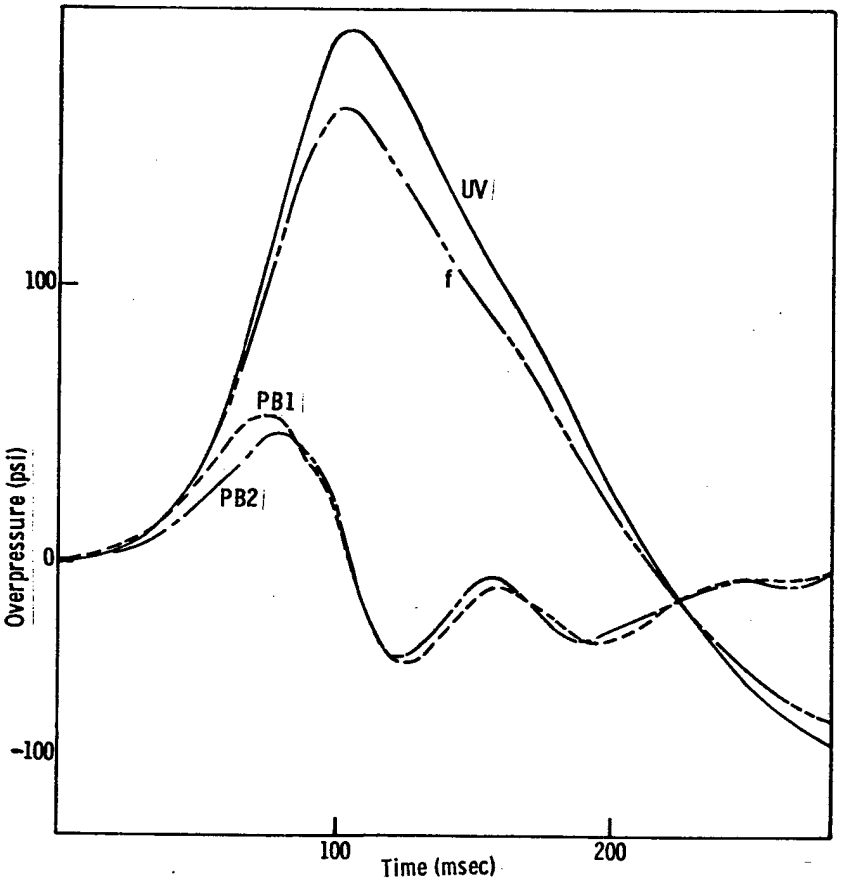

Figure 3.20 Comparison of waveforms, station W16: PB1, PB2, UV, f

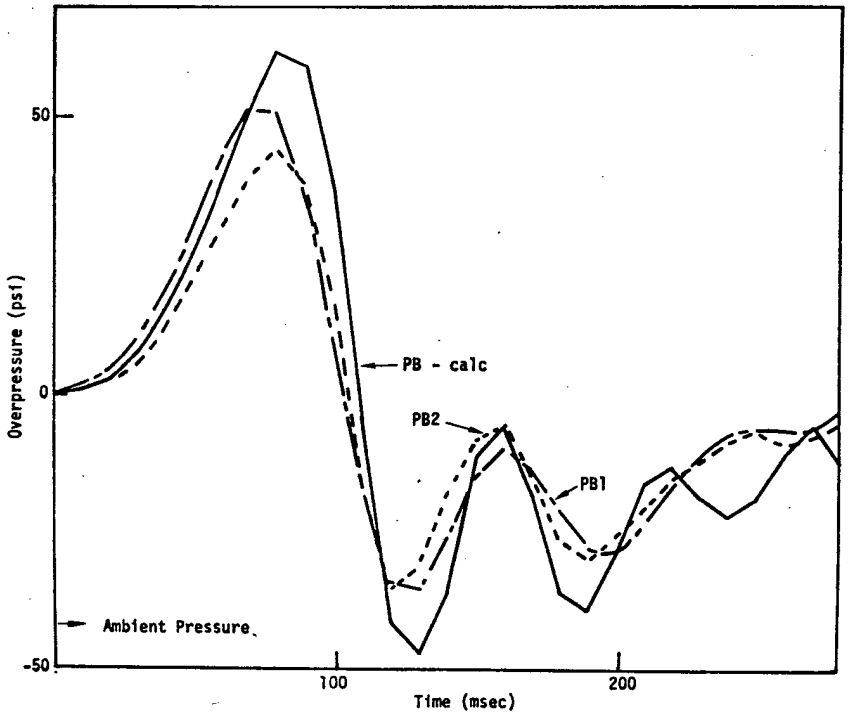

Figure 3.21 Comparison of measured and calculated waveforms, station W16 bottom pressures

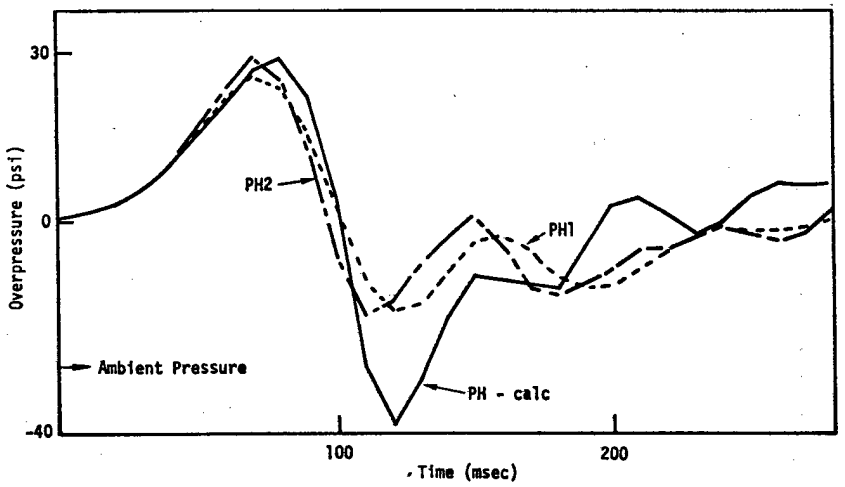

Figure 3.22 Comparison of measured and calculated waveforms, station W16 half-way-up pressures

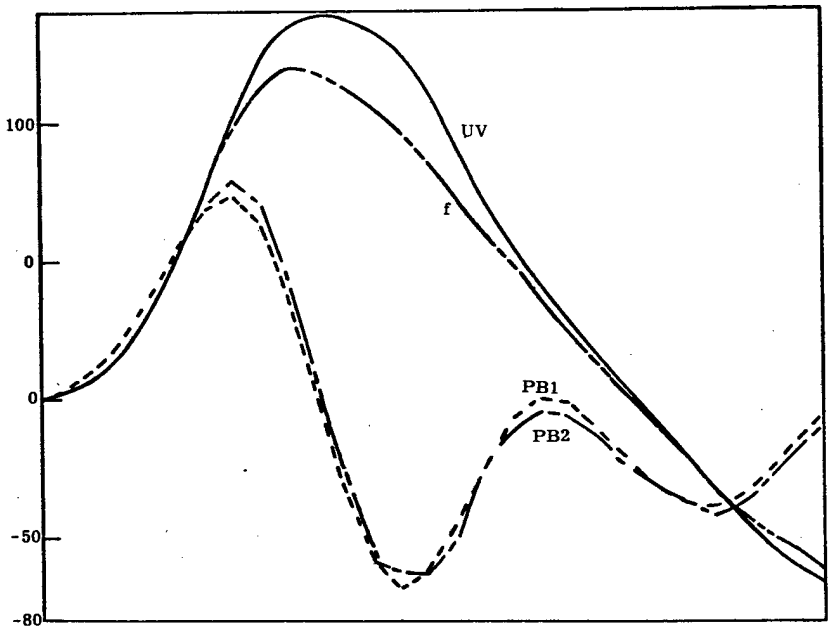

Figure 3.23 Comparison of waveforms, station W20: PB1, PB2, UV, f

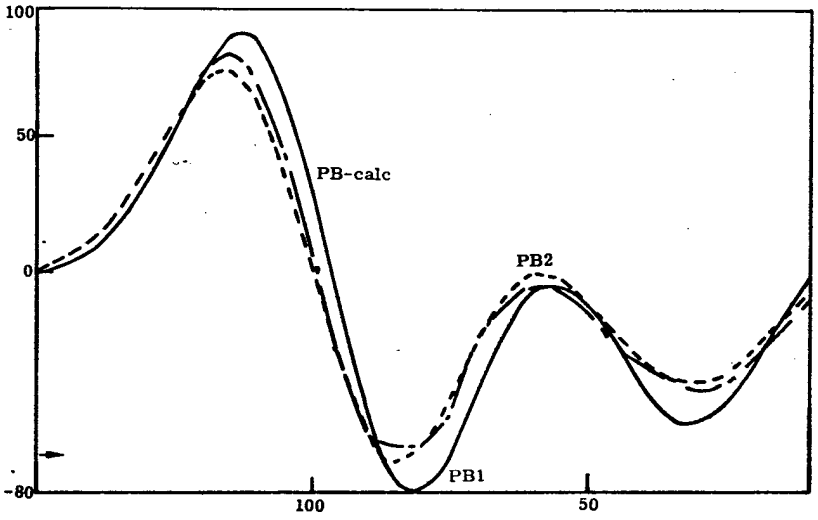

Figure 3.24 Comparison of measured and calculated waveforms, station W20 bottom pressures

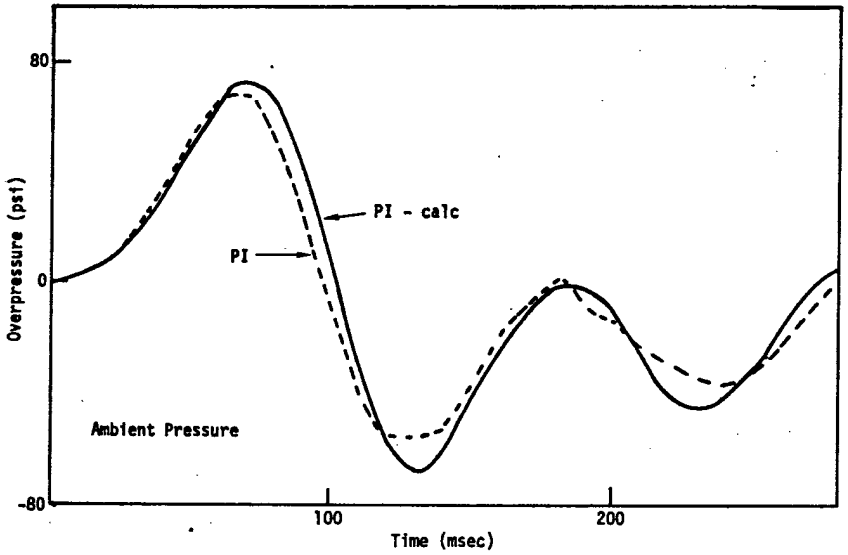

Figure 3.25 Comparison of measured and calculated waveforms, station W20 intermediate-depth pressures

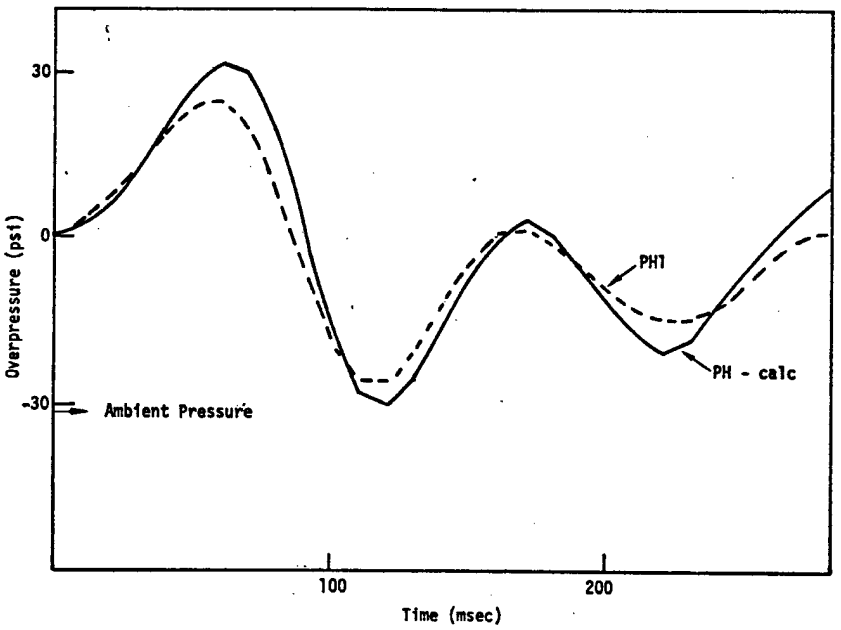

Figure 3.26 Comparison of measured and calculated waveforms, station W20 half-way-up pressures

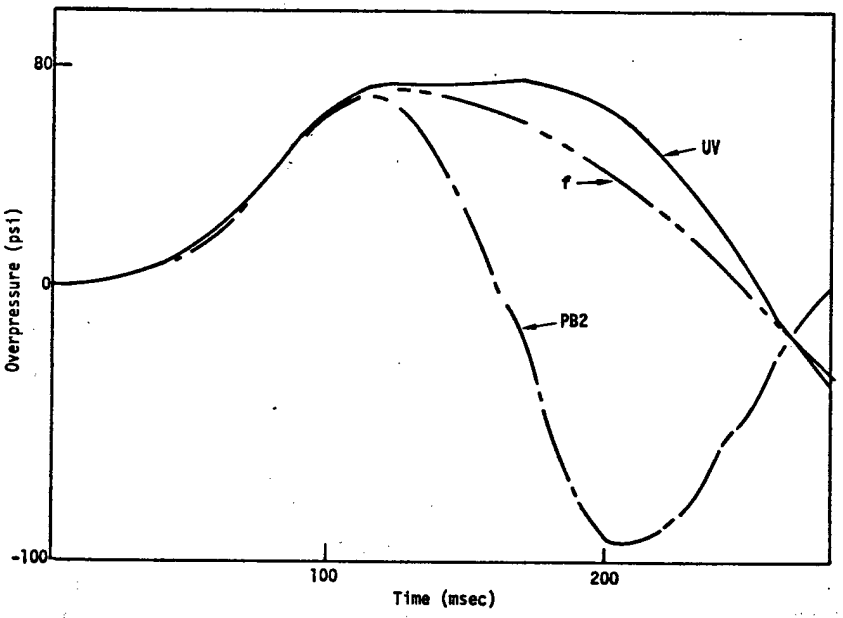

Figure 3.27 Comparison of waveforms, station W23 PB2, UV, f

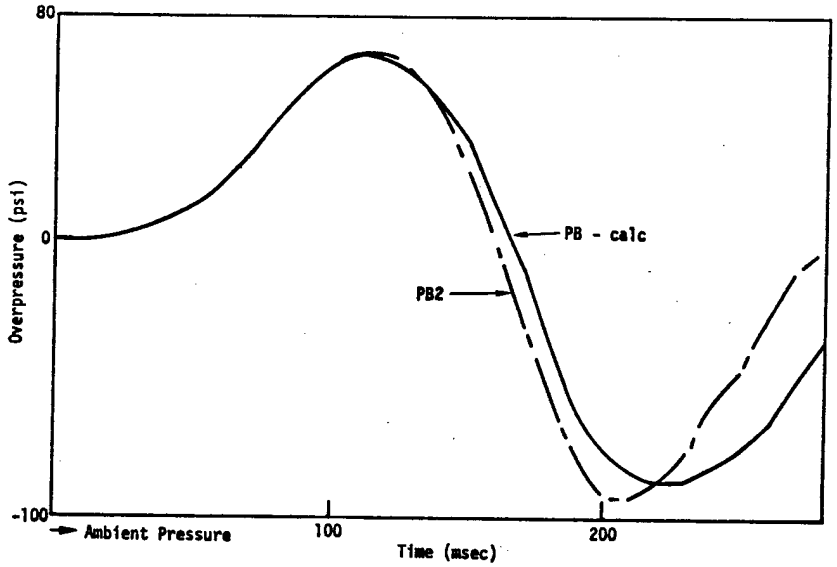

Figure 3.28 Comparison of measured and calculated waveforms, station W23 bottom pressures

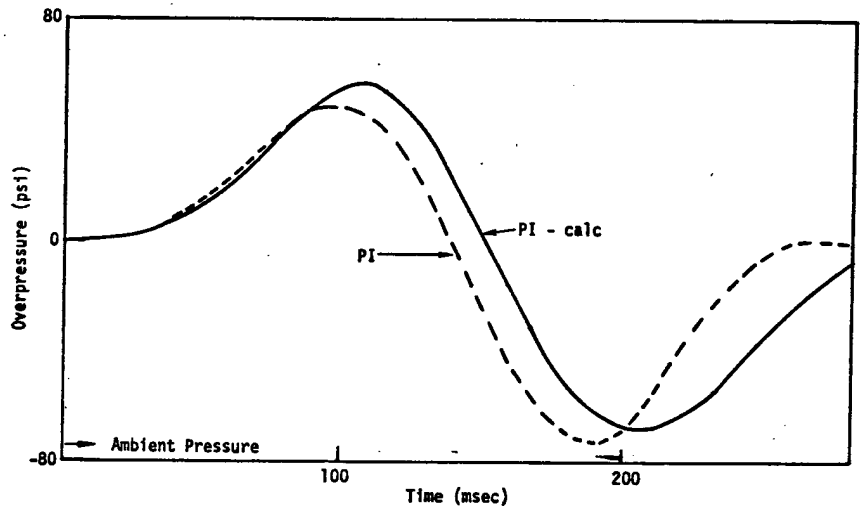

Figure 3.29 Comparison of measured and calculated waveforms, station W23 intermediate-depth pressures

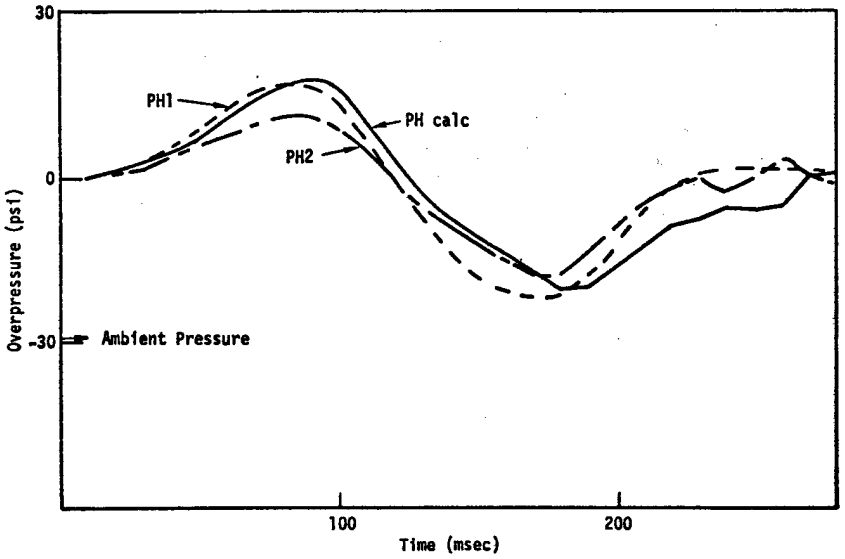

Figure 3.30 Comparison of measured and calculated waveforms, station W23 half-way-up pressures

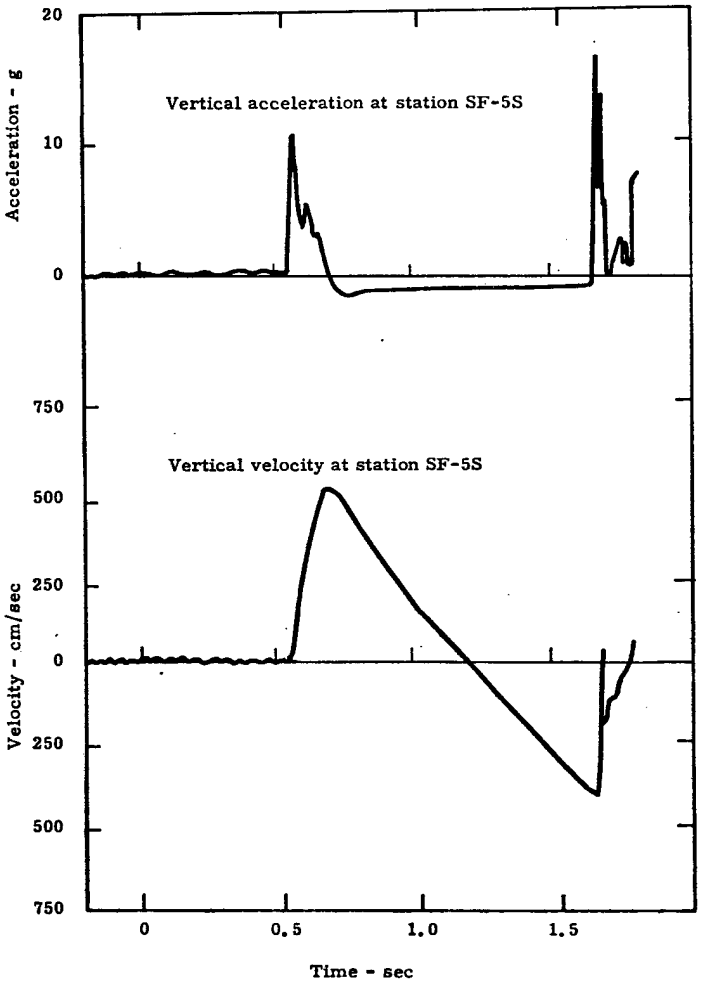

Figure 3.31 Typical Cannikin surface motions: vertical acceleration and vertical velocity at station SF5S

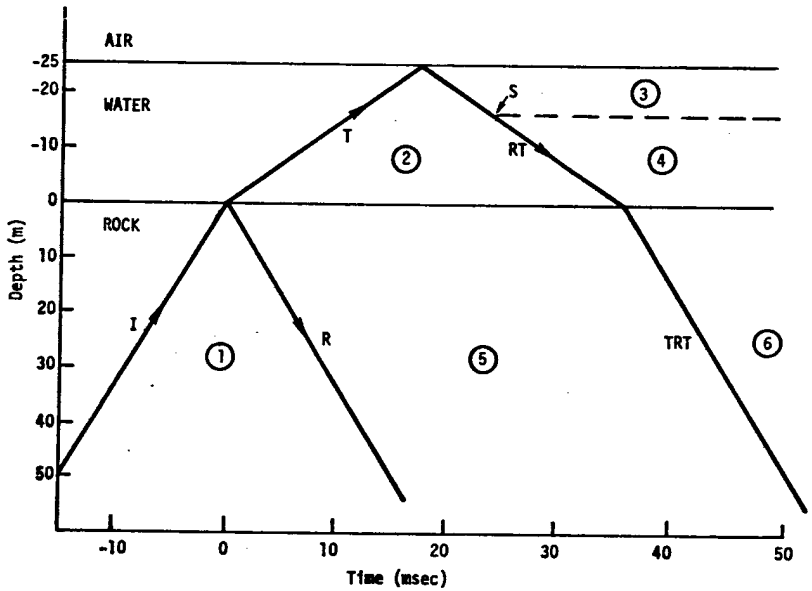

Figure 3.32 Space-time diagram of the spall phenomenon

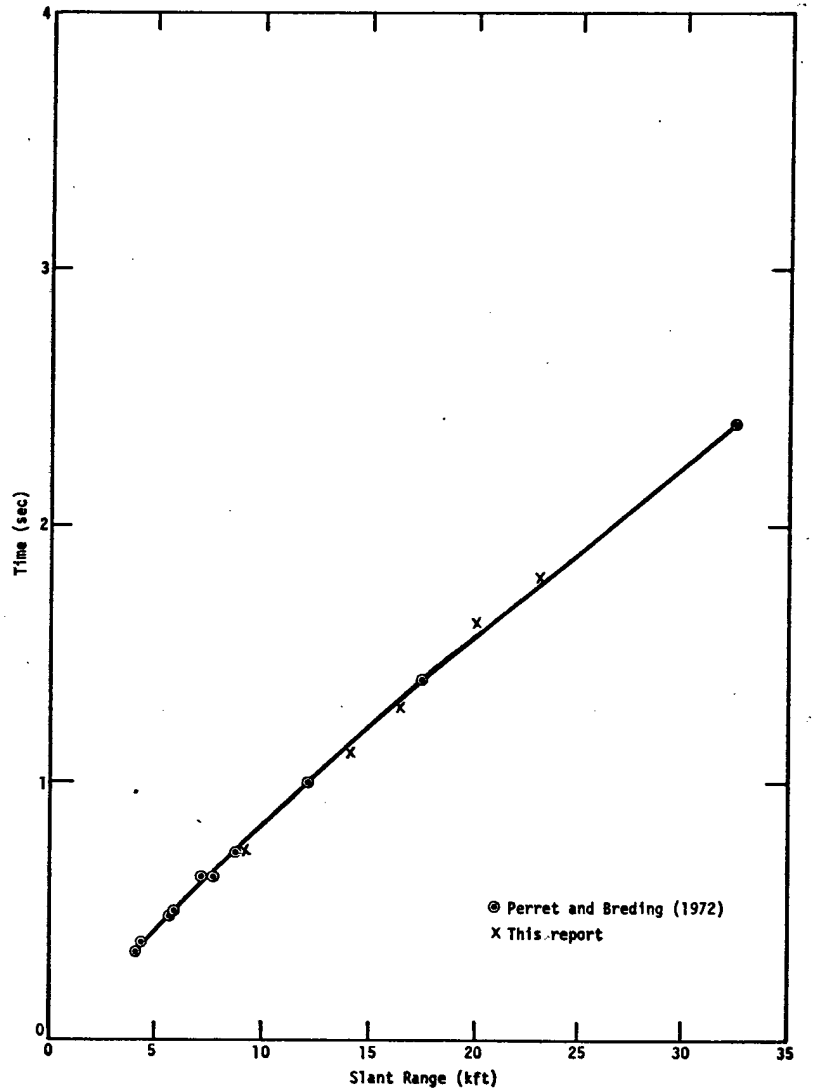

Figure 3.33 Milrow times of arrival versus slant range

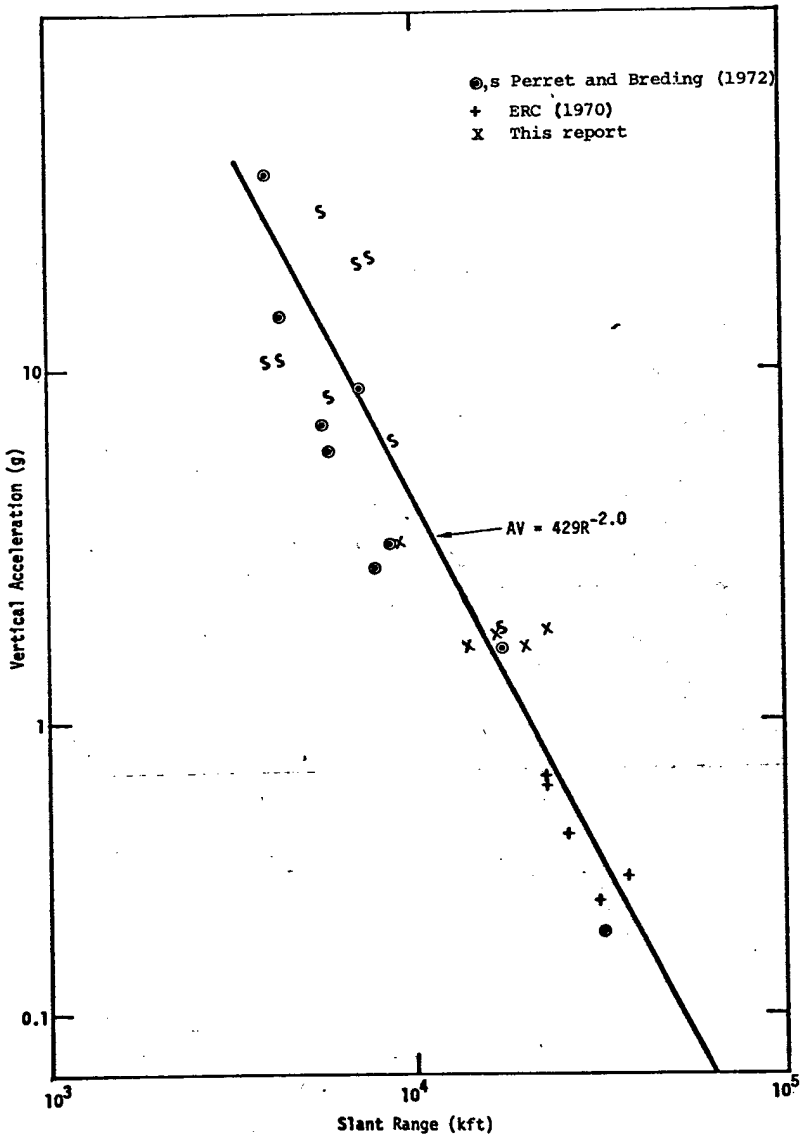

Figure 3.34 Milrow vertical accelerations versus slant range

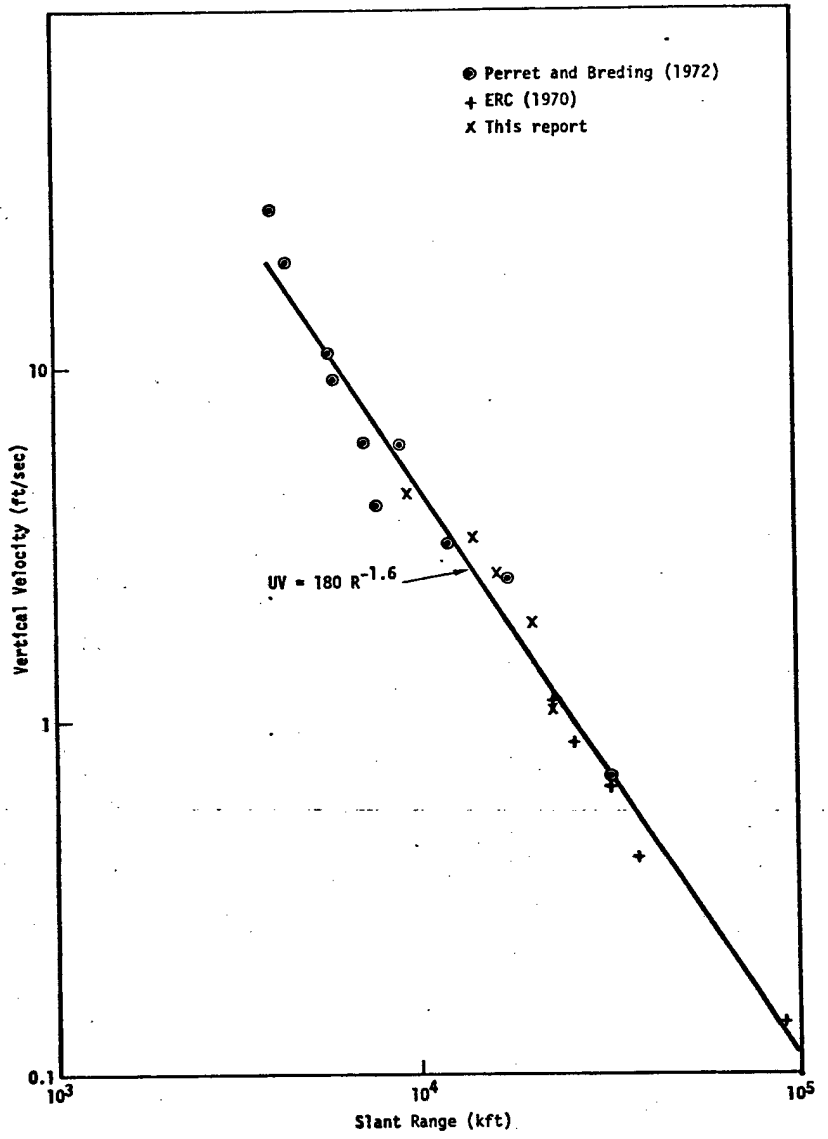

Figure 3.35 Milrow vertical velocities versus slant range

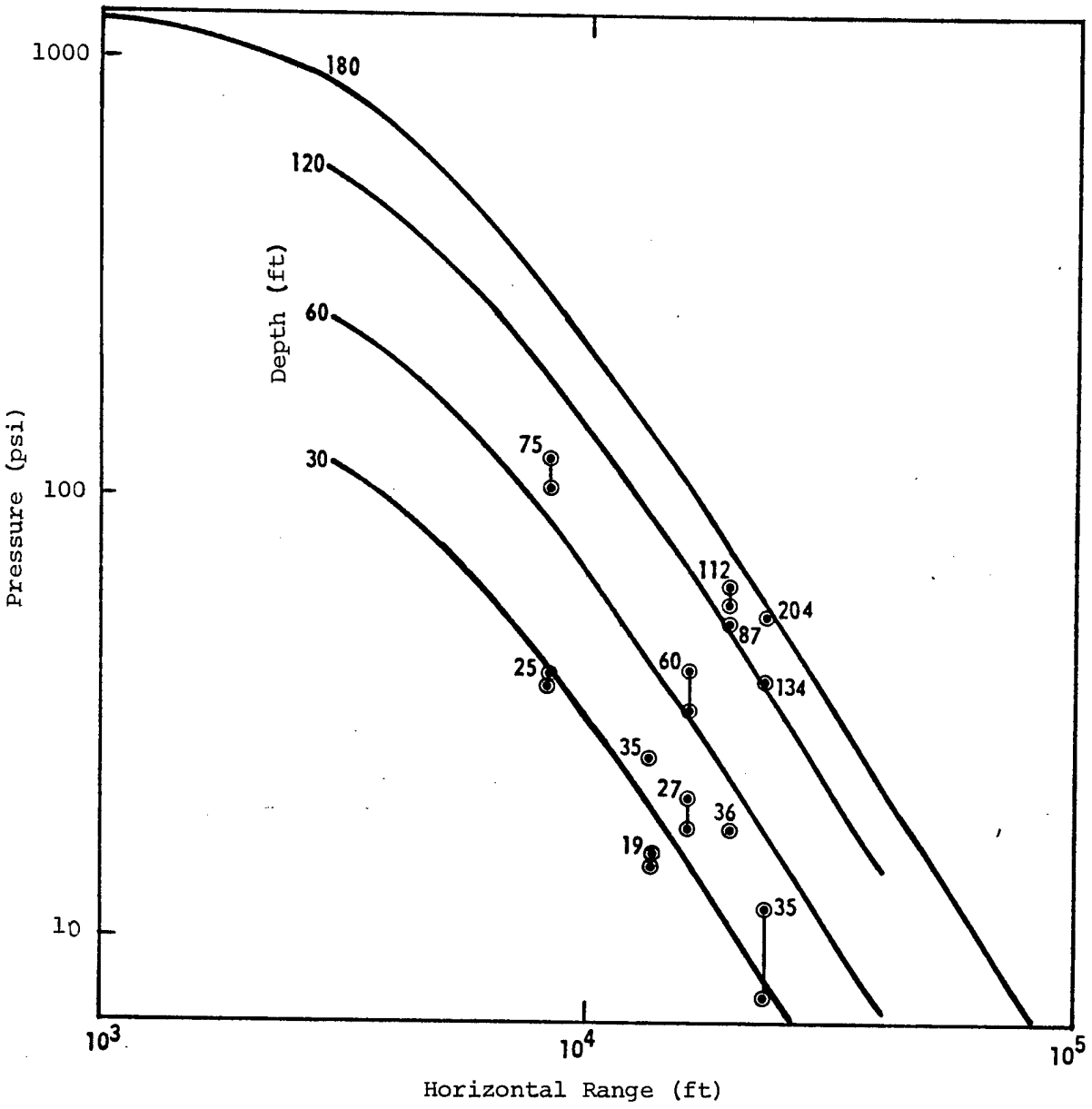

Figure 3.36 Milrow water pressures versus horizontal range and depth

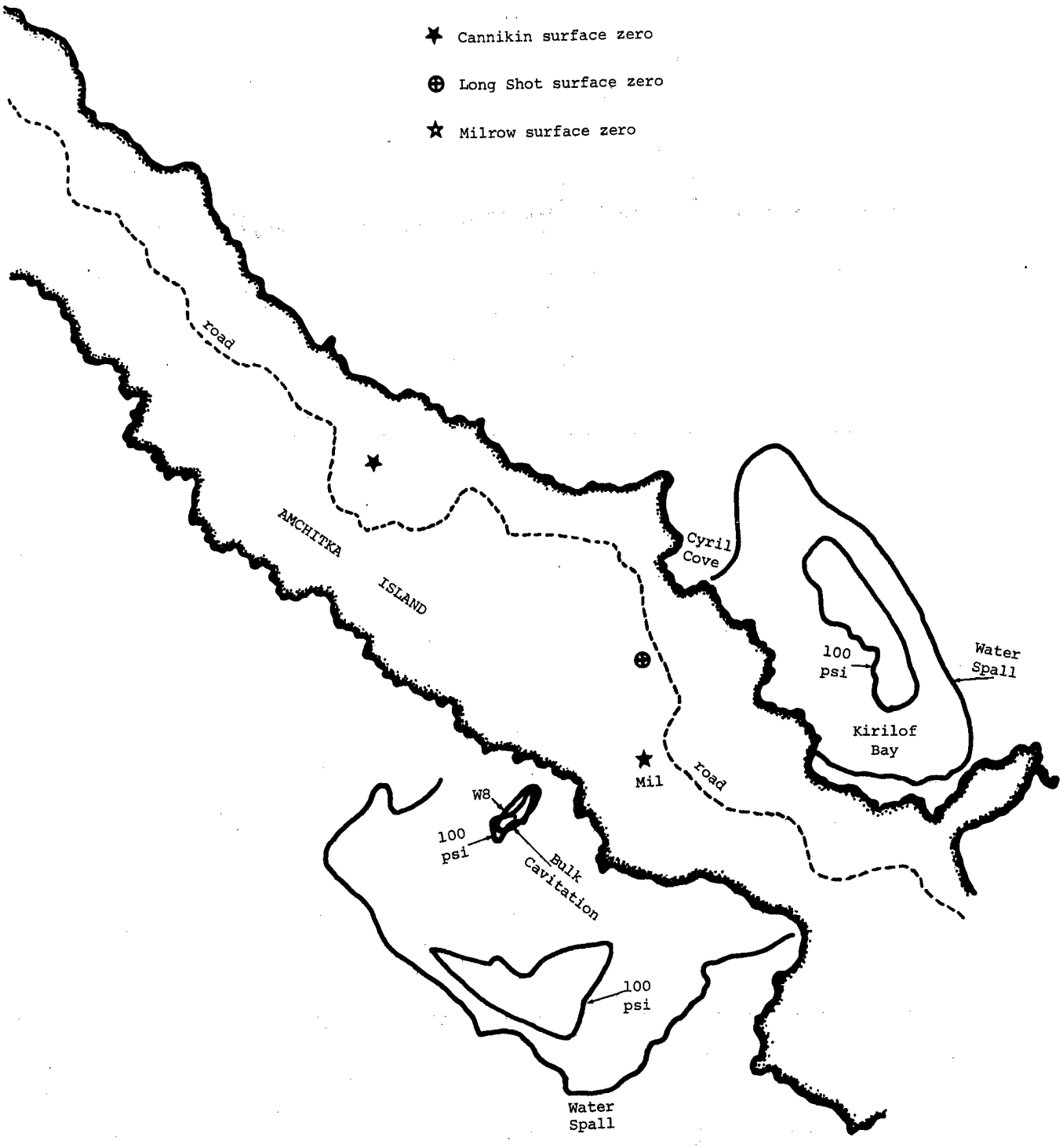

Figure 3.37 Map showing contours of Milrow bottom pressures and limit of water spall

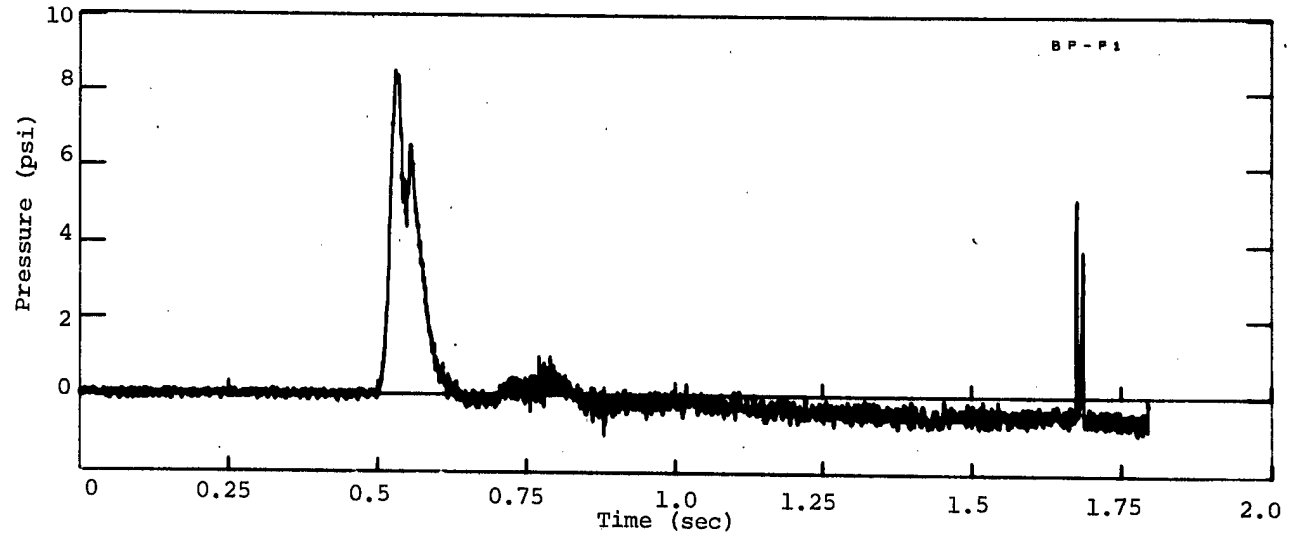

Figure 4.1 Pressure in lake BP; horizontal range 0.72 km

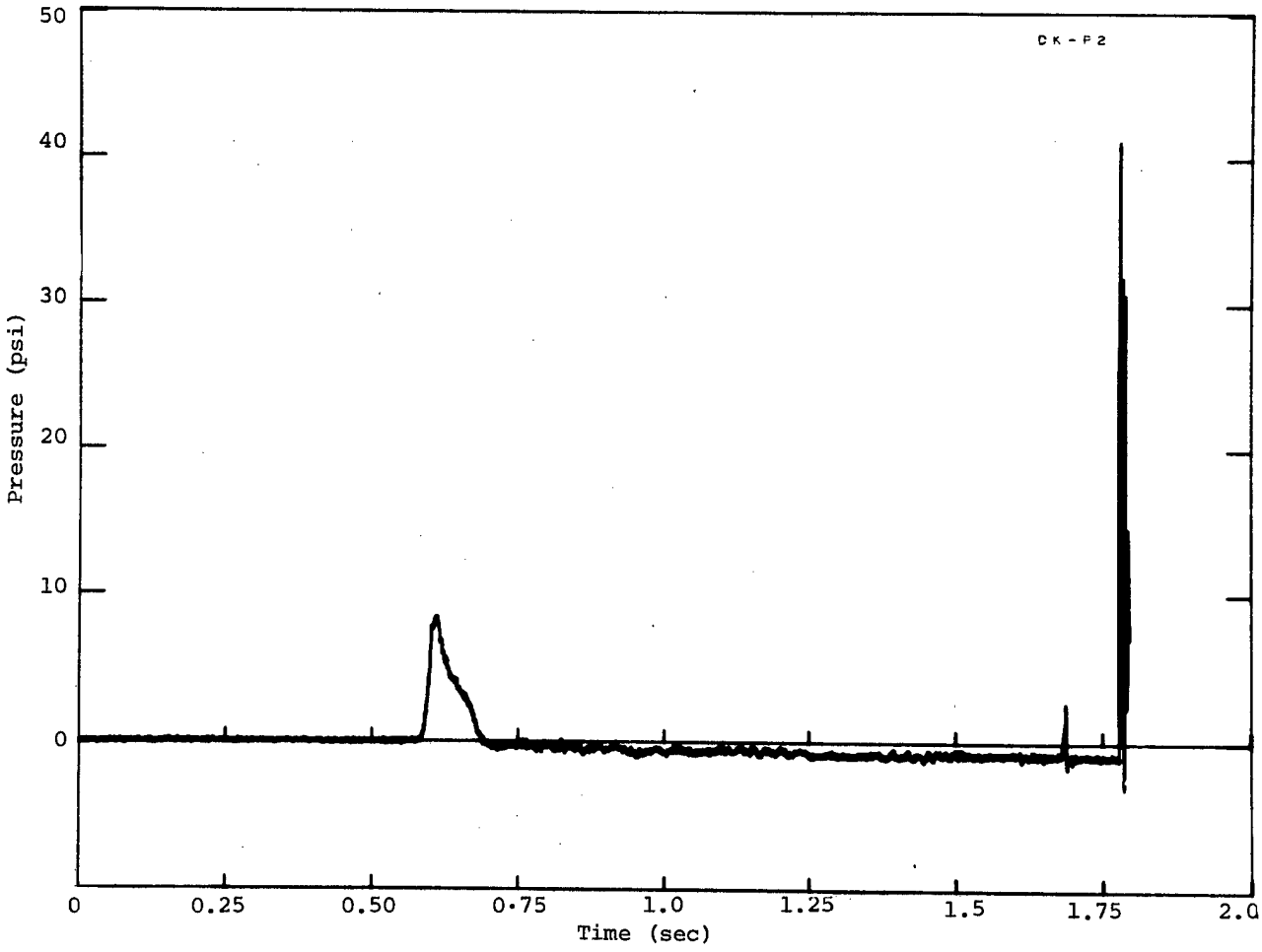

Figure 4.2 Pressure in lake DK, station DK-2; horizontal range 1.29 km

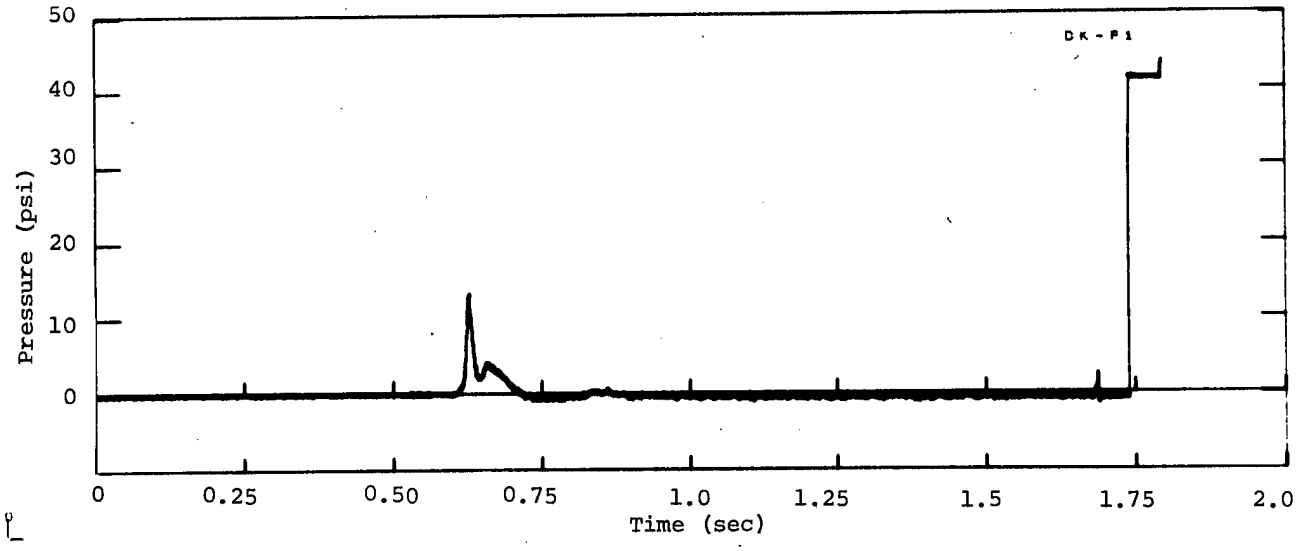

Figure 4.3 Pressure in lake DK, station DK-1; horizontal range 1.41 km

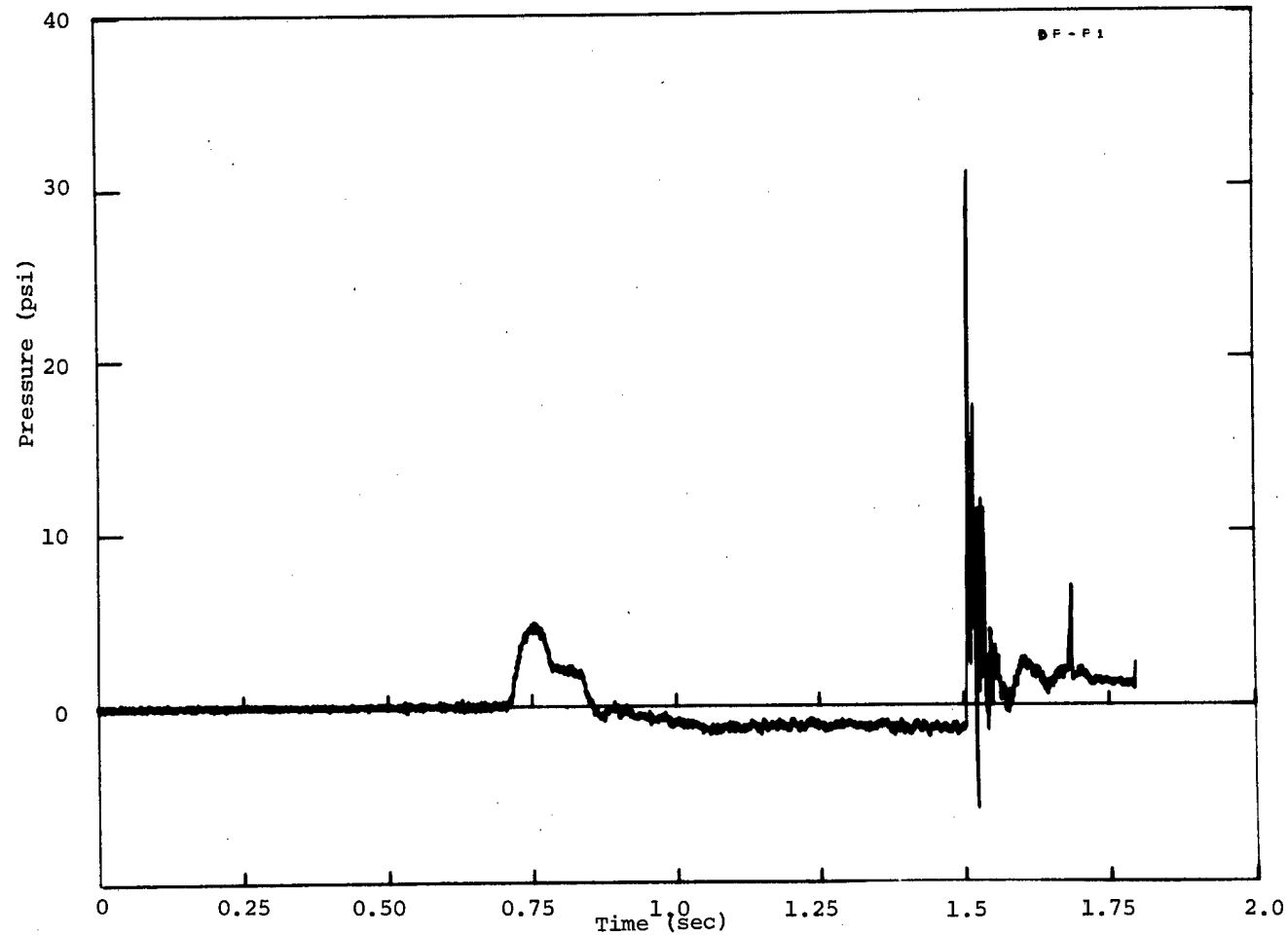

Figure 4.4 Pressure in lake DP, station DP-1; horizontal range 2.10 km

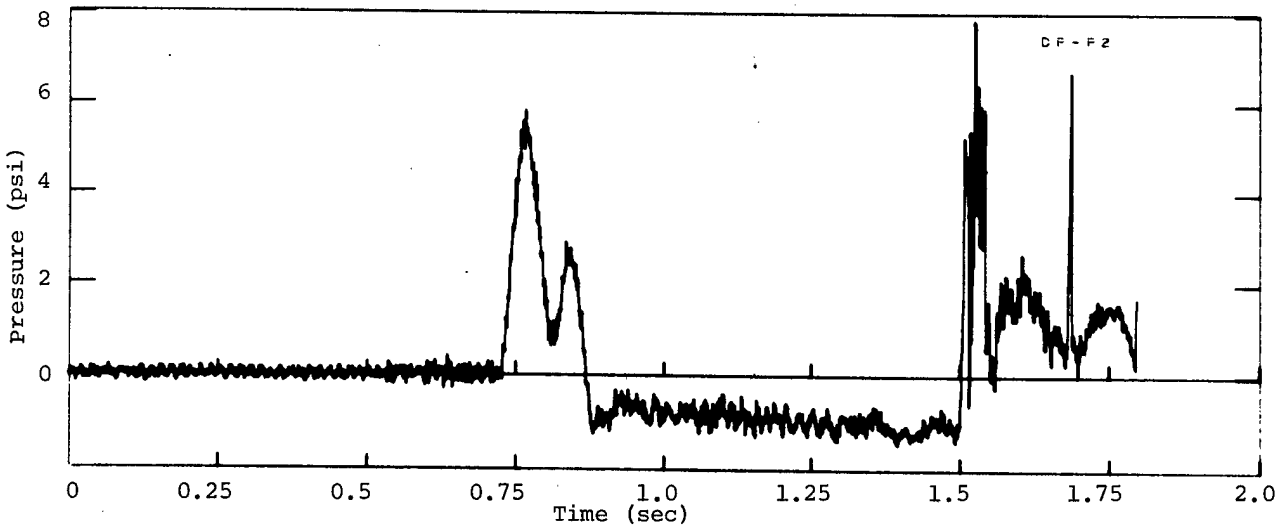

Figure 4.5 Pressure in lake DP, station DP-2; horizontal range 2.15 km

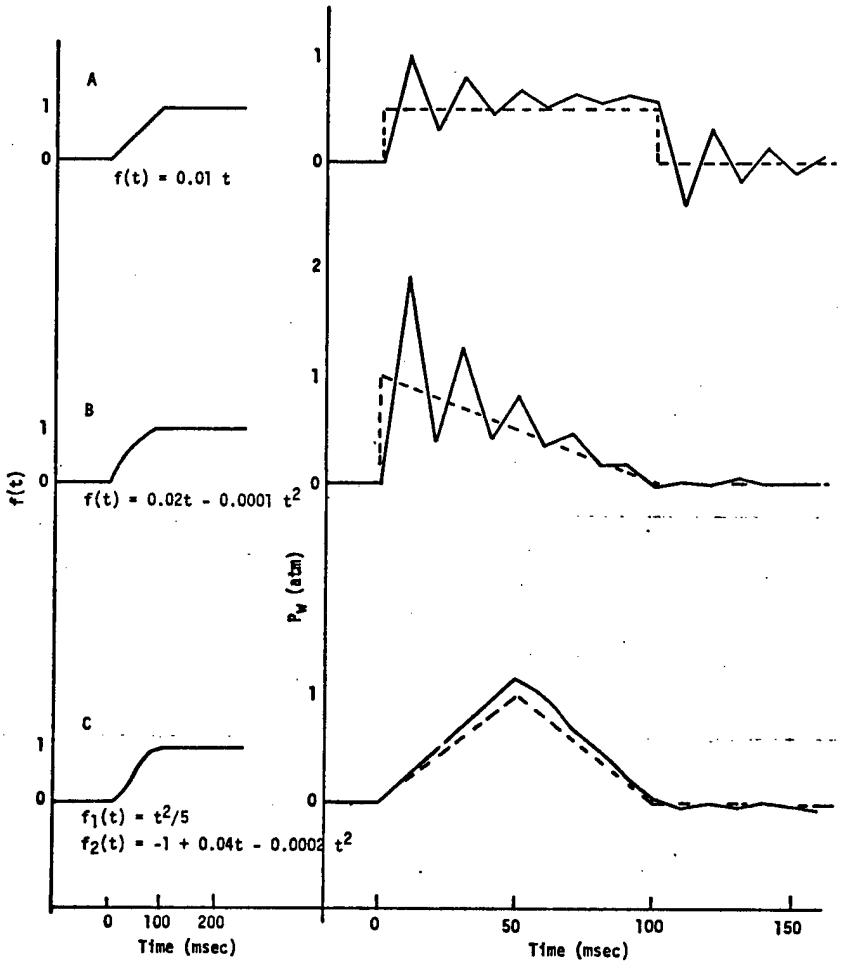

Figure 4.6 Three comparisons of the application of the shallow water with the reverberation theory of water pressure

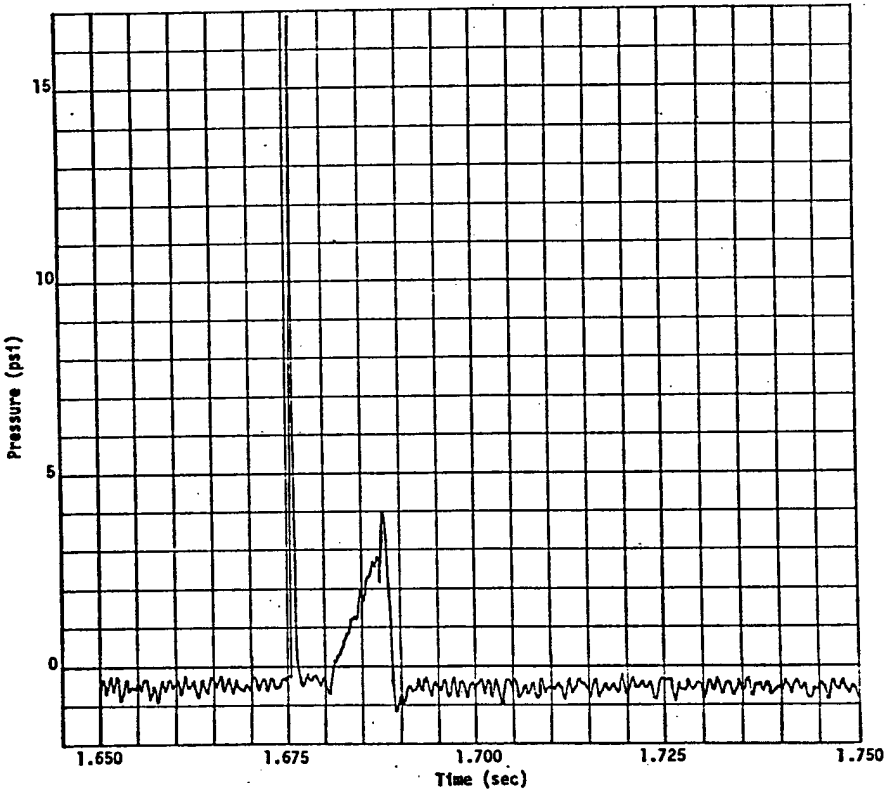

Figure 4.7 Second pressure pulse, station BP

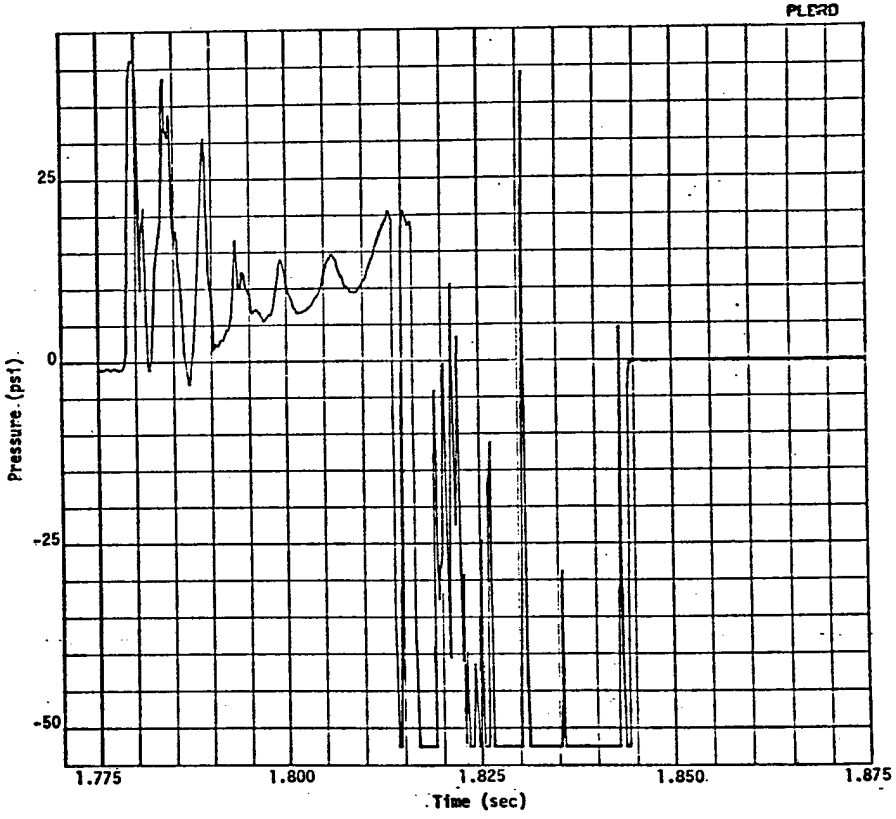

Figure 4.8 Second pressure pulse, station DK-2

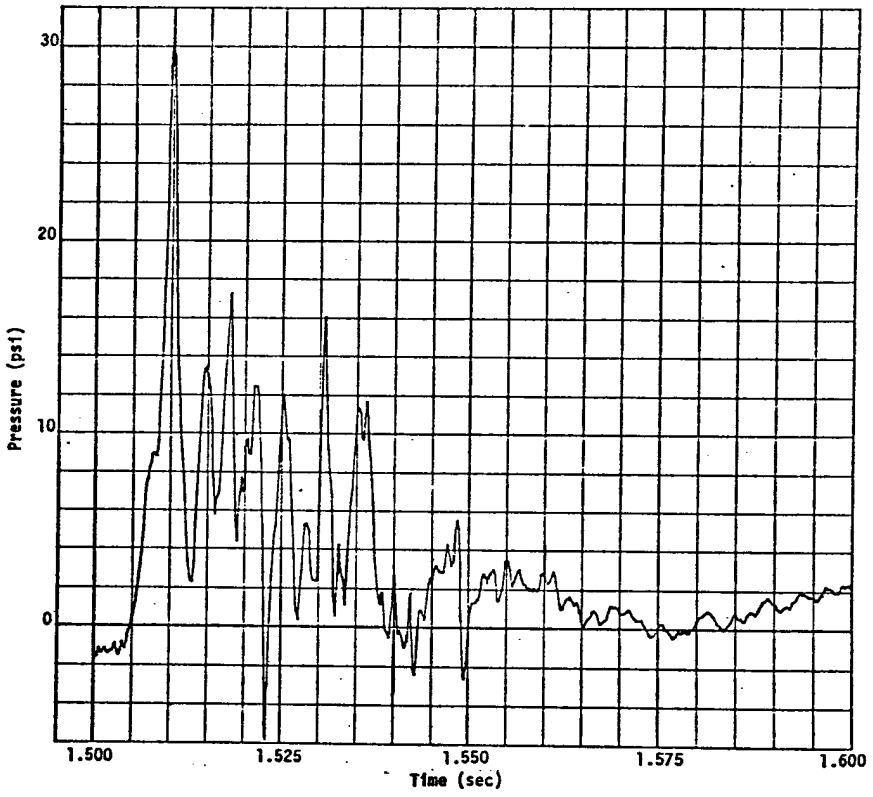

Figure 4.9 Second pressure pulse, station DP-1

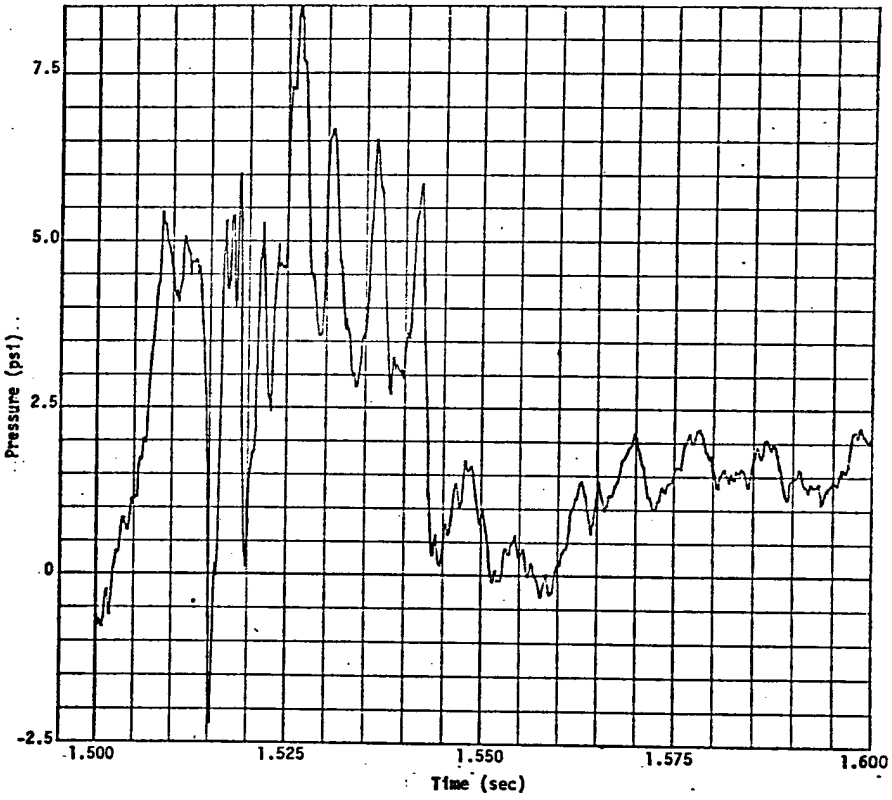

Figure 4.10 Second pressure pulse, station DP-2

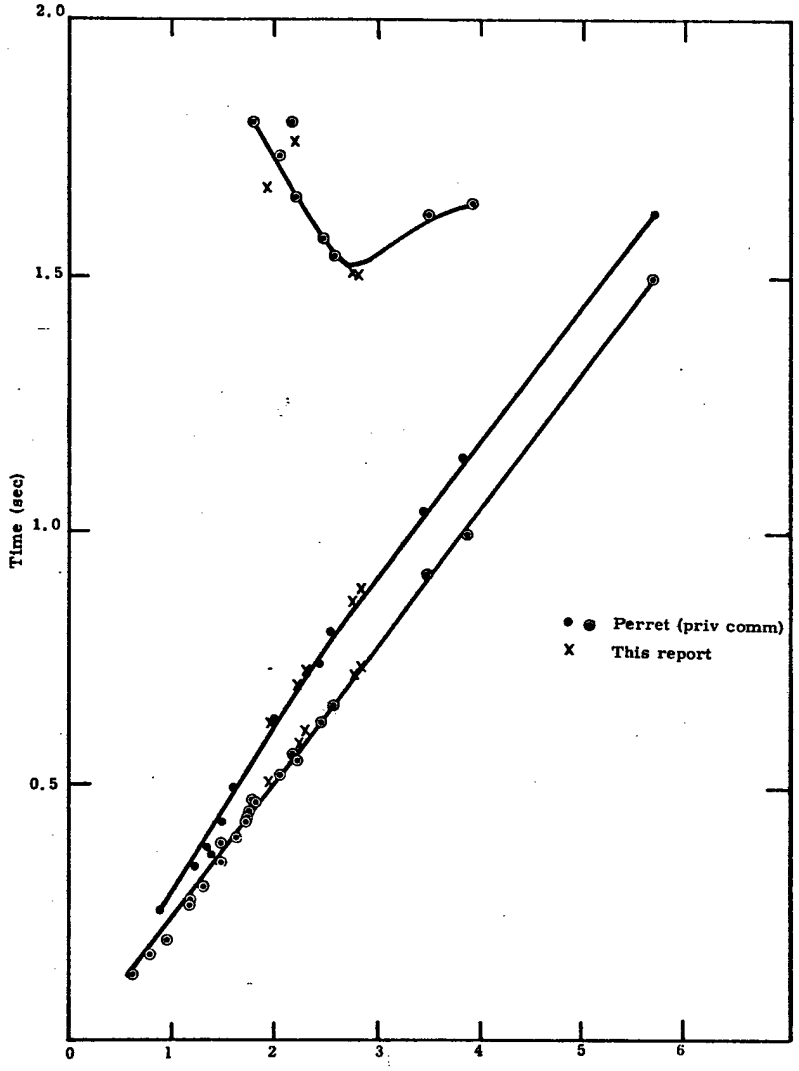

Figure 4.11 Comparison of time scales of vertical accelerations with those of shallow water pressures

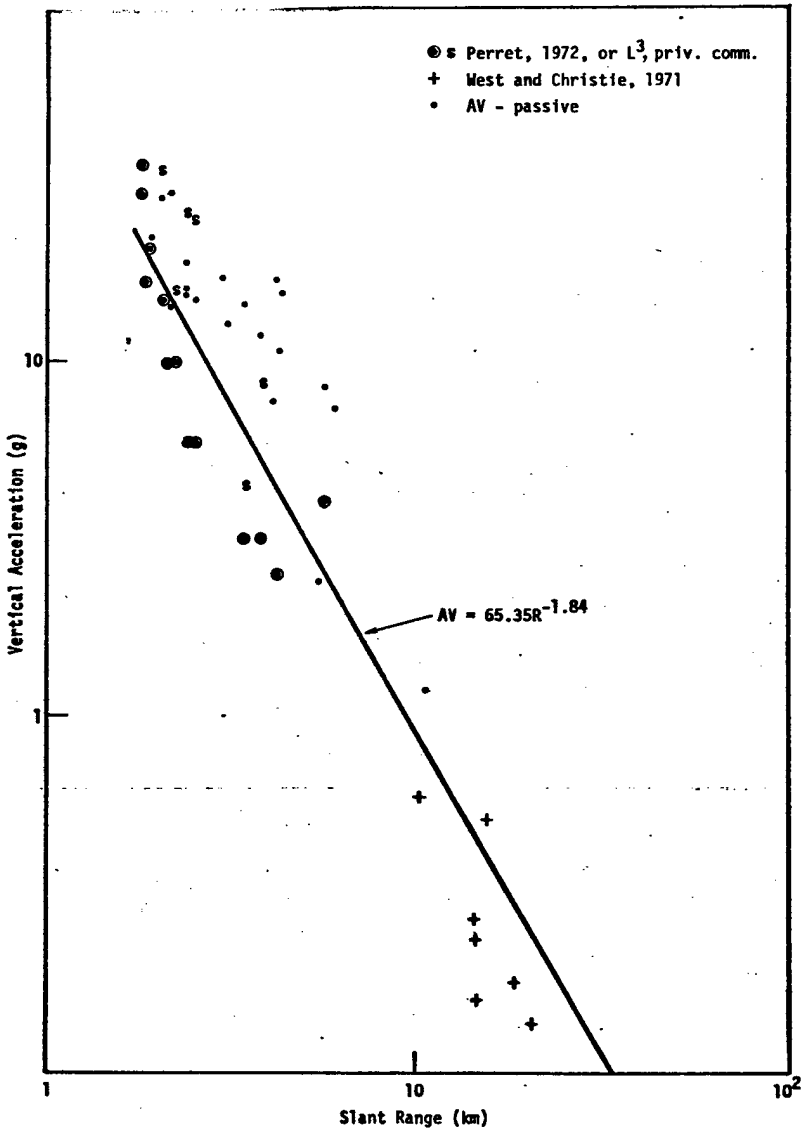

Figure 4.12 Cannikin vertical accelerations versus slant range

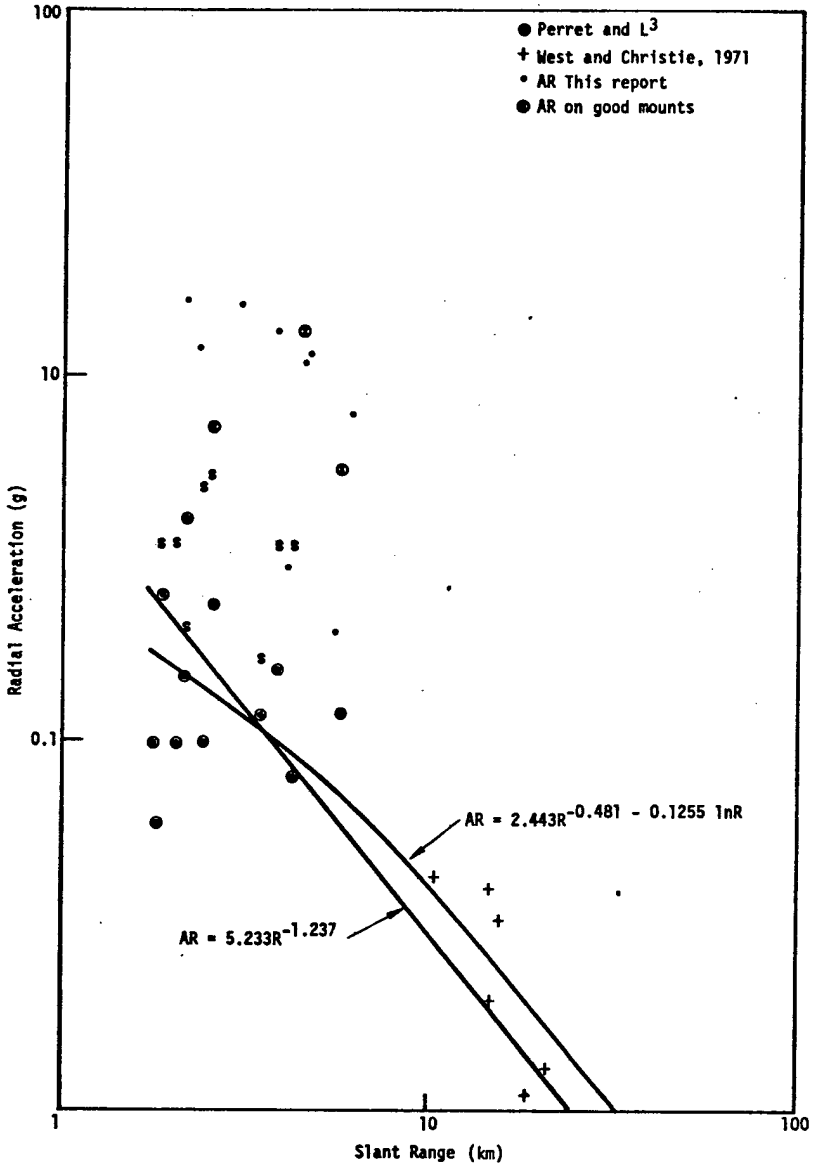

Figure 4.13 Cannikin radial accelerations versus slant range

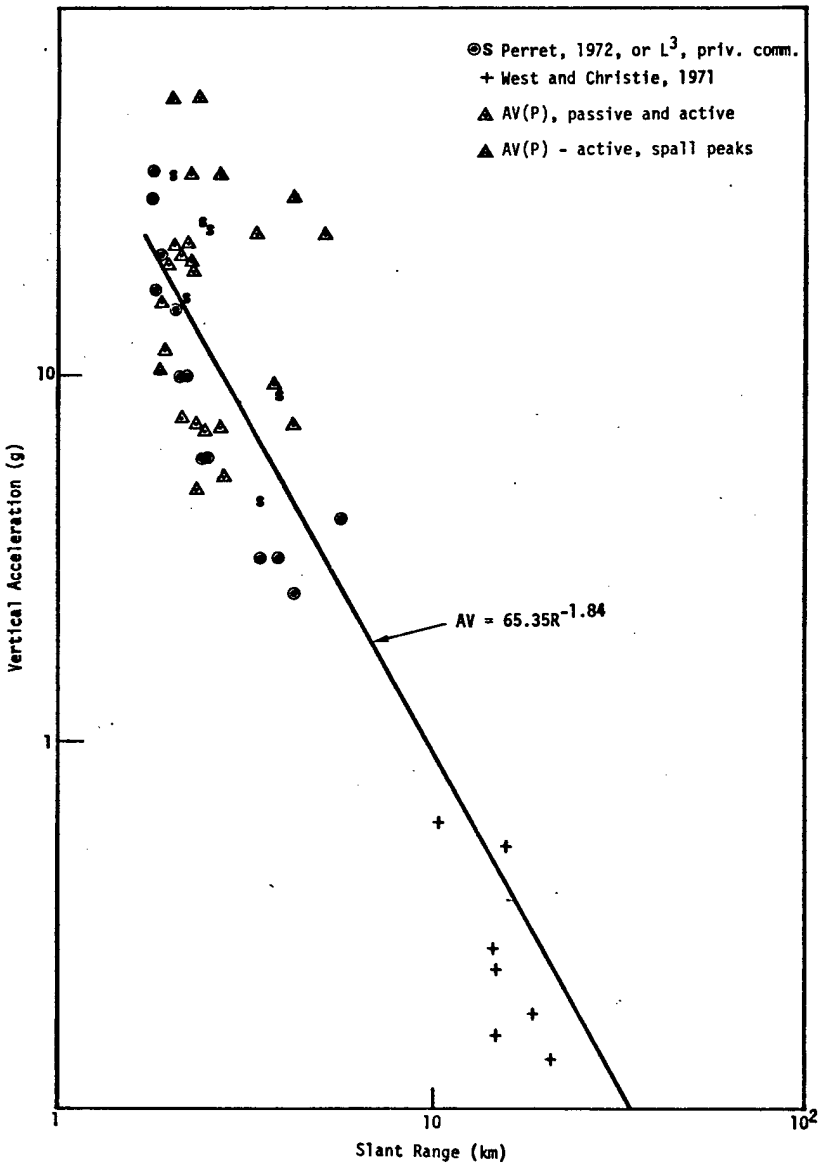

Figure 4.14 Cannikin vertical accelerations--comparison with accelerations inferred from pressure measurements

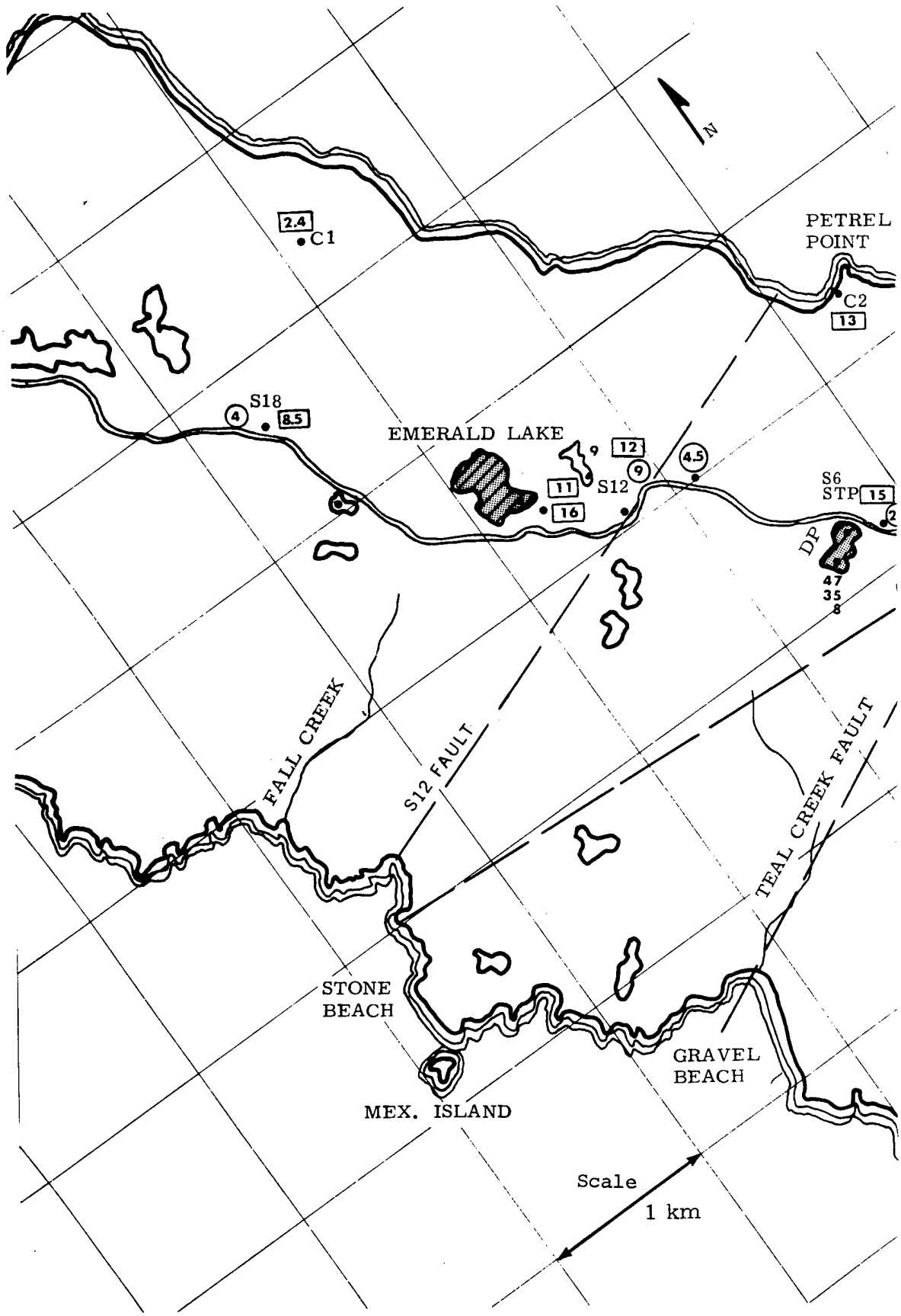

Figure 4.15 Map relating measur

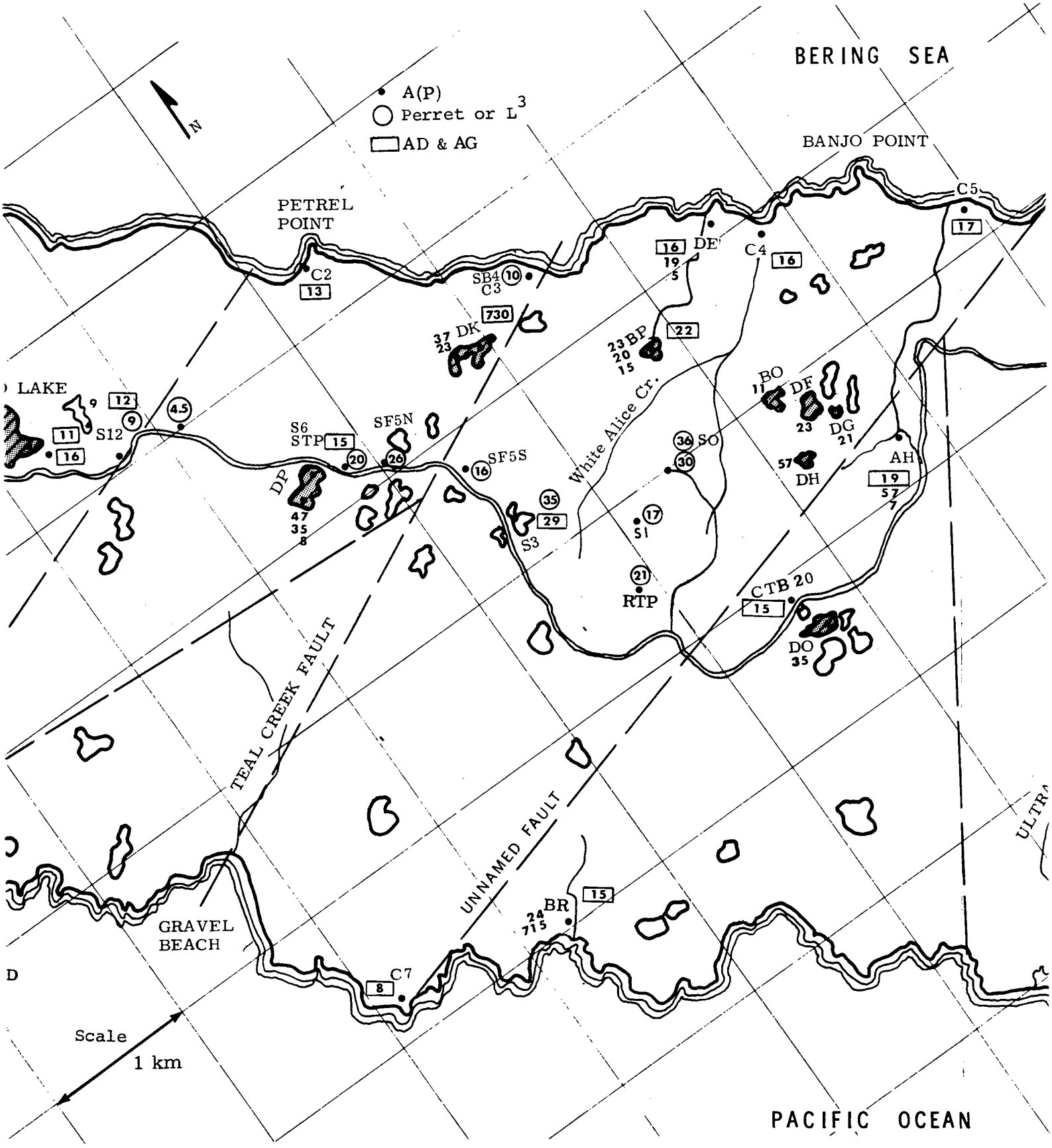

Figure 4.15 Map relating measured and inferred accelerations to location and to faults

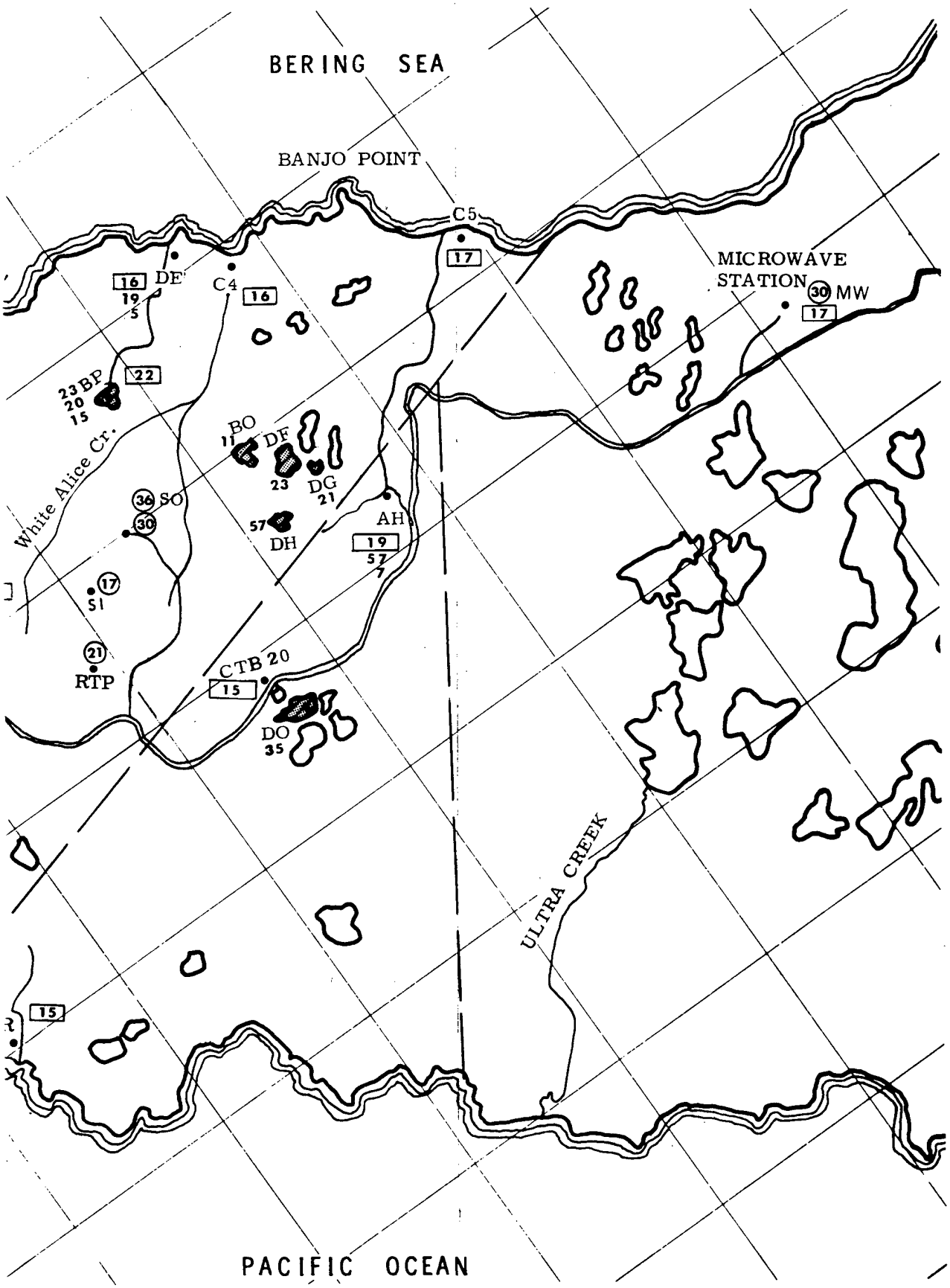

elerations to location and to faults

(3)

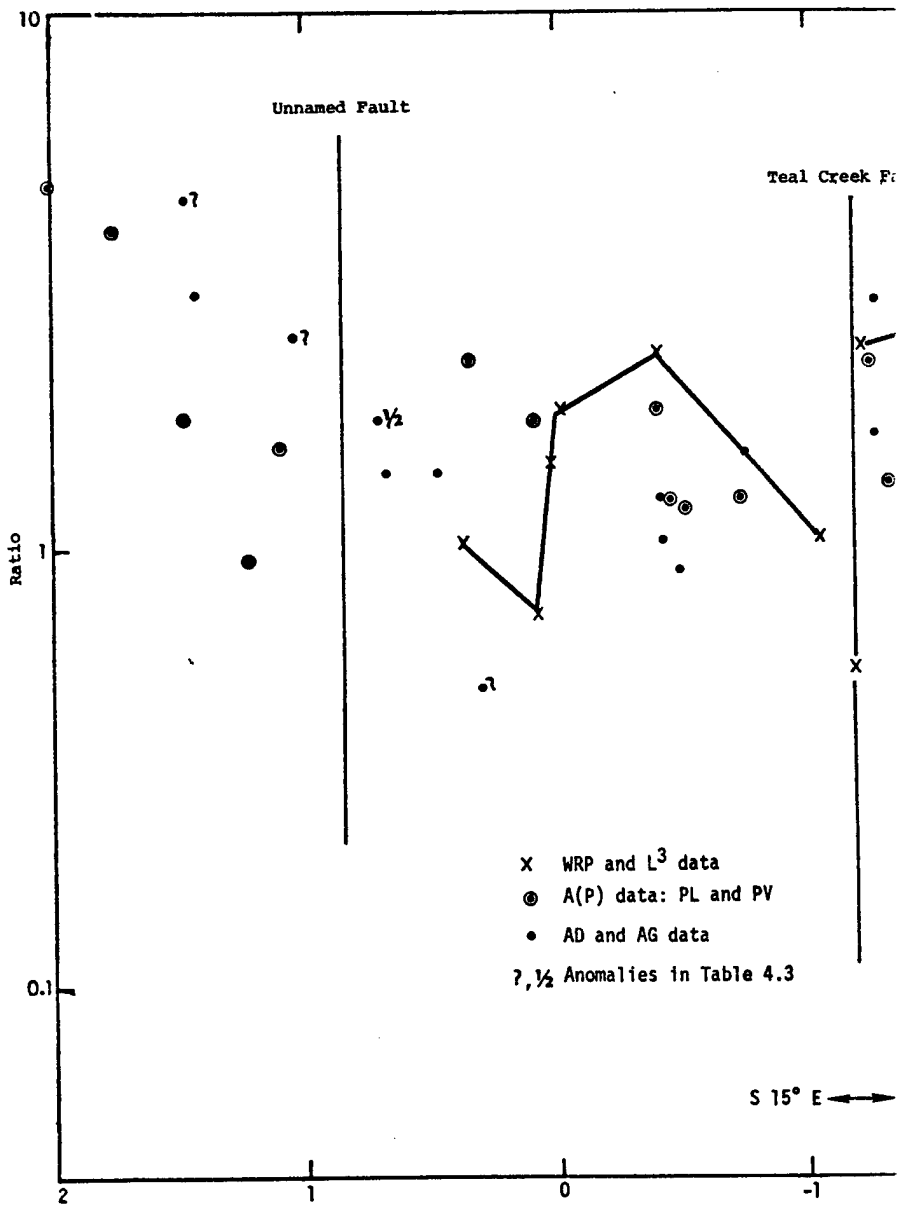

Figure 4.16 Peak measured and inferred accel
faults, normalized to average de

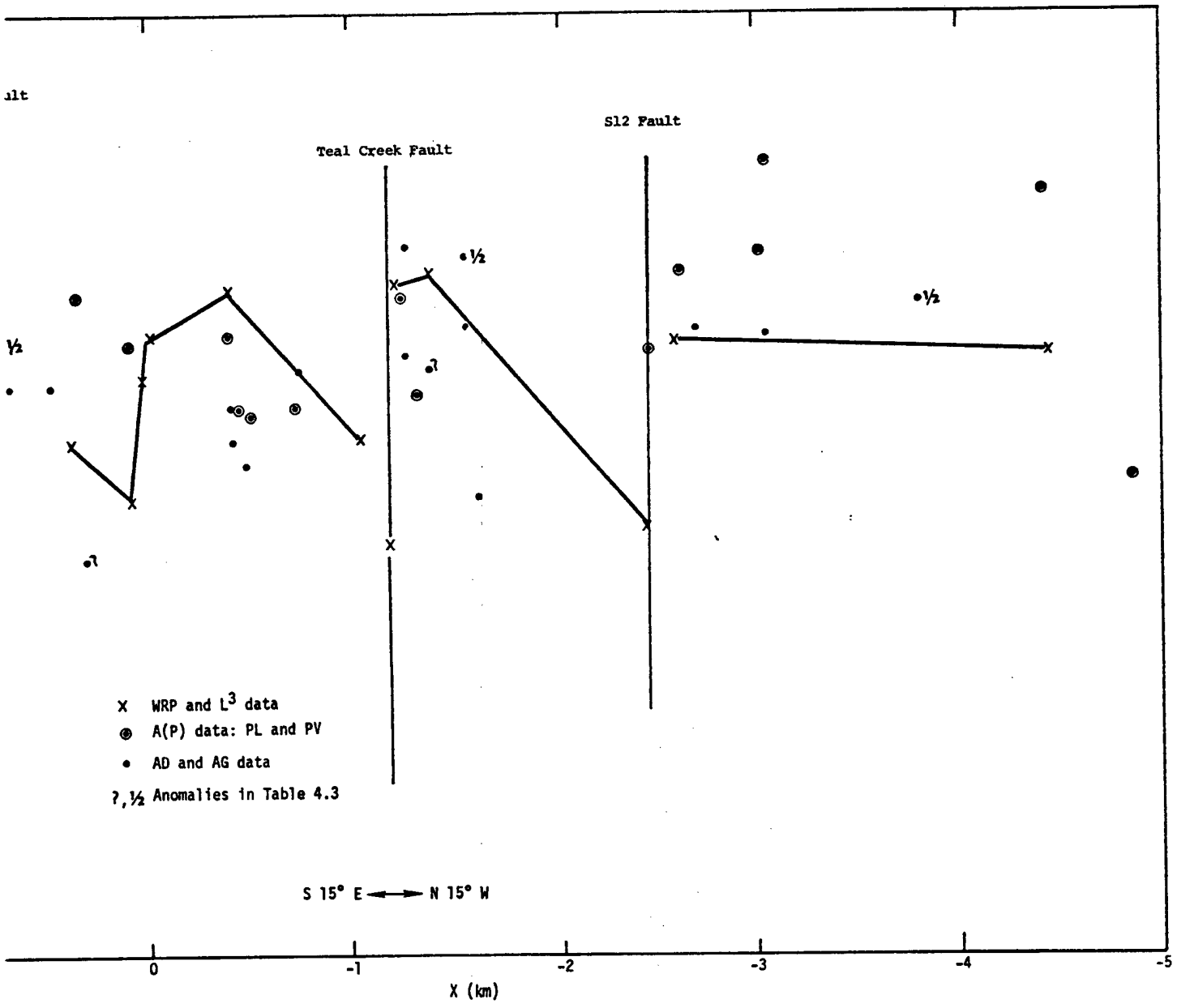

Peak measured and inferred accelerations versus distance normal to cross-island faults, normalized to average decrease of acceleration with slant range

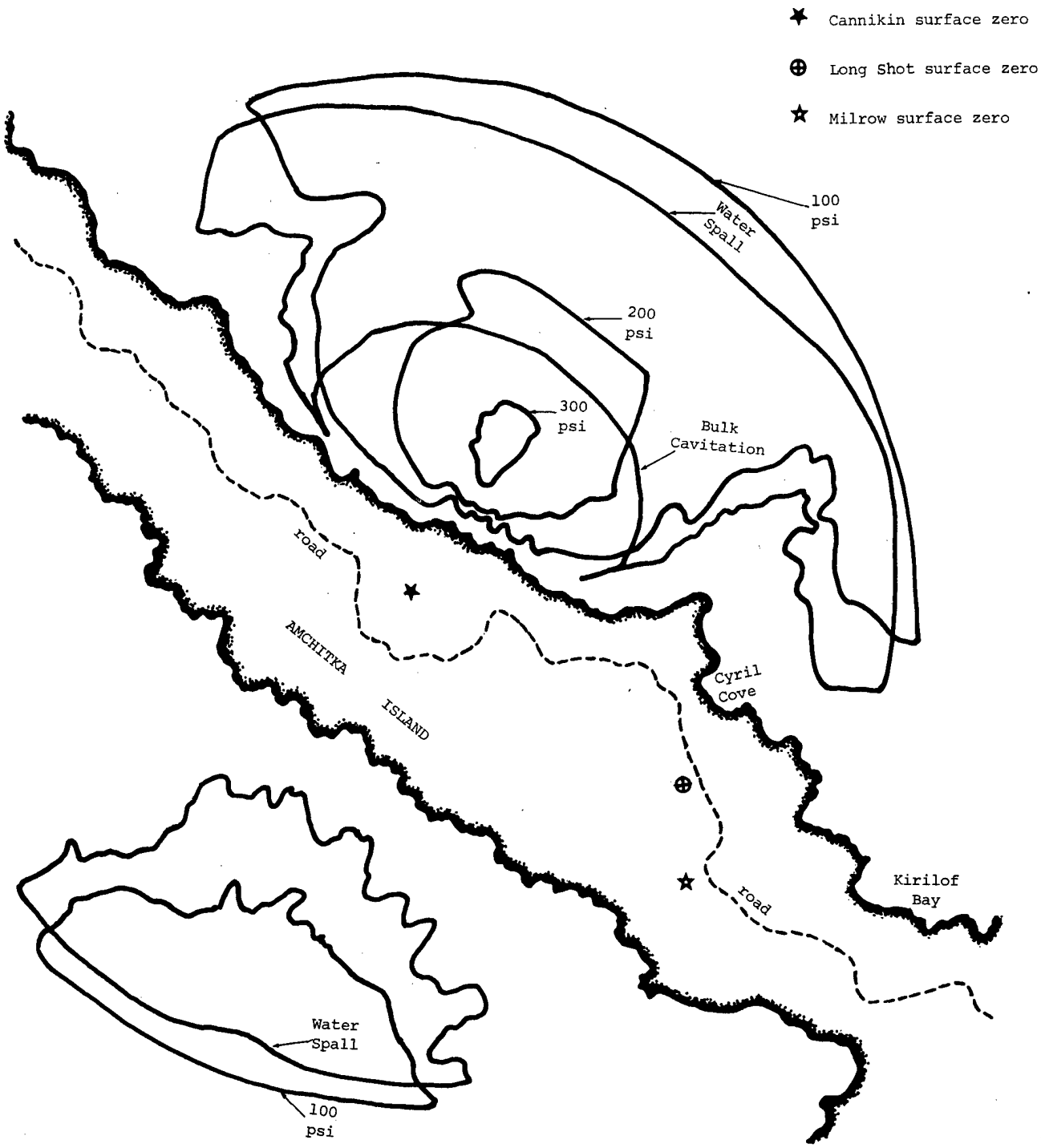

Figure 4.17 Map showing contours of Cannikin bottom pressures, limit of water spall, and limit of bulk cavitation

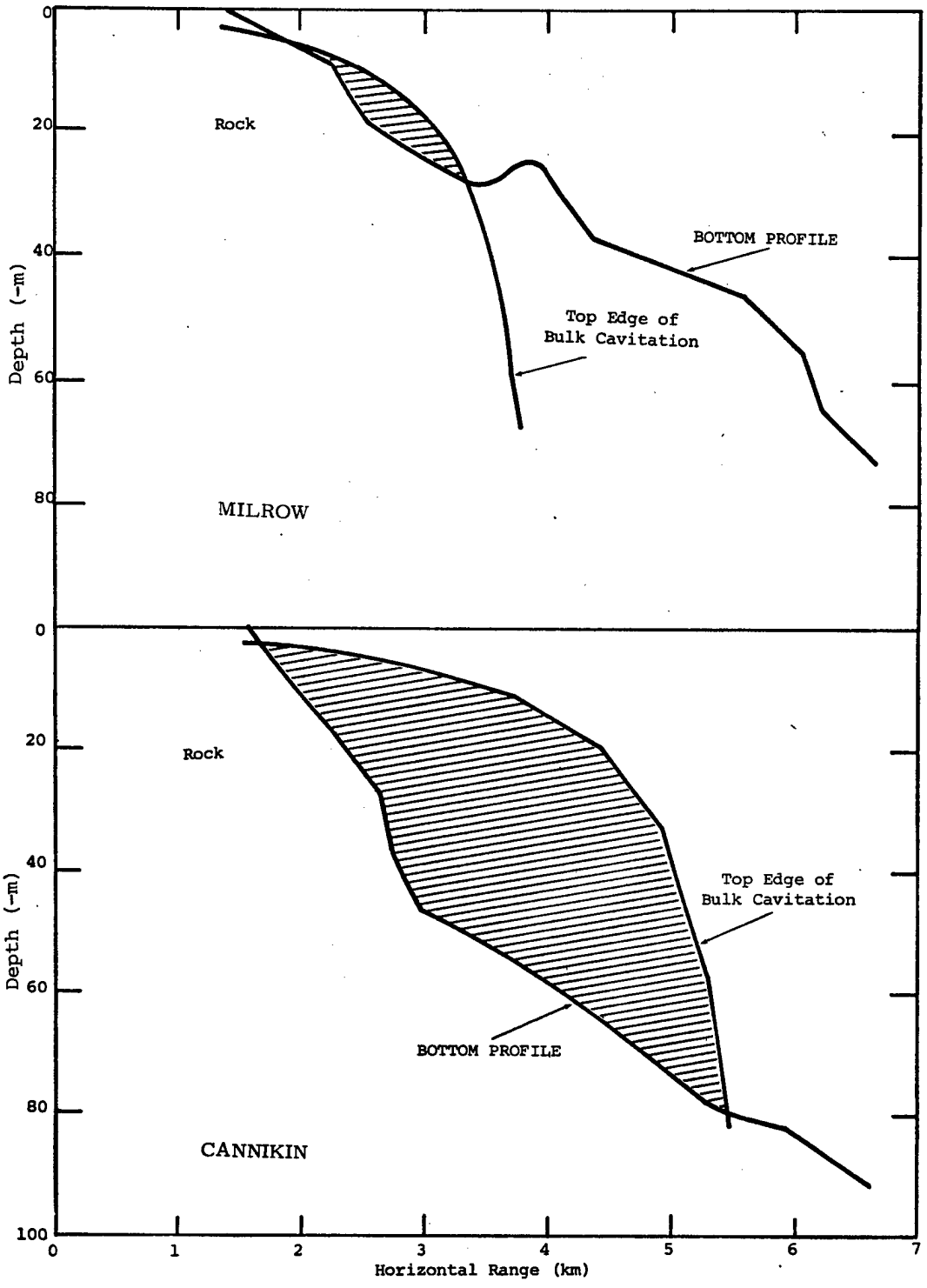

Figure 4.18 Estimates from Equation 4.17 of the volumes within which there was bulk cavitation on Milrow and Cannikin

DISTRIBUTION:

USAEC
Division of Technical Information
P. O. Box 62
Oak Ridge, Tennessee 37830

USAEC (2)
Division of Military Applications
Washington, D. C. 20545

USAEC (2)
Albuquerque Operations Office
P. O. Box 5400
Albuquerque, New Mexico 87115

USAEC (25)
P. O. Box 14100
Las Vegas, Nevada 89114
Attn: Library
E. M. Douthett
R. H. Thalgott
R. R. Loux (20)
P. N. Halstead
E. D. Campbell

USAEC
Division of Operational Safety
Washington, D. C. 20545
Attn: Dr. R. D. Maxwell

LASL (7)
P. O. Box 1663
Los Alamos, New Mexico 87544
Attn: Report Librarian (2)
C. I. Browne
R. R. Brownlee
R. H. Campbell
R. Sharp, Jr.
K. H. Olsen

University of California (8)
Lawrence Livermore Laboratory
P. O. Box 808
Livermore, California 94550
Attn: Library (2)
J. E. Carothers
H. C. Rodean
F. Holzer
P. Coyle
R. Wallstedt
E. Jackson

U. S. Geological Survey (5)
Special Projects Branch
Denver Federal Center
Denver, Colorado 80225
Attn: Library (2)
L. M. Gard
D. D. Gonzalez
W. S. Twenhofel

U. S. Geological Survey
National Center for Earthquake Research
345 Middlefield Road
Menlo Park, California 94025
Attn: J. H. Healy

U. S. Dept. of Commerce
Earthquake Mechanisms Laboratory
390 Main Street, Rm 7021
San Francisco, California 94105
Attn: D. Tocher

U. S. Dept. of Commerce
NOAA/ESL
3060 S. Highland Drive
Las Vegas, Nevada 89102
Attn: K. W. King

Headquarters
Defense Nuclear Agency
Washington, D. C. 20305
Attn: J. G. Lewis

Test Command (2)
Defense Nuclear Agency
Kirtland AFB East
Albuquerque, New Mexico 87115
Attn: Library
B. Grote

Director
Army Engineer Waterways Exp. Station
P. O. Box 631
Vicksburg, Mississippi 39180
Attn: G. Arbuthnot, for J. D. Day

Kirtland AFB West
AF Weapons Laboratory (WLIL)
New Mexico 87117
Attn: Library

USAEC
Division of Peaceful Nuclear Explosions
Washington, D. C. 20545

USAEC
Site Manager
Amchitka, Alaska 99541

Mr. J. J. Davis
Asst. Director for Site & Health Standards
Directorate of Regulatory Standards
USAEC
Washington, D. C. 20545

Physics International Company
2700 Merced Street
San Leandro, California 94557
Attn: F. M. Sauer

Dr. Leo K. Bustad
Director, Radiobiology Laboratory
School of Veterinary Medicine
University of California
Davis, California 95616

Dr. D. U. Deere
2230 Civil Engineering Bldg
University of Illinois
Urbana, Illinois 61801

Dr. Lydik S. Jacobsen
267 Belgreen Place
Santa Rosa, California 95405

Dr. Nathan M. Newmark
1114 Civil Engineering Bldg.
University of Illinois
Urbana, Illinois 61801

Professor Joseph Lintz
Dept. of Geology
MacKay School of Mines
University of Nevada
Reno, Nevada 89507

Professor Paul A. Witherspoon
Dept. of Civil Engineering
University of California
472 Davis Hall
Berkeley, California 94720

Mr. Thomas F. Thompson
713 Crossway Rd.
Burlingame, California 94010

Dr. Vincent Schultz
Dept. of Zoology
Washington State University
Pullman, Washington 99163

Dr. William G. Van Dorn
Scripps Institute of Oceanography
P. O. Box 109
La Jolla, California 92037

Mr. Lewis G. von Lossberg
Sheppard T. Powell & Associates
305 N. Charles Street
Baltimore, Maryland 21201

Dr. James T. Wilson, Director
Institute of Science & Technology
University of Michigan
2200 N. Campus Blvd.
Ann Arbor, Michigan 48105

Mr. Stanley D. Wilson
Shannon & Wilson, Inc.
1105 N. 38th Street
Seattle, Washington 89103

Mr. Carl E. Abegglen
U. S. Fish & Wildlife Service
6917 Old Seward Highway
Anchorage, Alaska 99502

Dr. C. C. Amundsen
Graduate Program in Ecology
University of Tennessee
Knoxville, Tennessee 37916

Mr. Vern Byrd
U. S. Fish and Wildlife Service
P O Box 5015
Amchitka, Alaska 99541

Dr. Carl Kisslinger (1)
Dr. E. R. Engdahl (1)
Cooperative Institute for Research
into the Environmental Sciences
University of Colorado
Boulder, Colorado 80303

Dr. K. R. Everett
Dept. of Agronomy and
Institute for Polar Studies
Ohio State University
Columbus, Ohio 43210

Dr. William T. Helm (1)
Mr. R. A. Valdez (1)
College of Natural Resources
Utah State University
Logan, Utah 84321

Dr. W. M. Major
Dept. of Geophysics
Colorado School of Mines
Golden, Colorado 80401

Mr. James E. McNeil
Sea Operations Dept.
Delco Electronics
6767 Hollister Ave
Goleta, California 93017

Mr. T. R. Merrell
Auke Bay Fisheries Laboratories
National Marine Fisheries Service
P. O. Box 155
Auke Bay, Alaska 99821

Dr. R. E. Nakatani
Fisheries Research Institute
University of Washington
Seattle, Washington 98105

Dr. Robert L. Rausch
Arctic Health Research Center
University of Alaska
Fairbanks, Alaska 99701

Dr. Norman Smith
Arizona Cooperative Wildlife Research Unit
214 Biological Sciences Bldg., East
University of Arizona
Tucson, Arizona 85721

Dr. C. S. White
Lovelace Foundation for
Medical Education & Research
5200 Gibson Blvd SE
Albuquerque, New Mexico 87108

Dr. F. S. L. Williamson
Chesapeake Bay Center for Environmental Studies
Smithsonian Institution
Route 4, Box 622
Edgewater, Maryland 21037

Mr. Karl Schneider
Alaska Dept. of Fish & Game
1018 West International Airport Road
Anchorage, Alaska 99502

Battelle Memorial Institute
Columbus Laboratories
505 King Avenue
Columbus, Ohio 43201
Attn: R. S. Davidson

Mr. Roger J. Desautels
Archaeological Research, Inc.
1641 Monrovia Avenue
Costa Mesa, California 92627

Mr. R. G. Fuller
P O Box 622
Oracle, Arizona 85623

Dr. John P. Cook
University of Alaska
Fairbanks, Alaska 99701

EG&G
P. O. Box 204
San Ramon, California 94583
Attn: R. G. Preston

C. R. Mehl, 5230
B. F. Murphey, 8300
L. R. Hill, 8314
G. A. Fowler, 9000
C. D. Broyles, 9100
J. D. Kennedy, 9110
W. D. Weart, 9111
W. R. Perret, 9111
L. J. Vortman, 9111
G. E. Hansche, 9120
B. C. Benjamin, 9123
H. E. Viney, 9130
J. R. Banister, 9150
M. L. Merritt, 9150 (10)
L. S. Ostrander, 8232
R. S. Gillespie, 3151 (3)
For AEC/TIC (public Release)
L. C. Baldwin, 3152
Division 3141 (4)